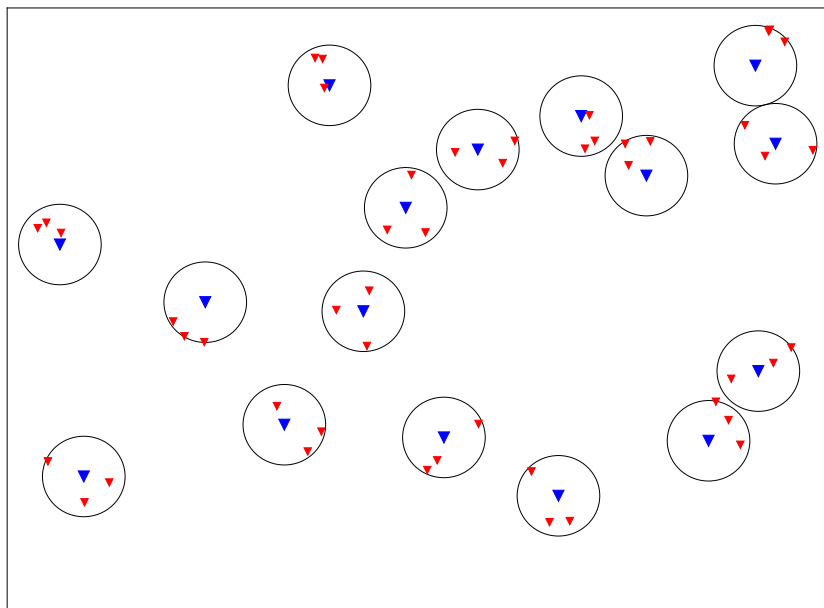

Mathematical Modelling and Prediction of Interference Power in In-robot Subnetworks

Master's Thesis



Aalborg University
Mathematical Engineering

Copyright © Aalborg University 2022

This project has been written in \LaTeX with figures produced in \TikZ and Python. Scripts have been made using Python.



Mathematical Engineering
Aalborg University
<http://www.aau.dk>

AALBORG UNIVERSITY

STUDENT REPORT

Title:

Mathematical Modelling and Prediction of Interference Power in In-robot Subnetworks

Theme:

Master's Thesis

Project Period:

Fall Semester 2021 and
Spring semester 2022

Project Group:

math-22-mattek-10-11

Participants:

Lars Vedel Friis
Lukas Menholt

Supervisors:

Ramoni Ojekunle Adeogun
Christophe Biscio

Number of Pages: 90

Date of Completion:

June 2, 2022

Abstract:

The envisioned wireless networks, 6G in-X subnetworks have extreme requirements for latency, data rate and reliability. The in-X subnetworks considered in this thesis, is the in-robot subnetworks in a factory setting. The interference power which comes from the in-robot subnetworks in a factory setting is analyzed and predicted throughout this thesis.

Analytical expressions for the mean and auto-correlation function (ACF) of the interference power are derived. The expressions for the mean and ACF contained high dimensional integrals which we estimate using Monte Carlo (MC) integration. When estimating the expression for the mean it was found that the analytical mean fitted the mean of the interference power obtained from simulations. It was found that when estimating the expression for the ACF using MC integration that it would overestimate the ACF of simulated interference power. However, the ACFs had the same form, thus, an appropriate scaling could make them coincide.

Furthermore, the interference power simulated from in-robot subnetworks was predicted using an autoregressive (AR) model of order 20. We also found that the interference power could be predicted using the AR(20) predictor for up to 8 [ms] when the velocity is 2 [m/s]. Additionally, the AR(20) predictor outperformed the last value predictor for all settings.

Preface

This Master's thesis was written by Lars Vedel Friis and Lukas Menholt of the Master program Mathematical engineering in the time period 1st of September 2021 to the 3rd of June 2022. The thesis was written in cooperation with the Department of Mathematical science and the Department of Electronic Systems.

The reference style follows the IEEE-method with specified page numbers of the source. A detailed description of the references can be found in the bibliography.

The figures in this thesis are produced by the group in Python 3.8 or the *TikZ* package in \LaTeX . The scripts are produced and simulation are performed using Python 3.8.8.

The authors would like to thank Ramoni Ojekunle Adeogun and Christophe Biscio for their supervision throughout the development of this thesis. Furthermore, the authors would like to thank Jorge F. Schmidt, Udo Schilcher, Mahin K. Atiq and Christian Bettstetter for sharing the code for their interference predictor, described in [1], with us.

Aalborg University, June 2, 2022

Lars Vedel Friis
<lfriis17@student.aau.dk>

Lukas Menholt
<lmenho17@student.aau.dk>

Danish Summary

Vi er i en tid, hvor der kommer mere og mere trådløs kommunikation, dette sker da vi er midt i en overgang fra internet af ting til internet af alting. For at fuldende denne overgang bliver der nødt til at være trådløse forbindelser som opfylder ekstreme krav for data-rate, pålidelighed og forsinkelse. Et trådløst netværk der er udset til at opfylde disse ekstreme krav er i-X undernetværker. I dette projekt fokuserer vi på i-robotter undernetværker i en industriel sammenhæng. Vi fokuserer specifikt på den interferens der sker mellem undernetværkerne, eftersom at denne interferens kan være med til at de ekstreme krav om pålidelighed ikke bliver opfyldt.

I denne afhandling analyseres interferensen fra i-robotter undernetværker i en industriel sammenhæng, derudover vil interferensen blive prædikeret. Vi starter med at lave en interferens model hvor alle de forskellige dele af interferensen bliver beskrevet. Specifikt, hvilken model for trafik, small scale fading, shadowing og path-loss der vil blive brugt igennem rapporten. Ydermere er det beskrevet, hvordan undernetværkerne bevæger sig. Efterfølgende bliver der lavet en matematisk beskrivelse af interferensen givet ud fra den beskrevet interferens model. Ud fra den matematiske beskrivelse er analytiske udtryk for middelværdien og autokorrelationsfunktionen (ACF'en) udledt. Disse udtryk indholder integraler, som vi ikke kan løse analytisk, så de bliver løst ved hjælp af Monte Carlo (MC) integration. Det bliver vist, at når det analytiske udtryk for middelværdien bliver regnet ved hjælp MC integration, så stemmer det overens med den empiriske middelværdi af interferensen, når den bliver simuleret ud fra interferens modellen. I tilfældet hvor ACF'en bliver løst ved hjælp af MC integration, ses det, at ACF'en for det simuleret interferens bliver overestimeret. Dog ses det også, at de har samme form. Det vises også, at ved hjælp af en tilpas skalering, så ligger ACF'en, udregnet ved hjælp af MC integration, oveni ACF'en af interferensen simuleret fra interferens modellen.

Basis teorien bag autoregressive modeller præsenteres, og anvendes til at konstruere en interferens prædikator. Et forudgående forsøg bliver lavet, hvori forsøgsindstillinger bliver valgt sammen med ordenen af prædiktoren. Den autoregressive interferens prædikator bliver testet under forskellige scenarier, hvori størrelsen af rummet, un-

dernetværkernes hastighed og antallet af undernetværker ændres. Prædiktoren kan forudsige interferensen for tidsforskydninger op imod 8 [ms], når der er lav signal til støj ratio og hastigheden af undernetværkerne er 2 [m/s]. Desuden præsterer den autoregressive prædikator bedre end en sidste værdi prædikator for alle testscenarierne.

Abbreviation List

ACF	Autocorrelation function.
ADAS	Advanced driver-assistance systems.
AR	Autoregressive.
ARMA	Autoregressive moving average.
CSMA	Carrier sensing multiple access.
DDCA	Distributed dynamic channel allocation.
DNN	Deep neural network.
i.i.d.	Independent identically distributed.
MC	Monte Carlo.
BPP	Binomial point process.
MPP	Matern point process.
PPP	Poisson point process.
TDD	Time Division Duplexing.
TU	Time unit.
DL	Downlink.
UL	Uplink.
WSS	Wide-sense stationary.

Notation List

\mathbb{N}^+	Set of positive integers $\{1, 2, \dots\}$.
\mathbb{N}	Set of the natural numbers $\{0, 1, 2, \dots\}$.
$\mathbb{P}(\cdot)$	Probability measure.
$\mathbb{P}(\cdot \cdot)$	Conditional probability measure.
\mathbb{E}	Expected value operator.
\mathbb{E}_{\cdot}	Expected value operator with respect to \cdot .
$z \sim f(z)$	z follows a distribution with probability density function $f(z)$.
\mathbf{v}	Vector.
$h_{\cdot}(\cdot)$	Small scale fading.
$\ell(\cdot)$	Path-loss function.
$\gamma_{\cdot}(\cdot)$	Traffic function.
$\zeta(\cdot, \cdot)$	Shadowing.
N	Number of sensor actuator pairs in a subnetwork.
M	Number of subnetworks.
K	Number of channel groups.
N_{sg}	Number of subnetworks per channel group.

N_{TU}	Number of time units in either uplink or downlink.
T_{UL}	Duration of uplink.
T_{DL}	Duration of downlink.
T_f	Duration of a frame.
L_0	Number of waves in small scale fading.
f_c	Carrier frequency.
J_0	Zeroth-order Bessel function of first kind.
α	Path-loss exponent.
d	Minimum distance between the centers of the subnetworks.
r	The cell radius of the subnetworks.
ν	Velocity of the subnetwork.
$[M]$	integers up to M , $[M] = 1, 2, \dots, M$.
$\Phi = \{\mathbf{x}_{[M]}\}$	A collection of the locations of the control units of the subnetworks.
$\Phi_k = \{\mathbf{x}_{k[M]}\}$	A collection of the locations of the sensor actuator pairs of the k -th subnetwork.
$\Xi_k = \{\boldsymbol{\xi}_{k[M]}\}$	A collection of the locations of sensor actuator pairs of the k -th subnetwork relative to the control unit.
$ \cdot $	The Lebesgue measure.
\mathcal{U}	Uniform distribution.
\mathcal{N}	Normal distribution.
j	Imaginary unit, $\sqrt{-1}$.
\hat{x}	Estimate of x .

Contents

Preface	vii
List of Abbreviations	xi
List of Notation	xiii
1 Introduction	1
2 Problem Analysis	3
2.1 Brief History on Wireless Networks	3
2.1.1 Analysing Wireless Networks Using Stochastic Geometry	4
2.2 Modelling Interference in Wireless Networks	5
2.3 In-X Subnetworks Model	7
2.3.1 Factory in-X Subnetworks	7
2.3.2 In-vehicle Subnetworks	8
2.3.3 In-body Subnetworks	8
2.3.4 In-house Subnetworks	9
2.3.5 Interference Challenges and Its Mitigation in 6G in-X Subnetworks	9
2.4 Existing Interference Predictors	10
2.5 Problem Statement	12
3 Description of Interference Model	13
3.1 Model Description	13
3.2 Test of Predictability in Order to Implement and Analyse the Interference in in-X Subnetworks	24
3.2.1 Changes to the Model	30
3.3 Stochastic Interference Model	31
3.4 Derivation of the Mean and ACF of the Interference	33
3.4.1 Derivation of the Mean Interference	33
3.4.2 Derivation of Temporal Covariance of the Interference	35
3.4.3 Autocorrelation Function of the Interference	42

4	Proposed Predictors	43
4.1	Last Value Predictor	43
4.2	Autoregressive Processes and Predictors	43
4.2.1	Autoregressive Processes and Yule Walker Equations	44
5	Numerical Evaluation	47
5.1	Evaluating the Mean and ACF From the Stochastic Interference Model	47
5.1.1	Using MC Integration To Estimate the Mean Interference Power	47
5.1.2	Comparing the Mean Estimated Using MC Integration to the Mean of Simulated Interference Power	50
5.1.3	Using MC Integration to Estimate the ACF of the Interference Power	52
5.1.4	Comparing the ACF Estimated Using MC Integration to the ACF of Simulated Interference Power	57
5.2	Performance Evaluation of the Predictors	60
5.2.1	Preliminary Experiment	60
5.2.2	Performance Evaluation of the Predictors	63
5.2.3	Comparing AR(20) Predictor with Last Value Predictor	66
6	Discussion	69
7	Conclusion	73
8	Future Research	75
A	Point Process Theory	77
A.1	Binomial Point Process	79
B	Monte Carlo Integration	81
C	Additional Results	83
	Bibliography	87

1. Introduction

In today's day and age there is an ever increasing number of wireless solutions [2, p. 23]. This is all around us, from wireless keyboards, to the washing machine sending a message when it is done, to a type one diabetic with wireless glucose monitor attached to their body, to much more. This increase in wireless solutions we are experiencing is the transition from internet of things to internet of everything, where objects, processes and people are connected instead of objects only [3]. The requirements to fully transition to internet of everything cannot be reached with the 5th generation network but rather with the 6th generation network. This is due to 5G will be unable to completely support the extreme requirements envisioned in internet of everything [3]–[5], that is, higher reliability, lower latencies and higher data rates. A type of wireless networks which is envisioned to comply with extreme requirements is in-X subnetworks [4], here "X" stands for an entity, for example, vehicles, robots or the human body. The term subnetwork is because the network cells can be connected to the 6G network but should also be able to operate when being outside of coverage of the wide area network, as the subnetworks are expected to support life-critical functions.

Interference can decrease reliability of a link in a wireless network. Interference occurs when two or more transmitters transmit on the same channel at the same time to each of their receiver but since they transmit on the same channel the receivers receive a sum of the transmitted signals. Interference is thus the unintended messages that are received which makes it harder to decode the intended message [2, pp. 21-22]. The use-cases for the in-X subnetworks can result in dense scenarios, such as, a large number of cars at an intersection or in-body during crowded events, which necessitates the need for proactive interference management [5], [6]. A great deal of research in 6G network has already begun, and many countries have already initiated a 6G project [3]. In [7], they investigate the potential gain of using distributed dynamic channel allocation (DDCA) for mobile 6G in-X subnetworks in an industrial setting, they further propose three different algorithms to perform the DDCA. In [8], a design of a short range wireless isochronous real time in-X subnetworks is proposed with the focus on life-critical applications with low latency and high reliability. This type of network is envisioned to be deployed in robots or vehicles. Interference prediction can be used to improve the reliability and the latency in a network, as it is a proactive method which can be used before interference occurs, and thus reduce the overhead

of spectrum sensing and the outage probability [9]. With the ambitious 6G network, it may be possible to reach industry 4.0 and robotics, where wired solutions become wireless while a high reliability and low latency is preserved [10]. Thus, in order to aid in satisfying these extreme requirements, the focus of this report is analyzing and predicting the interference within in-robot subnetworks in a factory setting.

This master thesis is structured as follows: In Chapter 2, the problem is analyzed and the current progress within interference prediction as well as research within in-X subnetworks are presented, the chapter is concluded with our problem statement. In Chapter 3, we present our interference model for the in-robot subnetworks in a factory setting, and we derive the mean interference and autocorrelation function (ACF) under the interference model. In Chapter 4, we present the proposed interference predictors which are used in a numerical evaluation. In Chapter 5 we compare the derived mean interference and ACF to the empirical ones as well as test the proposed interference predictors. The results are discussed in Chapter 6, and conclusions of the thesis are drawn in Chapter 7. Lastly, future research possibilities are described in Chapter 8.

2. Problem Analysis

In this chapter, we will present the problem statement which involves predicting interference in a future type of network, known as in-X subnetworks. However, before doing that, it is necessary to present the current progress within the field of interference in wireless networks. Therefore initially, we will shortly present different aspects of wireless networks, and how stochastic geometry is a useful tool. Afterwards, various results will be presented from articles where interference has been characterized using different model assumptions. Envisions about the in-X subnetworks are then presented as well as specific use cases, requirements and challenges. Various existing interference predictors are then presented, where after we will conclude the chapter by presenting the problem statement.

2.1 Brief History on Wireless Networks

In the modern society, there has been an increasing demand for the connectivity of mobile devices. Staying connected anywhere at anytime helps people live more fulfilled lives [11, p. 4]. The cellular network has evolved greatly over the past three decades and is the main source of such ubiquitous connectivity [11, p. 3].

The increasing demand for connectivity yields challenges for the network operators. There are mainly three points that should be considered, that is, affordability, availability and quality. Affordability covers the expenses of deploying and maintaining a network as well as the price of acquiring a spectrum license. Availability has largely been solved by the introduction of 2G cellular networks which is available almost everywhere. The quality of a network is indicated by the average total throughput per unit area. The average total throughput per unit area is the capacity of a network [11, pp. 4-5]. The capacity is the product between the average number of active connections per unit area and the average rate on such data connections. The average rate can be found as the product of the bandwidth and the spectral efficiency of the data connections. The spectral efficiency and the SINR of a link are closely related. This relation can be seen in Shannon's capacity formula which is given by

$$C = B \log_2 \left(1 + \frac{S}{N + I} \right) \quad (2.1)$$

where C is the capacity, B is the bandwidth, S is the average signal power, N is the average noise power and I is the average interference power, that is, the average interference power is obtained by averaging over instantaneous interference power for a given time [12, pp. 272-273].

From Eq. (2.1), the quality of a network can be improved by increasing the bandwidth. However, the bandwidth of a network is not easy to increase, as new spectrum is rarely freed up and it is expensive when it happens. The quality can also be increased by improving the spectral efficiency. A way to improve the spectral efficiency is by dividing existing bands into smaller bands provided that the smaller bands are appropriate to support an acceptable data rate. However, these divisions of the frequency spectrum can only happen a finite amount of times before the bands cannot support an acceptable data rate. [11, p. 5]

An alternative way to increase the quality, and thereby the capacity, is by spectrum reuse, here the spectrum is shared among multiple users where they try to mitigate their mutual interference. In the time period 1955-2020 spectrum reuse has been the greatest contributor to the increase of network capacity. [11, p. 5] [13], [14]

2.1.1 Analysing Wireless Networks Using Stochastic Geometry

When analysing the performance of a proposed network through simulations, many simulations may not necessarily provide a useful insight as the performance of the network is too low for those scenarios. Since 2010 some analytical and semi-analytical results regarding the SINR distribution has been found for various networks. Say that we could relate the SINR distribution at a user to the parameters of the deployment of a network, such as, transmission power and densities of the cells. Then some of the scenarios which do not yield a sufficient network performance could be eliminated. The tools used to derive the analytical results are mainly from the mathematical field stochastic geometry, and specifically to model the base stations location as a realizations of point processes has proven useful. [11, p. 9]

There has been derived several useful results regarding the SINR when the base stations are distributed according to a homogeneous Poisson point process (PPP), as it is the best understood model and it is analytical tractable. However, there also exist some tractable models where the points are either more clustered or the distance between the points are greater than that of a Poisson process. Both cases are useful when modeling a cellular network. For example, in coverage-oriented deployment there is a minimum distance between neighbouring base stations. Hence it would be reasonable to model the locations using a point process where the points repel each other. On the other hand, in a capacity-oriented deployment the base stations are grouped together around hot spots, an appropriate point process to model the locations is then one in which the points appear in clusters. [11, pp. 10-12]

2.2 Modelling Interference in Wireless Networks

The interference can be characterized in different ways, depending on what type of network is considered. Various models exist some of them are more general and tractable while others are more specific and complex. Which kind of model should be used depends on the application [15]. For example, a lot of work has been done in order to obtain analytical results using stochastic geometry, but this is often done using more general models.

Before presenting the different models, we want to present the basic components that need to be modelled, so consider the interference received at a point $\mathbf{y} \in \mathbb{R}^2$ at time $t \in \mathbb{R}$.

$$I_{\mathbf{y}}(t) = \sum_{\mathbf{x} \in \Phi} \ell(\mathbf{y} - \mathbf{x}) H_{\mathbf{y}}(\mathbf{x}, t) \gamma_{\mathbf{x}}(t) \quad (2.2)$$

where ℓ is a path-loss function, $H_{\mathbf{y}}$ is a random nonnegative field, $\gamma_{\mathbf{x}}$ is the traffic parameter of the node at \mathbf{x} and Φ is a collection of node locations. Note that the node locations Φ may be time dependant, $\Phi(t)$, but for ease of notation we write Φ . The path-loss ℓ is a nonnegative function. The random nonnegative field $H_{\mathbf{y}}$ is a random propagation field containing effects like small-scale fading, shadowing and/or transmission power [11, p. 43]. When modelling interference the transmission power is usually set to 1. The traffic parameter $\gamma_{\mathbf{x}}$ is usually an indicator function which is 1 if the node \mathbf{x} is transmitting and 0 if idle. The node locations Φ at time 0 is usually described using a point process and then move according to some mobility model if they are mobile.

The PPP is by far the most common model for node locations, as the PPP is the most tractable and well understood model. Networks using a PPP to model the locations of the nodes are referred to as Poisson networks. Furthermore, the interference in a Poisson network accurately estimates the interference in a cellular network where the nodes/base stations repel each other, if the intensity is chosen carefully, according to [16]. Some work of modelling the interference in Poisson networks has been done in [16]–[20] for wireless networks.

In wireless networks the antennas are usually assumed to be omni-directional, and each node is equipped with a single antenna. In [16], the interference in a cellular network is modelled. The interference is modelled using a Poisson network with distance dependant path-loss and an iid unit variance circularly symmetric complex Gaussian variable as a fading model. They put a lot of emphasis on the PPP approximation theorem, where the interference with nodes placed according to a repulsive point process can be estimated by a PPP with an exclusion region around the receiver, and use it to characterize the SINR and related performance metrics.

In contrast to [16], the authors in [21] state that a PPP should not be used to

approximate a point process where the points repel each other, as it is only accurate for first order statistics and not higher order statistics. Specifically, they use a Matérn point process (MPP) in [21], to approximate the usage of carrier sensing multiple access (CSMA) as a minimum distance should be imposed between active nodes. The reason is that if CSMA is used, it is highly unlikely that two nodes close to each other can be active at the same time. In [21], they derive a close form expression for the temporal correlation of the interference, using an interference model with iid Nakagami fading and non-singular distance dependant path-loss. Further, they compare the Matérn network to a Poisson network and show that the average interference may be similar, however, the correlation function behaves significantly different. Hence, one should be careful with approximating an MPP using a PPP.

In [22], the throughput and outage probability is analysed for home users during the corona virus disease 2019 (COVID-19). Due to the pandemic, many industries and institutions had to make their employees work from home, this resulted in an increase in the amount of people who use video streaming applications. Due to the inhomogeneities in a city's building formation the Wi-Fi access points should not be modelled as being uniformly located. A Neyman Scott process was used in order to model Wi-Fi access points in clusters. Specifically, they used a homogeneous PPP as the mother process and a uniform distribution for the daughters, where the number of daughter points in each cluster is Poisson distributed.

In [19], the interference in a Poisson network is characterized in terms of a burstiness and a memory measure from the theory of temporal networks. The analysis is performed on a channel which is modelled using non-singular distance dependant path-loss and Nakagami block fading. The nodes transmit according to a probability all with the same message duration. Two mobility models are considered namely Brownian motion and random direction. The paper attempts to determine which factors of a Poisson network causes the bursty behavior observed in interference. It concludes that it is a combination of the rapidly and slowly changing factors contributing to the interference as well as the characteristics of Brownian motion that causes an increase in burstiness and memory. The rapidly and slowly changing factors are associated with the channel and the traffic, specifically the fading block length, the message length and the node velocity.

In [17], significant work has been put into deriving the temporal correlation of the interference in Poisson networks, this is done using the Pearson correlation coefficient. The correlation function is derived under various model assumptions. The node locations are modelled as a homogeneous PPP. The nodes are active with respect to a probability and the messages have constant length for all transmissions, resulting

in slotted ALOHA. The node mobility follows either Brownian motion or linear direction mobility. Lastly, the channel is modelled using a non-singular path-loss in combination with Nakagami block fading or Rayleigh fading generated using Clarke's model. They found that the temporal correlation of the interference changes if the velocity of the node movement, the message duration, the transmission probability or the block length changes. That is, the node location, traffic and wireless channel all contribute to the temporal correlation of the interference.

2.3 In-X Subnetworks Model

In-X subnetworks models are used to model networks consisting of subnetworks which each consists of a control unit and multiple sensors and actuators. The in-X subnetworks operate in the higher frequency bands around 6 – 10 [GHz] [7]. The sensors transmit information to the control unit, which will then process the information and transmit actions to the actuators. In-X subnetworks are expected to satisfy extreme requirements such as ultra reliable low latency communication with latencies below 0.1 [ms] and a packet error rate in the order of 10^{-6} to 10^{-9} [8]. The name in-X subnetworks refers to a subnetworks placed inside X which could be a car, house, factory or even the human body. In [4] they describe envisions for the different, just mentioned, use cases. The choice of where the subnetwork is placed obviously impacts how and if the subnetwork are able to move as well as the requirements for the subnetworks. We will briefly go through the four use cases mentioned in [4] and the envisioned requirements for each. Afterwards, the challenge of interference in 6G in-X subnetworks and how it is currently being mitigated will be discussed. The requirements are intended to be the most extreme cases, and they may be relaxed in cases where such demanding requirements are unnecessary.

2.3.1 Factory in-X Subnetworks

Factory in-X subnetworks are subnetworks that are placed in a factory setting, for example, in robots in a factory hall. The in-X subnetworks are expected to replace some of the wired solutions where it is critical to have latencies below 0.1 [ms] [4]. The subnetworks could control a robots movements and its precision when it comes to manufacturing products in a production line. Furthermore, subnetworks in mobile robots could control the mobility and thereby avoid other mobile robots and obstacles. The transmission traffic in the subnetworks may be a periodic traffic pattern for most use cases, however, some event-based traffic could also be used, in case of sporadic events. The subnetworks may also be able to collect statistics or other key performance indicators, which can be send to a local server. The robots could then be analyzed in order to identify anomalies in their behaviors and stop the robots before any production errors occurs. The expected number of devices, that is, sensors and actuators, in a robot is in the order of 10 – 20 for motion and force control, while for mobile robots it is 20 – 40. The maximum subnetwork density is expected to

be around $40000/\text{km}^2$. The robots should be ultra reliable and the communication service should satisfy the quality of service requirements $99.9999 - 99.999999$ % of the time.

2.3.2 In-vehicle Subnetworks

In-vehicle subnetworks are envisioned to replace the controller area network bus. Hence, the subnetworks will handle stuff like the anti-lock breaking system and the engine control. For highly critical transmissions such as high priority trigger messages the maximum latency is 0.054 [ms] [23]. This critical traffic may be accompanied with high data rates from advanced driver-assistance systems (ADAS) which utilizes data from camera sensors for adaptive cruise control and traffic sign recognition. The data rates are envisioned to be less than 10 Gbps for the ADAS and 10 Mbps for the control. The traffic can be both periodic and event-based like in the factory setting. The reliability is critical and the probability that the service is delivered according to the quality of service should be in the order $99.9999 - 99.999999$ %. The density of the subnetworks varies depending on where the car is, however, a maximum density is expected to be around $150/\text{lane-km}$. Besides cars the subnetworks could also be placed in various segments inside an airplane.

2.3.3 In-body Subnetworks

The devices used in in-body subnetworks can be divided into two categories, devices on the body and devices inside the body. The devices on the body could be skin patches and sensors for temperature and blood pressure while devices inside the body could be implants in the form of a pacemaker, insulin pump or muscle controllers. The control unit could be placed in a wristband or possibly in the form of a brain implant. The implants could be able to help people suffering from diseases, like patients suffering from diabetes could have a wireless insulin pump implanted to maintain the right glucose level [24]. Likewise, muscle controllers could be used to enable movements in people with motor disabilities [25]. The control unit could potentially be connected to an external network, and in case of anomalies, for instance unusual heart beat pattern, then the person could be sent to the hospital. A critical requirement for the in-body subnetworks is the battery placed in the wireless devices as they are expected to last for years. The in-body subnetworks do not require high data rates or low latencies, however, the required service level must be fulfilled as the applications can be life-critical. The probability of satisfying the quality of service should be 99.999999 % with the traffic being periodic and event-based. The density of subnetworks may vary greatly depending on where the person is, and the requirements should be satisfied despite the person being in crowded areas with chances of higher interference, for instance at a concert. The maximum subnetwork density is envisioned to be around $2/\text{m}^2$.

2.3.4 In-house Subnetworks

The in-house subnetworks are expected to cover the data flow across devices in different rooms or in the same room. The applications are usually not latency critical, here it is assessed that a maximum latency of 5 [ms] is sufficient for entertainment applications, such as gaming with extended virtual reality. Extended virtual reality may include a full body haptic suit where devices are distributed on the persons body. Extended VR requires high data rates, and it is envisioned that a data rate of 7 Gbps is needed. The traffic between the devices is event-based. It is expected that the maximum density is 1/room.

2.3.5 Interference Challenges and Its Mitigation in 6G in-X Subnetworks

Due to the some of the life-critical application envisioned for the 6G in-X subnetworks, the subnetworks should be resilient to dense scenarios which may occur [4]. The dense scenarios could for example be humans attending a concert, cars on a congested road or at an intersection or even an in-body subnetwork inside an in-car subnetwork [5]. In order for the 6G in-X subnetworks to maintain the extreme requirements, the problem of interference that occur in these dense scenarios needs to be addressed. This problem has led to research within radio resource allocation methods for dense 6G in-X subnetworks [5], [7], [26].

To aid the reliability, a combination of blind repetition and channel hopping can be used, that is the same message is transmitted on different channels regardless of the previous transmission attempts were successfully received. This is proposed for applications where the transmissions mainly consist of control loops [4]. In [8], an initial design is proposed for short range wireless isochronous real time in-X subnetworks for life-critical applications where the latency of control loops should be shorter than 0.1 [ms]. Specifically, potential frequency bands are presented along with a frame structure for the transmissions, and further the required bandwidth in order to achieve ultra reliable low latency communication is investigated. However, this transmission scheme, with blind repetition and channel hopping, may not be sufficient to ensure the high reliability that some applications require [4]. Thus some additional methods to reduce the interference may be needed. Most of the existing methods for 5G are reactive, hence interference is experienced before action is taken. Reactive methods is not recommended for the 6G in-X subnetworks with low latency requirements. Instead it is envisioned that the methods used for the in-X subnetworks should be proactive [4], [5].

Depending on the application the interference can be managed in different ways. One approach is centralized management, where the subnetworks report to a central controller such that information about transmissions from the different subnetworks is shared among each other [4]. Another approach is distributed interference management where the subnetworks do not share information, but instead rely on information on the portion of the frequency band where they are active, that is local

sensing. From the local sensing, the subnetworks should make decisions on the allocation of its resources. This decision can be made using machine learning such as a deep neural network (DNN) or reinforcement learning [6], [26]. In [26], a DNN is trained for each of the subnetworks, the DNN uses the local sensed interference power as input and performs a mapping to a class of shared frequency channels. In [6], reinforcement learning is used to solve a multi-objective optimization problem where the sum capacity is maximized at each subnetwork subject to the power and transmission bandwidth constraints. It could also be of interest to use prior knowledge about the 6G in-X subnetworks in the proactive algorithms, for instance Bayesian reinforcement learning could be used to perform resource allocation where prior knowledge about the interference and mobility of the subnetworks can be incorporated [4]. Further in [7], three heuristic approaches for DDCA are presented and compared with a centralized method, centralized graph coloring. The distributed methods utilize local sensed interference power and SINR measurements and the performance is comparable with the centralized scheme. A combination between centralized and distributed interference management may also be of interest, so the subnetworks use centralized management when possible and distributed when out of range from the central controller.

The different resource allocation methods for in-X subnetworks decrease the interference, or in other words decrease the outage probability, however, the current methods mainly rely on current interference power measurements. Interference prediction has a potential to aid the interference mitigation techniques, since it will allow the resource allocation to be determined before the interference occurs [7], [9].

2.4 Existing Interference Predictors

Interference is a well-known problem in wireless communication, where the interference may cause an outage of a link, that is, the SINR drops below a certain threshold. Several interference mitigation methods have been developed, in order to decrease the interference amount. A proactive method is by predicting when the interference is below a certain threshold and then to transmit the message at the predicted time instance. This is particularly useful in cognitive radio networks, where the cognitive radio users can use licensed frequency bands when the primary users are not occupying them [9]. The cognitive radios then need to perform spectrum sensing, spectrum decision, spectrum mobility and lastly spectrum sharing. All of these could be improved with the use of interference prediction, as the real time sensing and decision making overhead are reduced, as well as the cognitive radios leave the channel before interfering with the primary users which is the case without prediction [9]. The usefulness of this method depends on the accuracy of the predictor. In order to design an accurate predictor it has to be designed for a model which reflects the interference pattern.

The authors of [17], have in [20] designed a simple interference predictor based of the $K \leq 5$ strongest interfering nodes. The predictor has a setup phase, where the different 2^K interference values are calculated and stored together with their transcodes, in a table, reflecting which nodes were transmitting. In the learning phase, real interference values are measured and stored in a new table with the previous transcodes. The new table takes far away interference into account. While measuring the interference, the message length and message probability is estimated for each of the K nodes. In the predicting phase, the predictor assumes that if a node is idle it will remain idle in the next time step, and if it is transmitting it will transmit in the next time step unless it has been transmitting for the estimated message length, then it is idle in next time step. Doing this for each K nodes, the predictor predicts a transcode for the next time step, and a corresponding interference value is found in the table made in the learning phase. The predictor can then be used multiple times to predict more time steps ahead. A flaw with this predictor is that it does not utilize the estimated message probabilities. Hence, in its prediction it does not account for new messages. The predictor is tested by using it to perform a simple slot selection, on a Poisson network where the nodes transmit according to a Poisson arrival process and the message length is exponential distributed and the channel is subject to iid Nakagami fading and non-singular distance dependant path-loss. The slot selection algorithm is tested against a random slot selection which it outperformed.

The same authors as [20] has since then designed an interference predictor in [1] based on the correlation function they found in [17]. The new predictor is based on an autoregressive moving average (ARMA) approximation of the ACF where the ARMA coefficients are used in a linear Kalman filter to predict the next interference samples. It was found that the predictor performs better if it is used in a network without channel sensing, this is because it is designed using an interference model where the nodes transmit according to a probability with fixed message duration, hence it does not account for channel sensing. The predictor was tested on interference simulated according to long term evolution (LTE), wireless sensor network (WSN) and Wi-Fi and yielded promising results.

Other kinds of predictors are channel predictors which tries to predict whether or not there is significant interference on a channel, for instance hidden Markov models with binary states can be trained and used to predict states for whether a channel is free or not [9], [27]. Further ARMA models have proven useful as predictors in channel sensing, spectrum decision and spectrum mobility [9].

2.5 Problem Statement

There is a lack of models and analytical expressions regarding the interference in the in-X subnetworks as they have recently been envisioned and a lot of research still has to be made. Since the different user applications need to be modelled differently we chose to focus on the in-robot subnetworks in a factory setting. The already existing interference predictors have been designed with an outset in the existing networks, so it would be interesting to see how such predictors perform on the in-robot subnetworks. It would further be interesting to see, if it is possible to design new interference predictors with an outset in a new model describing the in-robot subnetworks. This has lead up to the following problem statement.

"How can a mathematical model be made to realistically capture the interference power in in-robot subnetworks in a factory setting, and how can the interference power from this model be predicted? Additionally, is it possible to find statistics for the interference power from such a model?"

3. Description of Interference Model

In this chapter, the interference model is described along with all of the individual components. Afterwards, the interference power will be described using a more mathematical approach, and the mean and ACF of the interference are derived under the described model.

For simplicity, we consider the interference at \mathbf{x}_1 which is the location of the first control unit. Let M be the number of subnetworks and N the number of sensor and actuator pairs in each subnetwork. Then the interference at control unit \mathbf{x}_1 at time t is given as

$$\begin{aligned}
 I_{\mathbf{x}_1}(t) = & \sum_{k=2}^M h_{k0}^2(t) \ell(\mathbf{x}_k - \mathbf{x}_1) \gamma_{1k0}(t) \zeta(\mathbf{x}_1, \mathbf{x}_k) \\
 & + \sum_{k=2}^M \sum_{j=1}^N h_{kj}^2(t) \ell(\mathbf{x}_{kj} - \mathbf{x}_1) \gamma_{1kj}(t) \zeta(\mathbf{x}_1, \mathbf{x}_{kj})
 \end{aligned} \tag{3.1}$$

where $h_{k0}^2(t)$ is the small-scale fading on the link from the control unit in the k -th subnetwork to \mathbf{x}_1 at time t , $\ell(\mathbf{x}_k - \mathbf{x}_1)$ is the path-loss from the control unit of subnetwork k to \mathbf{x}_1 and $\gamma_{1k0}(t)$ is the traffic function, that is, an indicator function equalling 1 if the control unit of subnetwork k transmits at time t and the subnetwork is in the same channel group as the first subnetwork. Lastly, $\zeta(\mathbf{x}_1, \mathbf{x}_k)$ is the shadow effect between \mathbf{x}_1 and \mathbf{x}_k . Analogously, $h_{kj}^2(t)$, $\ell(\mathbf{x}_{kj} - \mathbf{x}_1)$, $\gamma_{1kj}(t)$ and $\zeta(\mathbf{x}_1, \mathbf{x}_{kj})$ are the fading, path-loss, traffic function and shadowing effects between \mathbf{x}_1 and the j -th sensor in the k -th subnetwork at time t .

In the following sections the individual components will be described, that is, the small-scale fading, path-loss, traffic function and shadowing, along with a description of the models for deployment and mobility of the subnetworks.

3.1 Model Description

Traffic model

The traffic function γ_{1k0} is an indicator function equaling one if \mathbf{x}_k transmits at the same time and channel as we are measuring \mathbf{x}_1 at. Hence, γ describes the traffic in the

	T_{UL}				T_{DL}				T_{UL}			
SN1	1_{UL}	2_{UL}	3_{UL}	4_{UL}	1_{DL}	2_{DL}	3_{DL}	4_{DL}	2_{UL}	4_{UL}	3_{UL}	1_{UL}
	3_{UL}	4_{UL}	2_{UL}	1_{UL}	3_{DL}	4_{DL}	2_{DL}	1_{DL}	4_{UL}	1_{UL}	2_{UL}	3_{UL}
	T_{DL}		T_{UL}				T_{DL}				T_{UL}	
SN2	1_{DL}	3_{DL}	3_{UL}	2_{UL}	1_{UL}	4_{UL}	3_{DL}	2_{DL}	1_{DL}	4_{DL}	3_{UL}	1_{UL}
	3_{DL}	4_{DL}	1_{UL}	4_{UL}	3_{UL}	2_{UL}	1_{DL}	4_{DL}	3_{DL}	2_{DL}	4_{UL}	2_{UL}
	TU											

Table 3.1: Depiction of the frame structures of two subnetworks. Note that the transmission order is the same from UL to DL and that the transmission order is shuffled in the next frame. Additionally, note the synchronization mismatch between the subnetworks, as a consequence subnetwork 1 (SN1) may receive both UL and DL interference from SN2, see 1_{UL} as an example.

network. For the traffic we will only consider where Time Division Duplexing (TDD) is used. We assume cyclic transmission patterns where a frame duration is $T_F = 0.1$ [ms]. The frame duration can be divided into sub-frames $T_F = T_{UL} + T_{DL}$. During the first part, all of the sensors transmit to the control unit (uplink), and in the second part the control unit transmits to all the actuators (downlink). We assume that the duration of the uplink (UL) and downlink (DL) is the same, $T_{UL} = T_{DL}$, as we have the same number of sensors and actuators. The sub-frames can further be divided into N_{TU} time units (TUs), where a TU is the transmission time from either a sensor to the control unit or the control unit to an actuator. This concept is illustrated in Table 3.1. During the UL all the sensors transmit one at a time, each taking a TU. Afterwards in the DL, the control unit transmits to the corresponding actuators in the same order as it received transmissions from the sensors. The order of the transmissions within the sub-frames are shuffled each frame, this helps circumvent jamming attacks, we will refer to this shuffling of each frame as random activity. Additionally, all the TUs do not have to be occupied, so we may have some empty TUs, for instance if we only had $N = 3$ devices then device 4 could be removed from Table 3.1.

The subnetworks do not work on the same clock, that is, there is a synchronization mismatch which we assume is a factor of a TU. A consequence of the synchronization mismatch, is that the UL and DL phases are not necessarily aligned in time across subnetworks.

As mentioned in Section 2.3.5, in order to lower the interference and latency, multiple channels and channel hopping in conjunction with blind repetition are used for in-X subnetworks (for more information about channel hopping and blind repetition see [8]). First we split the channels into K channel groups where K is chosen such that there is an equal number of channels in each group. The subnetworks are assigned to the channel groups uniformly, such that on average there are $N_{sg} = M/K$ subnetworks in a channel group. Let N_{cg} be the number of channels in each channel group. Then the messages are repeated blindly $N_{cg} - 1$ times, that is, once on each channel in the channel group, as is seen for both of the subnetworks in Table 3.1 for

	T_{UL}				T_{DL}				T_{UL}			
SN1	1_{UL}	2_{UL}	3_{UL}	4_{UL}	1_{DL}	2_{DL}	3_{DL}	4_{DL}	2_{UL}	4_{UL}	3_{UL}	1_{UL}
	T_{DL}		T_{UL}				T_{DL}			T_{UL}		
SN2	1_{DL}	3_{DL}	3_{UL}	2_{UL}	1_{UL}	4_{UL}	3_{DL}	2_{DL}	1_{DL}	4_{DL}	3_{UL}	1_{UL}
	TU											

Table 3.2: Depiction of the frame structures of two subnetworks with $N_{cg} = 1$.

the case of two channels in each group. We then have that, when a sensor transmits a message on one channel it repeats the same message on the other channels with a small delay between each transmission. However, since we only focus on the interference on one channel, which could be any of the channels, we will not model this blind repetition, this results in Table 3.2 instead of Table 3.1

Let N_{TU} be the number of TUs during UL or DL and N be the number of active sensor actuator pairs. Then, the expected value of the traffic function for the link between control units of the 1-st and k -th subnetwork is given by

$$\mathbb{E}[\gamma_{1k0}] = \mathbb{P}(\gamma_{1k0} = 1) \quad (3.2)$$

$$= \frac{N}{N_{TU}} \frac{T_{DL}}{T_F} \frac{N_{sg} - 1}{M - 1} \quad (3.3)$$

$$= \frac{N(N_{sg} - 1)}{2N_{TU}(M - 1)}. \quad (3.4)$$

In Eq. (3.3) the first fraction is the probability of the k -th control unit interfering given that the k -th subnetwork is doing DL and is in the same channel group as the first subnetwork, the second fraction is the probability of a subnetwork doing DL and the third fraction is the probability of another subnetwork being in the same channel group as the first subnetwork. Eq. (3.4) holds since we have that $T_{DL}/T_F = 1/2$. For the traffic function for the sensors we have

$$\mathbb{E}[\gamma_{1kj}] = \frac{TU}{T_F} \frac{N_{sg} - 1}{M - 1} \quad (3.5)$$

$$= \frac{N_{sg} - 1}{2N_{TU}(M - 1)}. \quad (3.6)$$

In Eq. (3.5), the first fraction is the probability of a single sensor interfering given that the k -th subnetwork is in the same channel group as the first subnetwork, whereas the second fraction is the probability of the sensor being in the same channel group as the first subnetwork.

Small-scale Fading Component

The small scale fading is modelled using Rayleigh fading which in turn is simulated using Jake-Doppler's model, specifically we have used the reformulated fading

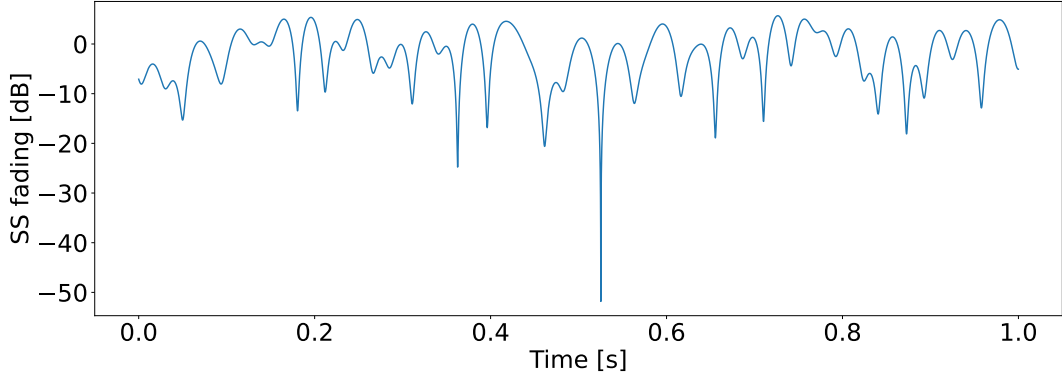


Figure 3.1: A plot of $|h_l(t)|^2$ for a single link, where $L_0 = 20$ and $f_c = 3$ [GHz].

model in [28]. When using Jake's model, we assume that we have L rays arriving with angles $\alpha_n = 2\pi(n - 0.5)/L$, such that the n -th ray has a Doppler shift $\omega_n = (2\pi f_c \nu / c) \cos(\alpha_n)$, where f_c is the carrier frequency, ν the velocity of the subnetworks and c is the speed of light. Using $L_0 = L/4$ complex oscillators, Jake's model for time t yields

$$h_l(t) = \sqrt{\frac{2}{L_0}} \sum_{n=1}^{L_0} (\cos(\beta_n) + j \sin(\beta_n)) \cos(\omega_n t + \theta_{n,l}) \quad (3.7)$$

where β_n are the phases and $\theta_{n,l}$ are the initial phases where $\theta_{n,l} \sim \mathcal{U}(0, 2\pi)$ and l denotes the specific link between \mathbf{x}_1 and the interfere that is either a sensor or control unit from another subnetwork. It should be noted that it is more likely to receive interference on a link from a control unit than a specific sensor. The phases β_n are chosen as

$$\beta_n = \frac{n\pi}{L_0} \quad \text{for } n = 1, 2, \dots, L_0. \quad (3.8)$$

This provides the same power for the real part and imaginary part and makes them uncorrelated. Further the normalization $\sqrt{2/L_0}$ makes it so

$$\mathbb{E}[h_l^2(t)] = 1. \quad (3.9)$$

An example of small scale fading is shown in Figure 3.1 for $|h_l(t)|^2$ with $L = 20$, a carrier frequency of $f_c = 3$ [GHz]. When we measure interference, we may receive interference from a different link for each frame, as can be seen from the frame structure in Table 3.2, which makes the small scale fading look like Figure 3.2.

When generating correlated Rayleigh fading using Jake-Doppler's model, the ACF should approximately follow the same pattern as the zeroth-order Bessel function of first kind [28], specifically

$$\text{Re} \left\{ \frac{\mathbb{E}[h_l(t)h_l(t+\tau)] - \mathbb{E}[h_l(t)]\mathbb{E}[h_l(t+\tau)]}{\sigma_{h_l}(t)\sigma_{h_l}(t+\tau)} \right\} \approx J_0(2\pi\nu\tau f_c/c) \quad (3.10)$$

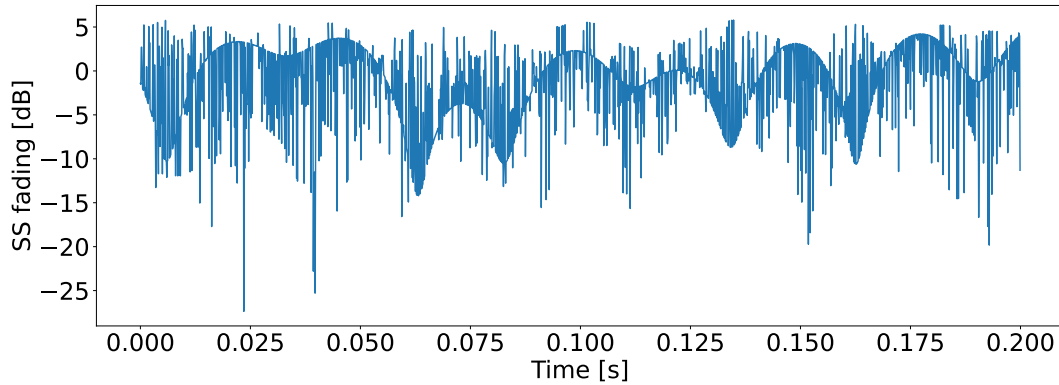


Figure 3.2: A plot of $|h_l(t)|^2$ where $L_0 = 20$, $f_c = 3$ [GHz] and the chosen link varies for each time step.

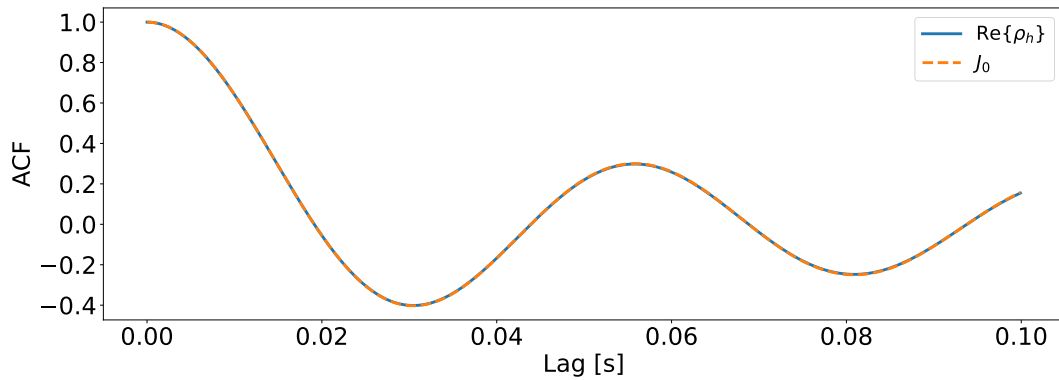


Figure 3.3: The real part of an empirical ACF of h and the zeroth order Bessel function of the first kind. The empirical ACF has been made by averaging over 1024 realizations with 10^6 points and a sample frequency of 10000 [Hz].

where J_0 is the zeroth order Bessel function of first kind and σ_{h_l} is the standard deviation of h_l . A comparison of an empirical ACF and the Bessel function is shown in Figure 3.3. Furthermore, the ACF of $|h_l|^2$ can be approximated by $J_0^2(2\pi\nu\tau f_c/c)$, as can be seen in Figure 3.4. For ease of notation we will use h_l^2 instead $|h_l|^2$ for the remainder of this project.

Path-loss

To model the path-loss a non-singular distance dependant path-loss model is used [17], specifically

$$\ell(\mathbf{x}_k - \mathbf{x}_1) = \min(1, \|\mathbf{x}_k - \mathbf{x}_1\|_2^{-\alpha}). \quad (3.11)$$

A plot of the path-loss as a function of distance can be seen in Figure 3.5, for $\alpha = 3$. The changes in distance is caused by the mobility of the nodes. Our mobility model is described later in this section.

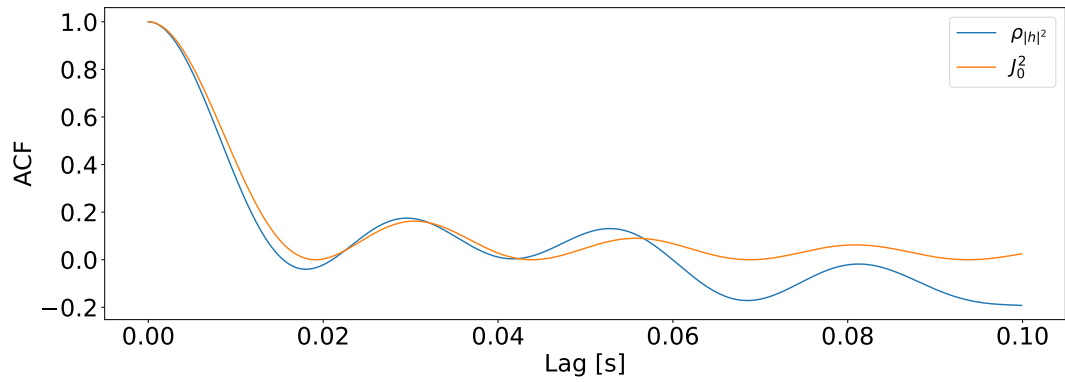


Figure 3.4: Empirical ACF of the small scale fading $|h_l|^2$ and the zeroth order Bessel function of the first kind squared. The empirical ACF has been made averaging over 1024 realizations with 10^6 points and a sample frequency of 10000 [Hz].

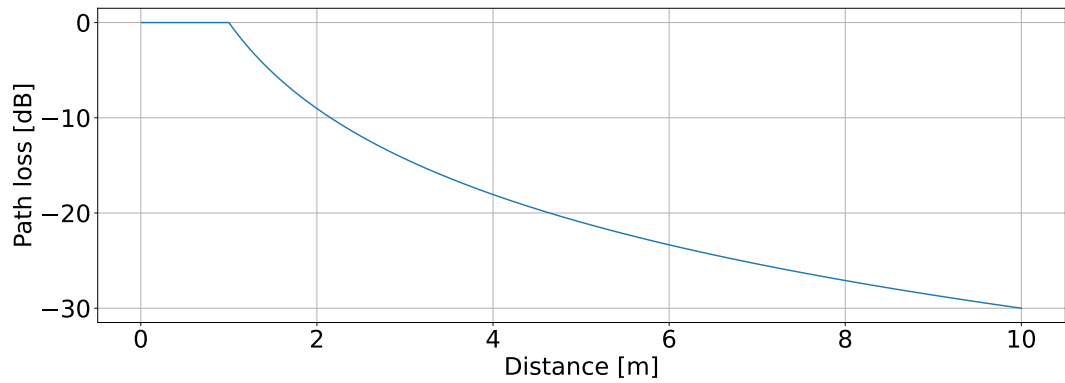


Figure 3.5: Path-loss as a function of distance using Eq. (3.11) with $\alpha = 3$.

Shadowing

We will use a similar shadowing model as [29], that is a log-normal random field, since it is argued that correlated shadow is more realistic, as ignoring the correlation will over-estimate the diversity of adjacent or closely located links [30]. In order, to describe the log-normal random field, we will focus on the Gaussian random field in the following. In the beginning of a snapshot a Gaussian random field is generated on a grid. Let Δ be the spacing along the grid, then we have a grid containing $(width \times height)/\Delta^2$ points on the random field f . We then have Gaussian random variables with the following covariance at the grid points

$$\text{cov}(f(\mathbf{s}), f(\mathbf{t})) = \sigma_s^2 e^{-\frac{\|\mathbf{s}-\mathbf{t}\|_2}{\delta}} \quad (3.12)$$

where δ is the decorrelation distance, σ_s^2 is the variance of the shadow map and $f(\mathbf{s})$ and $f(\mathbf{t})$ are Gaussian random variables at the points \mathbf{s} and \mathbf{t} in the grid, respectively. We have calculated the shadow map using an algorithm that utilizes circulant embedding which is described in [31, p. 374]. In Figure 3.6a a shadow map using the parameters $\sigma_s^2 = 3$, $\delta = 5$ and $\Delta = 1/20$ is seen. In Figure 3.6b we see a histogram of the values of the shadow map. The mean and variance of the values in the histogram are -0.21951 and 3.36746 , respectively, which are fairly close to the true mean and variance which are 0 and 3 , respectively. However, we do not always see this close of a representation of the mean and variance. We have simulated 1024 shadow maps and found the mean and variance for each of the maps, these can be seen in two histograms in Figure 3.7. This means that the shadow map and how it is distributed changes a lot between each realization.

The shadowing component is modelled in dB according to

$$\tilde{\zeta}(\mathbf{x}_1, \mathbf{x}_k) = \frac{1 - e^{(-d_{1k}/\delta)}}{\sqrt{2}\sqrt{1 + e^{(-d_{1k}/\delta)}}} (f(\mathbf{x}_1) + f(\mathbf{x}_k)) \quad (3.13)$$

where d_{1k} is the distance between the control units from the 1-st and k -th subnetwork. The shadowing component is calculated similarly for links involving sensors and actuators. The shadowing component in the linear scale is then given as

$$\zeta(\mathbf{x}_1, \mathbf{x}_k) = 10^{\tilde{\zeta}(\mathbf{x}_1, \mathbf{x}_k)/10}. \quad (3.14)$$

In Figure 3.8, we have plotted the shadow values against distance on a scatter plot. Here it is seen that the further the distance between the subnetworks, the bigger the spread of the shadow values. This increase continues until we reach a distance of approximately 7-8 meters, then the spread remains somewhat constant.

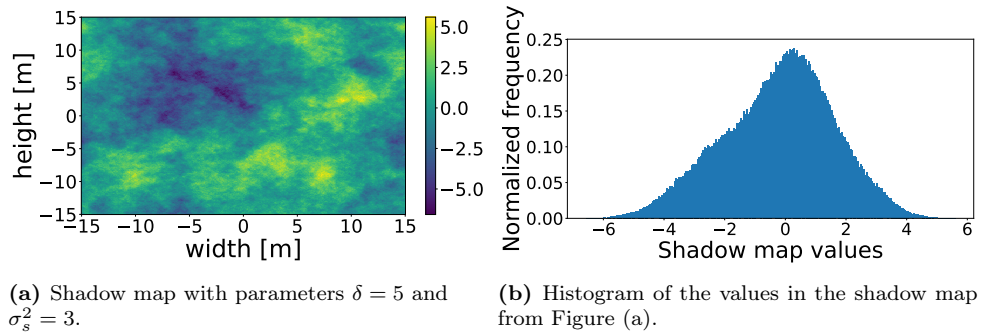


Figure 3.6

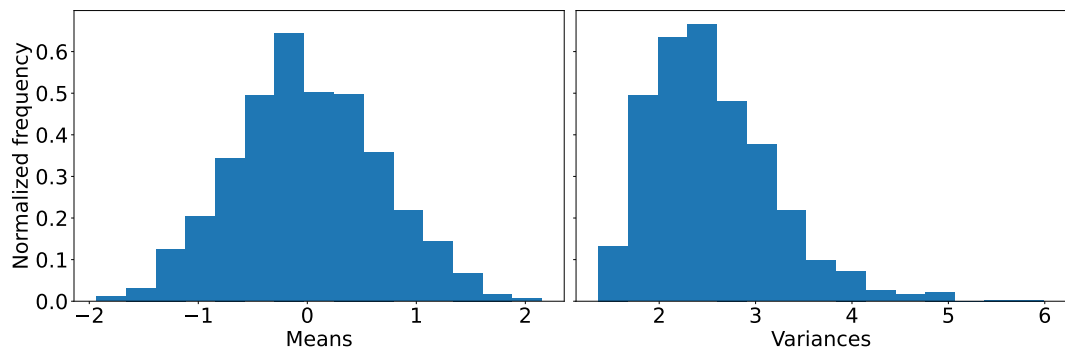


Figure 3.7: Histograms of the means and variances found for 1024 different shadow maps generated with the parameters $\sigma_s^2 = 3$, $\delta = 5$ and $\Delta = 1/20$.

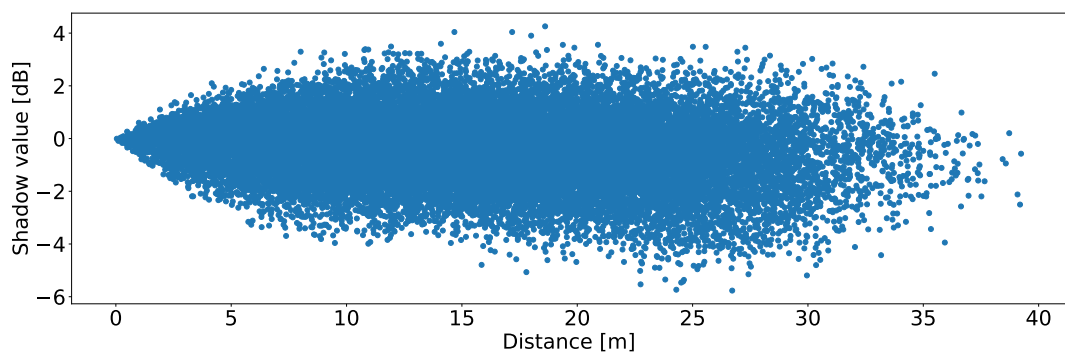


Figure 3.8: Scatter plot of values from shadowing versus distance using 25000 points. The shadow map used is the one shown in Figure 3.6a

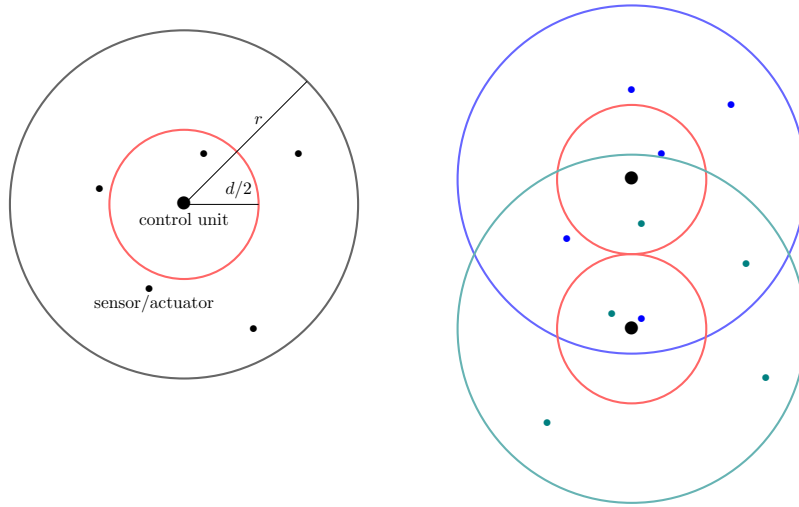


Figure 3.9: Left: Illustration of an in-X subnetworks model with radius r and 5 sensor actuator pairs, the red circles represent half of the minimum distance d . Right: Illustrates two subnetworks colliding, where the sensor actuator pairs are the same color as the cell radius for each of the subnetworks. In this case $d = r$, and an overlap is possible.

Deployment and Mobility

In our work, we have chosen to focus on in-robot subnetworks in a factory setting. That is the subnetworks are placed in a rectangular room and can move around freely, in the form of robots, as long as they maintain a minimum distance to each other. We assume that each of these subnetworks has the same number of sensor actuator pairs. Furthermore, that these pairs are co-located randomly throughout the cell of the subnetwork as seen in Figure 3.9. When the subnetworks comes within the minimums distance of each other or comes within a radius of a wall a new direction is drawn randomly.

As in Figure 3.10, we have chosen a square room. We assume that the number of subnetworks is known before deployment. When deploying a new subnetwork it cannot be placed arbitrarily close to already deployed subnetworks. Say the subnetworks have a cell radius r and there should be a minimum distance d between the centers of each of the subnetworks. Furthermore, if $d < 2r$ then the subnetwork cells can overlap, see Figure 3.9. Let A be the area of a factory hall, then the radius of the subnetworks r will result in a deployment area $\tilde{A} = A^{\ominus r}$ which is an erosion of the area, A , by r . This can also be seen in Figure 3.10. The first subnetwork is placed uniformly in \tilde{A} whereas the second is placed uniformly in \tilde{A} with a circle with radius d and center at the first subnetwork removed. In general the deployment of the k -th subnetwork is conditioned on the deployment of the previous $k - 1$. Specifically, the k -th subnetwork is placed uniformly in \tilde{A} with areas removed such that the center of the k -th subnetwork is at least a minimum distance away from the other subnetworks.

Initially, each of the subnetworks draws a random direction uniformly in the

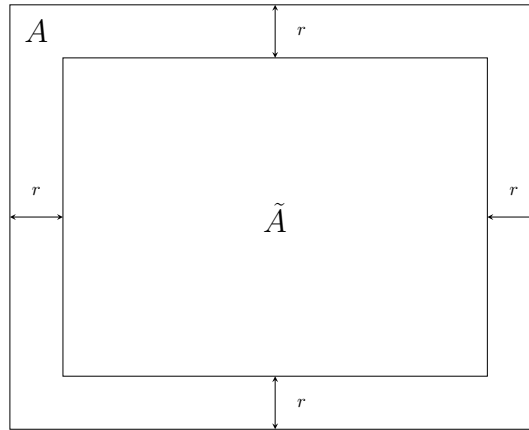


Figure 3.10: Illustration of the deployment area \tilde{A} .

interval $[0, 2\pi)$. All the subnetworks move with the same velocity ν in their respective directions, until they meet a wall or another subnetwork, then a new direction is drawn uniformly in the interval $[0, 2\pi)$. If two subnetworks collide both of them gets a new direction.

In Figure 3.11 there is shown an example of a deployment of $M = 16$ subnetworks within $A = [-15, 15]^2$, with a minimum distance of $d = 3$ [m] and radius of $r = 2$ [m]. The deployment is at time $t = 0$ [s] and then the subnetworks move in a random direction with a velocity of $\nu = 2$ [m/s]. The outer ring is the radius of the subnetwork r and the inner ring has radius $d/2$. The color of the subnetworks indicate the channel group that they belong to. Here we also see that the number subnetworks in each channel group can vary a lot.

Simulating Interference in in-X Subnetworks

In this section, we simulate interference from the interference model described throughout this chapter. Additionally, we want to investigate how the simulated interference samples are distributed and correlated. The simulation settings are found in Table 3.3. The simulated interference as well as the path-loss, small scale fading and shadowing are plotted in Figure 3.12 for the first 0.2 [s] (2000 samples) of a snapshot. In order to see the effects of only one interfere, the interference was simulated where the first subnetwork is in a channel group with only one other subnetwork. In general, in the snapshots the first subnetwork is not constrained to be in a channel group with only one other subnetwork, but the number of subnetworks assigned to a certain channel is random as shown in Figure 3.11.

We want to investigate how the interference samples are distributed, therefore 1024 snapshots have been simulated, and a histogram has been made using all the interference samples. For the simulations the number of channel groups is set to 4. The histogram of the interference samples is seen in Figure 3.13a.

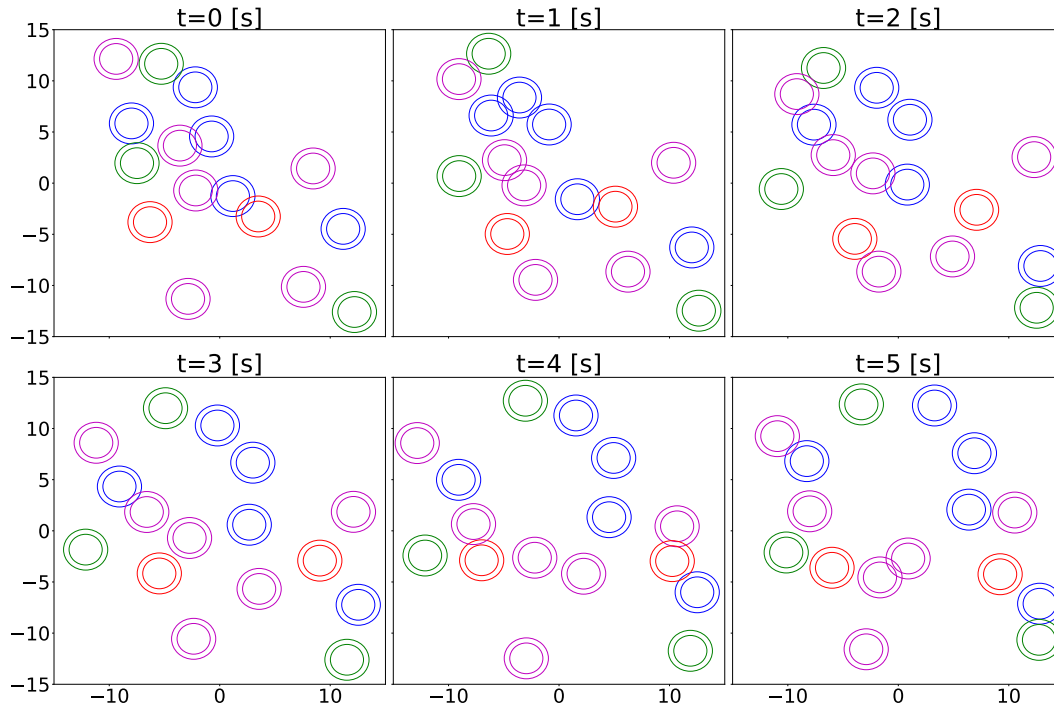


Figure 3.11: Illustration of in-factory subnetworks, where we have $M = 16$ subnetworks within $A = [-15, 15]^2$, with a minimum distance of $d = 3$ [m] and radius of $r = 2$ [m]. The deployment is at $t = 0$ [s], afterwards they move with velocity $\nu = 2$ [m/s], in a random direction. The outer ring denotes the cell radius and the inner half of the minimum distance. There are 4 channel groups, and the subnetworks are colored according to the assigned channel group.

Parameter	Value
Number of subnetworks, M	16
Number of sensor actuator pairs, N	18
Cell radius, r	2 [m]
Room size	30×30 [m ²]
Minimum distance, d	3 [m]
Velocity, ν	2 [m/s]
Carrier frequency, f_c	3 [GHz]
Path-loss exponent, α	3
Number of waves, L_0	20
Variance of shadow map, σ_s^2	3
Decorrelation distance, δ	5 [m]
Step size in the shadow map, Δ	1/20 [m]
Number of snapshots	1024
Simulation time	30 [s]
Sample frequency	10 [kHz]

Table 3.3: Settings used for simulating interference power using the in-X interference model.

From the histogram it is observed that the interference samples are almost normally distributed in the dB scale, that is, the interference samples are log-normally distributed in the linear scale.

Beside the distribution of the interference samples, we also want to examine how the samples are correlated. In order to assess how the interference samples are correlated, we have calculated an empirical ACF of the interference samples for each snapshot and then averaged over the 1024 snapshots to obtain an estimate of the ACF. The ACF of the interference samples is seen in Figure 3.13b.

From Figure 3.13b it is seen that the ACF decreases really fast, meaning that given previous samples we will have very little information to predict the future samples. We conjecture that the rapidly decreasing ACF is due to random activity, that is, the shuffling of the transmission order for each time frame. In order to investigate this conjecture, we will perform a test of predictability in order to implement and analyse the interference in in-X subnetworks.

3.2 Test of Predictability in Order to Implement and Analyse the Interference in in-X Subnetworks

In this section we have tested the predictability of the interference power for different setups. First we have an initial test, where it is seen that when random activity is off the ACF is greater. Afterwards, we see that when random activity is off it does not make a difference how many sensors there are but only the relation between T_{UL} and T_{DL} . Then there will be made tests on different scenarios given only one sensor in each subnetwork. At the end we describe the changes this causes to the model.

As we saw in the previous section, the ACF of the interference power decreases very fast (see Figure 3.13b). We suspect that this is because of the random activity. Thus we have simulated 1024 snapshots where random activity is off, the ACF and distribution of the interference samples from these snapshots are seen in Figure 3.14. If we look at Figure 3.14b we see that the ACF is greater by a big margin compared to the ACF when random activity is on. Furthermore, we also see in Figure 3.14a that the interference samples in the histogram are still normal distributed in dB scale.

When there is no random activity, we argue that the number of sensors does not matter but only the relation between T_{UL} and T_{DL} . This is due to the fact that, if we receive interference from a sensor in one time step, we will receive interference from the same sensor for all time steps, and the fact that the placement of all the sensors follow the same distribution. Thus, when simulating data we only need to place one sensor for each subnetwork.

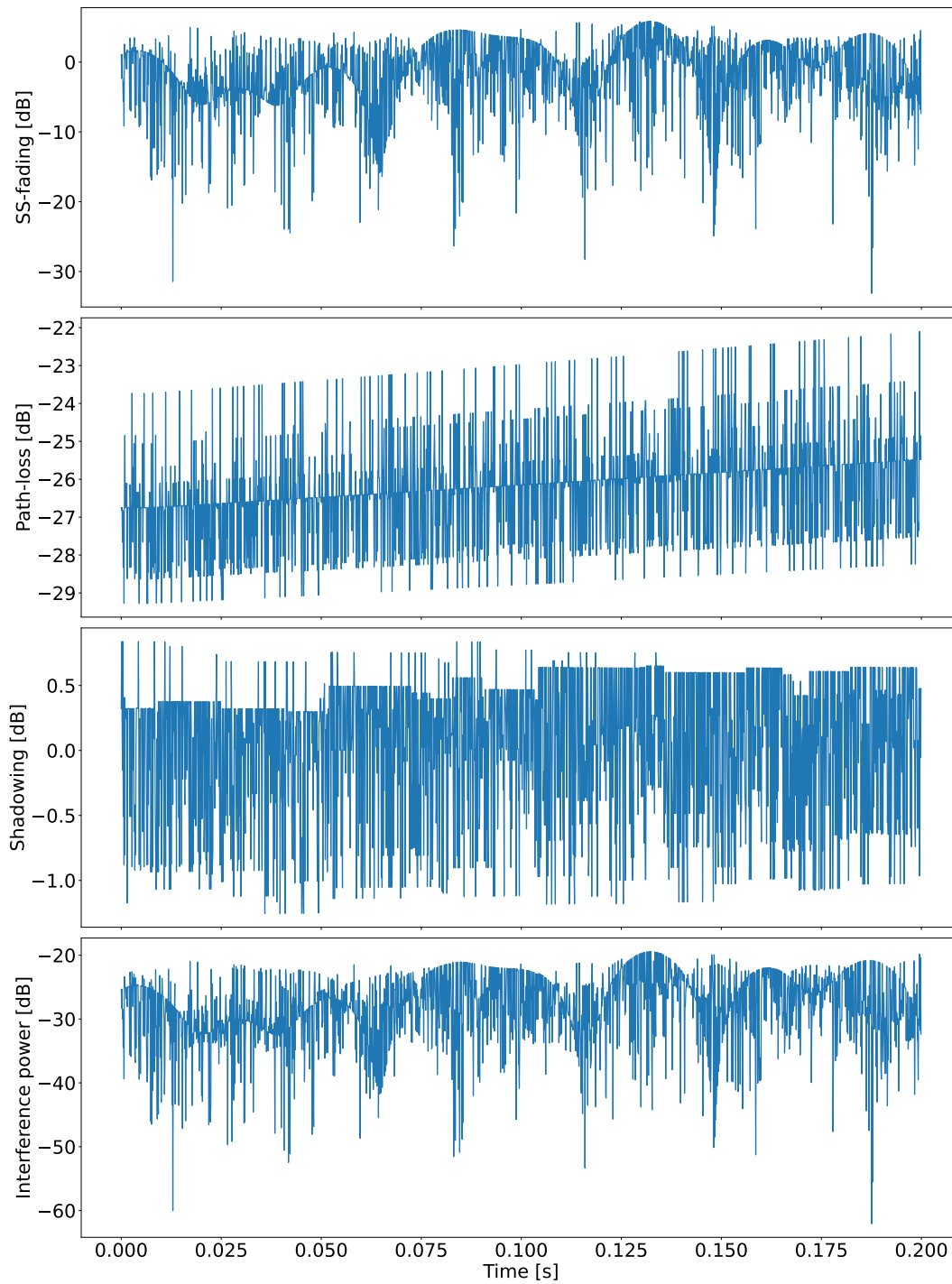


Figure 3.12: Plot of the interference power as well as plots of the components constituting the interference power, that is, the small-scale fading, path-loss and shadowing. This is done in the case where there is only one other subnetwork in the channel group as the first subnetwork.

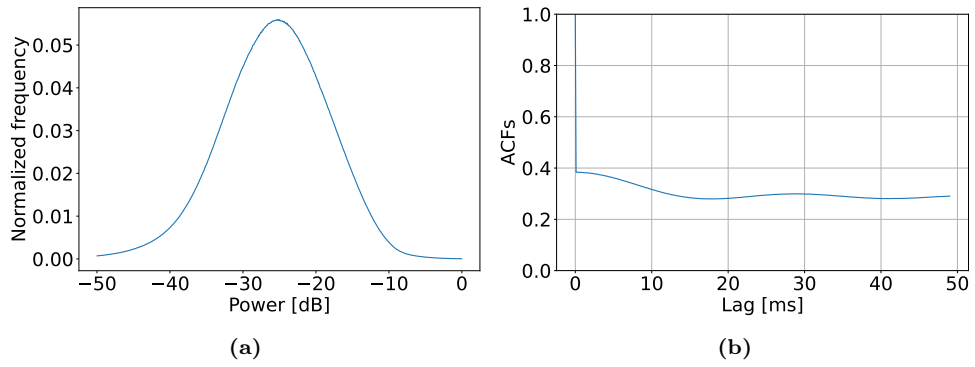


Figure 3.13: A histogram (a) and an ACF (b) of interference simulated from the interference model using the settings in Table 3.3.

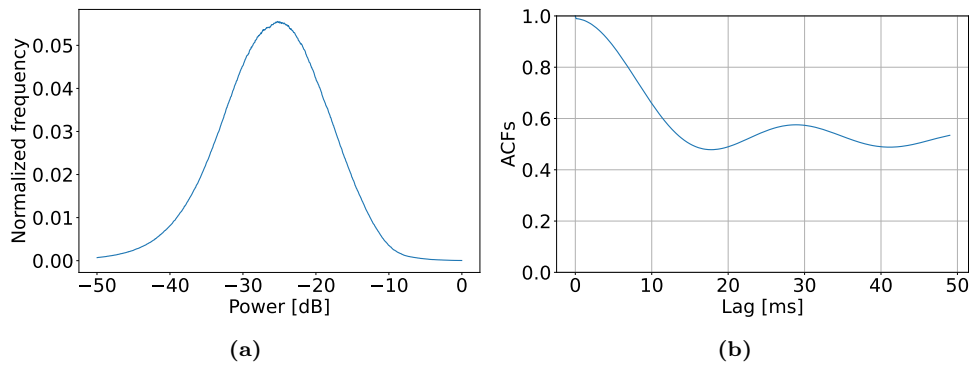


Figure 3.14: A histogram (a) and an ACF (b) of interference simulated from the interference model using the settings in Table 3.3, with random activity turned off.

Scenario	Misalignment	Number of Channels
1	off	4
2	off	1
3	on	4
4	on	1
5	fractional	1

Table 3.4: Settings for the different scenarios to be tested.

We will now test the interference model for five different scenarios which can be seen in Table 3.4. The simulation settings that we change in the different scenarios are misalignment and the number of channels. These scenarios are selected to examine the difference in the interference power, when receiving from sensors only compared to receiving from a combination of sensors and control units. Furthermore, the effect of different amount of subnetworks interfering is also examined. Misalignment refers to the synchronization mismatch between the subnetworks. When this is on we can receive interference from both sensors and control units, whereas when it is off we only receive interference from sensors. In scenario 5, the misalignment is fractional, that is, we allow interference from both a sensor and a control unit from the same subnetwork, the scale of the contribution from the sensor is drawn randomly from $\{0, 0.25, 0.5, 0.75, 1\}$, and then the scale of the contribution from the control unit is chosen such that the sum of the scales equals one. As mentioned in Section 3.1, we only model one channel in a channel group, thus the number of channels is the same as the number of channel groups.

The simulations are once again made using the settings from Table 3.3, with number of sensor and actuator pairs set to one. We found that the interference power seems to follow a log-normal distribution for all the scenarios as seen in Figure 3.15a. In order to assess how well a log-normal distribution fits the interference power for the different scenarios, we have calculated the Kullback–Leibler divergence [32] between a normalized histogram of the interference power samples in dB and a fitted normal distribution. The discrete Kullback-Leibler divergence between two probability mass functions h and f is defined as

$$D(h||f) = \sum_{i=1}^{N_{bins}} h(x_i) \log \left(\frac{h(x_i)}{f(x_i)} \right). \quad (3.15)$$

The Kullback-Leibler divergence is a measure of the inefficiency of assuming a distribution f when the real distribution is h , the closer the value gets to zero the better f fits. In our case, we set the normalized histogram as the real distribution. We use $N_{bins} = 1024$ bins in the range $[-50, 0]$ [dB].

In Table 3.5 the mean interference power, the estimated parameters for the normal distribution in dB and Kullback-Leibler divergence for each scenario are found. In Figure 3.15b the ACFs for all the different scenarios are plotted. Here it is seen that

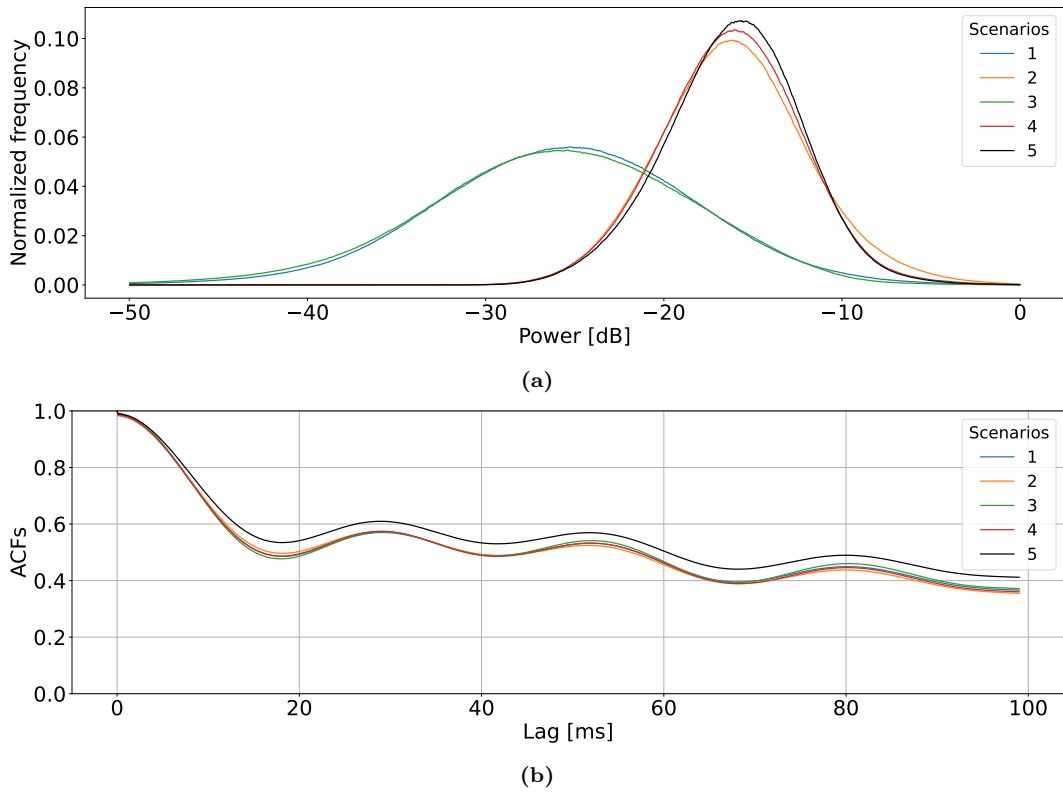


Figure 3.15: Histograms (a) and ACFs (b) of the interference from the different scenarios simulated from the interference model using the settings in Table 3.3.

the ACFs are all very close, in fact the ACFs for scenario 1-4 are placed almost on top of each other. It is observed that the ACF for scenario 5 is slightly above the other ACFs.

In Figure 3.16 we have a time trace of each of the scenarios. In the first time trace plot the interference power has been simulated from the original interference model with random activity turned off, that is, with 18 sensor actuator pairs. As mentioned earlier, we see that this corresponds to scenario 3 where 4 channel groups are used and misalignment is on.

From Table 3.5, it is seen that the mean interference and the distribution parameters of a scenario is similar in size to other scenarios with the same amount of channels. Additionally, looking at the values of the KL-divergences the interference samples seem to closely follow a log-normal distribution for all scenarios. Together with the parameters and the histogram in Figure 3.15a, it is seen that the interference for scenario 1 and 3 follows a distribution with a lower mean value and that the standard deviation (scale) is significantly larger when compared to the other scenarios. This is because for scenario 1 and 3 there are 4 channels, hence the channel groups have 4 subnetworks on average yielding a lower interference power. Additionally, since the number of subnetworks in each channel group is chosen randomly, and that

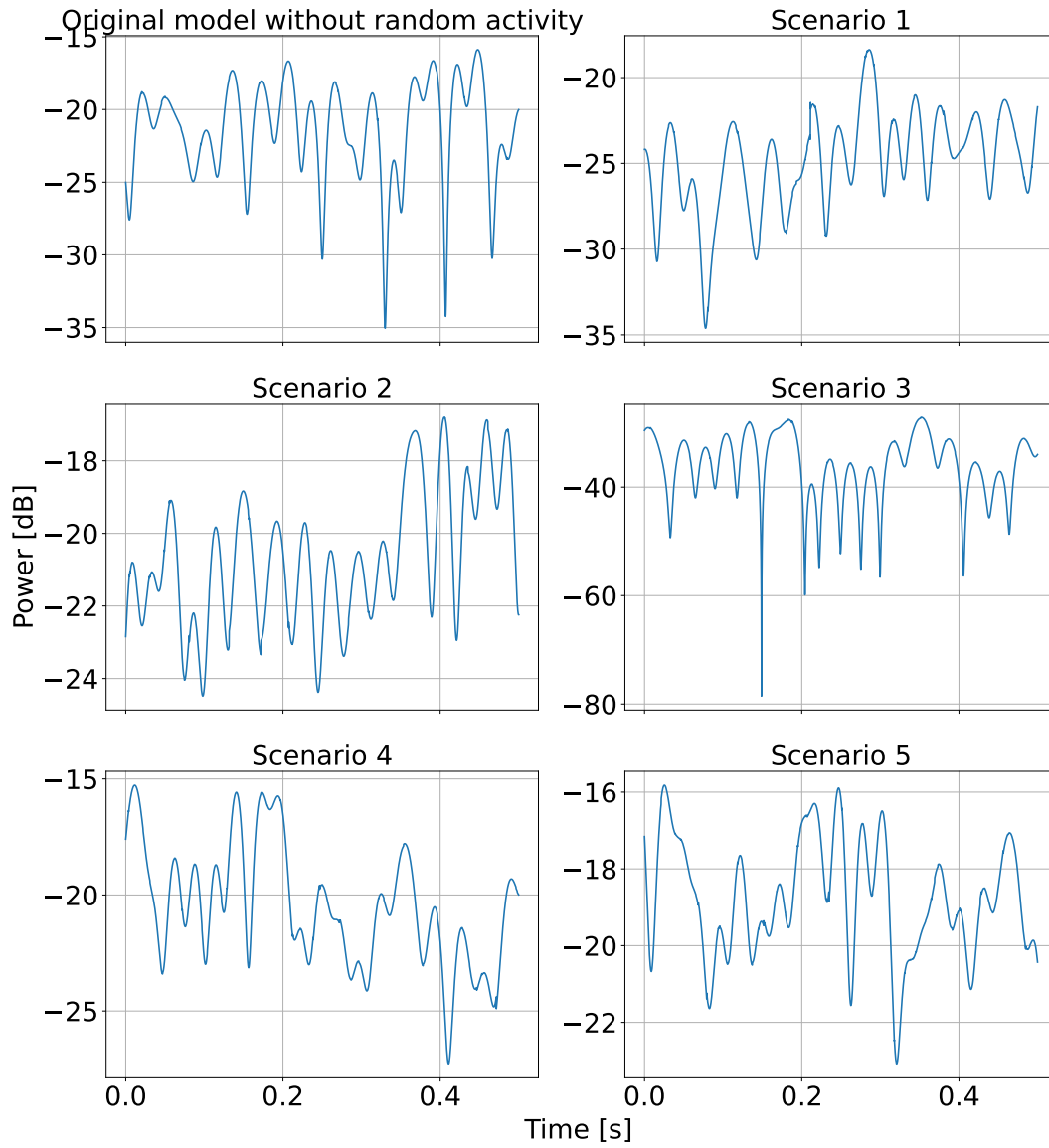


Figure 3.16: Time trace plots of the interference simulated from the original interference model without random activity as well as the interference from the 5 scenarios.

Scenario	Mean Interference [dB]	Log-Normal Parameters	KL-Divergence
1	-19.843	loc = -25.646 scale = 7.310	0.00170
2	-13.758	loc = -16.023 scale = 4.233	0.00458
3	-20.464	loc = -26.079 scale = 7.499	0.00548
4	-14.358	loc = -16.220 scale = 3.944	0.00218
5	-14.379	loc = -16.072 scale = 3.824	0.00305

Table 3.5: Results of the different scenarios from Table 3.4.

the interference power depends on the number of subnetworks in the channel group we are measuring, we have an increase in standard deviation (scale).

Looking at scenario 1 and 2, the mean interferences and the loc parameters are slightly higher compared to that of scenario 3 and 4, respectively. This is expected, as the misalignment is off for scenario 1 and 2, that is, we only receive interference from sensors. The distance between sensors and the control unit of the first subnetwork is sometimes less and sometimes greater than the distance between other control units and the first, since the sensors are randomly distributed inside the subnetwork cell while the control unit is at the center. Since the path-loss function is a nonlinear function which attenuates the interference received from greater distances, see Figure 3.5 when the sensor is closer to the control unit of the first subnetwork it increases the interference power more than it decreases the interference power when it is further away. As a result the received interference power will be slightly less when misalignment is on, compared to when misalignment is off.

3.2.1 Changes to the Model

Based on the ACFs in Figure 3.15b and Figure 3.13b and the plots of the interference time traces in Figure 3.16 and Figure 3.12, we deem that random activity should be turned off in order for the interference signal to be predictable. This changes the expected value of the traffic functions γ_{1k0} and γ_{1k1} from Eq. (3.3) and Eq. (3.5) to

$$\mathbb{E}[\gamma_{1k0}] = \frac{N_{sg} - 1}{2(M - 1)} \quad (3.16)$$

and

$$\mathbb{E}[\gamma_{1k1}] = \frac{N_{sg} - 1}{2(M - 1)}, \quad (3.17)$$

respectively. The expected values are equal to the product of two probabilities. The first probability is the probability of receiving interference from a sensor or a control unit from a subnetwork given that the subnetwork is in the same channel as the first subnetwork. Since we have from Section 3.1 that $T_{UL} = T_{DL}$, that is, an equal amount of time on UL and DL, the probability of receiving UL or DL interference at a given time is $1/2$. The second probability is the probability of being in the same channel group as the first subnetwork. When the average number of subnetworks per group is N_{sg} and there are M subnetworks this probability is $(N_{sg} - 1)/(M - 1)$.

3.3 Stochastic Interference Model

In this section we want to describe the interference model from the previous section more mathematically. Furthermore, we will derive the mean and covariance of interference power, using the interference model, and use these to find the ACF, this is done in Section 3.4. We start by describing the distribution of the placement of the subnetworks and the sensor actuator pairs. Afterwards, we will go through the derivations of the mean and ACF.

In Section 3.1 the deployment and mobility of the in-X subnetworks are described. We will use that as an outset to describe it from a stochastic geometry standpoint. To describe the placement of the subnetworks, we focus on the placement of the control units as they are at the centres of the subnetworks. Let

$$\Phi = \{\mathbf{x}_1, \mathbf{x}_2, \dots, \mathbf{x}_M\} = \{\mathbf{x}_{[M]}\} \quad \text{for } M > 0 \quad (3.18)$$

be the location of the control units where we use the notation $\mathbf{x}_{[M]}$ to denote the M first control units. This notation will also be used in other cases for example $f(\mathbf{x}_{[M]}) = f(\mathbf{x}_1, \mathbf{x}_2, \dots, \mathbf{x}_M)$ and $d\mathbf{x}_{[M]} = d(\mathbf{x}_1 \times \mathbf{x}_2 \times \dots \times \mathbf{x}_M)$.

The first control unit is placed uniformly over \tilde{A} resulting in a probability density function (pdf)

$$f(\mathbf{x}_1) = \begin{cases} \frac{1}{|\tilde{A}|}, & \text{for } \mathbf{x}_1 \in \tilde{A}, \\ 0, & \text{else} \end{cases} \quad (3.19)$$

where $|\tilde{A}|$ is the Lebesgue measure of \tilde{A} . When the second subnetwork is placed, it is conditioned on the location of the first one. Let $b(\mathbf{x}, r)$ be a circle in \mathbb{R}^2 with center at \mathbf{x} and radius r . Then the location of the control unit of the second subnetwork has the following pdf

$$f(\mathbf{x}_2|\mathbf{x}_1) = \begin{cases} \frac{1}{|\tilde{A} \setminus b(\mathbf{x}_1, d)|}, & \text{for } \mathbf{x}_2 \in \tilde{A} \setminus b(\mathbf{x}_1, d), \\ 0, & \text{else} \end{cases} \quad (3.20)$$

where the area of the first subnetwork is excluded to make sure that the position of the second subnetwork, \mathbf{x}_2 , is feasible. Generally, the conditional pdf of the location of the control unit of the n -th subnetwork is given by

$$f(\mathbf{x}_n|\mathbf{x}_{[n-1]}) = \begin{cases} \frac{1}{|\tilde{A} \setminus \bigcup_{k=1}^{n-1} b(\mathbf{x}_k, d)|}, & \text{for } \mathbf{x}_n \in \tilde{A} \setminus \bigcup_{k=1}^{n-1} b(\mathbf{x}_k, d), \\ 0, & \text{else.} \end{cases} \quad (3.21)$$

These pdfs corresponds to uniform distributions within the feasible areas. Say we want to deploy M subnetworks, to see that the conditional pdfs $f(\mathbf{x}_n|\mathbf{x}_{[n-1]})$ for $n \in [M]$ (where $[M] = \{1, 2, \dots, M\}$) are indeed valid pdfs consider

$$\int_{\mathbb{R}^2} f(\mathbf{u}_n|\mathbf{x}_{[n-1]}) d\mathbf{u}_n = \int_{\tilde{A} \setminus \bigcup_{k=1}^{n-1} b(\mathbf{x}_k, d)} f(\mathbf{u}_n|\mathbf{x}_{[n-1]}) d\mathbf{u}_n \quad (3.22)$$

$$= \frac{1}{|\tilde{A} \setminus \bigcup_{k=1}^{n-1} b(\mathbf{x}_k, d)|} \int_{\tilde{A} \setminus \bigcup_{k=1}^{n-1} b(\mathbf{x}_k, d)} 1 d\mathbf{u}_n \quad (3.23)$$

$$= 1. \quad (3.24)$$

Thus, we have that $f(\mathbf{x}_n|\mathbf{x}_{[n-1]})$ for $n \in [M]$ are valid pdfs, since they are non-negative and integrate to one. In the context of point processes, this defines M different binomial point processes (BPPs) each with one point, that is,

$$\mathbf{x}_n|\mathbf{x}_{[n-1]} \sim \text{Binomial}\left(\tilde{A} \setminus \bigcup_{k=1}^{n-1} b(\mathbf{x}_k, d), 1, f(\mathbf{x}_n|\mathbf{x}_{[n-1]})\right) \quad (3.25)$$

where the first entry of the BPP is the deployment area, the second entry is the number of points being deployed and the third entry is the density (for the definition of BPP see definition A.6). The location of the control units, Φ , are thus the superposition of these point processes.

We can use the conditional distributions to find the distribution of the point process [33, p. 165]

$$f(\mathbf{x}_{[M]}) = f(\mathbf{x}_2, \dots, \mathbf{x}_M|\mathbf{x}_1) f(\mathbf{x}_1) \quad (3.26)$$

$$\vdots$$

$$= \prod_{k=1}^M f(\mathbf{x}_k|\mathbf{x}_{[k-1]}). \quad (3.27)$$

If we consider the locations of the sensor actuator pairs in a subnetwork, then they can be described according to a BPP with a uniform pdf. Specifically, let

$$\Xi_k = \{\boldsymbol{\xi}_{k1}, \boldsymbol{\xi}_{k2}, \dots, \boldsymbol{\xi}_{kN}\} = \{\boldsymbol{\xi}_{k[N]}\} \quad (3.28)$$

be the location of sensor actuator pairs within the k -th subnetwork relative to the k -th control unit. The location of the pairs with respect to origin is found by adding the location of the control unit within the k -th subnetwork. That is, if we define

$$\Xi_k \sim \text{Binomial}\left(b(\mathbf{0}, r), N, \frac{1}{\pi r^2}\right) \quad \text{for } k \in [M], \quad (3.29)$$

then the positions of the sensor actuator pairs in the k -th subnetwork in A are given by

$$\Phi_k = \{\mathbf{x}_{k[N]}\} \quad (3.30)$$

where

$$\mathbf{x}_{ki} = \mathbf{x}_k + \boldsymbol{\xi}_{ki} \quad \text{for } i \in [N] \quad (3.31)$$

where \mathbf{x}_k is the location of the k -th control unit.

As we discussed in Section 3.2, we will focus on the case where $N = 1$, that is, each subnetwork only has one sensor actuator pair. Therefore, the mean and ACF will be derived for the case with one sensor in each subnetwork.

3.4 Derivation of the Mean and ACF of the Interference

In this section the goal is to derive the temporal ACF of the interference power which is particularly useful as it indicates how the interference samples are related over a certain time period. In order to obtain the ACF, we need to find expressions for the mean and the temporal covariance of the interference power. It is assumed that there is misalignment, that is, we may receive interference from both control units and sensors.

3.4.1 Derivation of the Mean Interference

In the following, the notation \mathbb{E}_Φ means that we take the expected value with respect to Φ . The mean interference at a control unit is derived using Eq. (3.1). For simplicity we consider the interference received at the first control unit, \mathbf{x}_1 , as the expected interference pattern should look similar across all control units.

$$\begin{aligned} \mathbb{E}[I_{\mathbf{x}_1}(t)] &= \mathbb{E}_{\Phi, \Phi_k, h, \gamma} \left[\sum_{k=2}^M h_{k0}^2(t) \ell(\mathbf{x}_k - \mathbf{x}_1) \gamma_{1k0}(t) \zeta(\mathbf{x}_1, \mathbf{x}_k) \right. \\ &\quad \left. + \sum_{k=2}^M h_{k1}^2(t) \ell(\mathbf{x}_{k1} - \mathbf{x}_1) \gamma_{1k1}(t) \zeta(\mathbf{x}_1, \mathbf{x}_{k1}) \right] \end{aligned} \quad (3.32)$$

$$\begin{aligned} &= \mathbb{E}_{\Phi, h, \gamma} \left[\sum_{k=2}^M h_{k0}^2(t) \ell(\mathbf{x}_k - \mathbf{x}_1) \gamma_{1k0}(t) \zeta(\mathbf{x}_1, \mathbf{x}_k) \right] \\ &\quad + \mathbb{E}_{\Phi_k, h, \gamma} \left[\sum_{k=2}^M h_{k1}^2(t) \ell(\mathbf{x}_{k1} - \mathbf{x}_1) \gamma_{1k1}(t) \zeta(\mathbf{x}_1, \mathbf{x}_{k1}) \right] \end{aligned} \quad (3.33)$$

$$= \mathbb{E}[I_{\mathbf{x}_1cu}(t)] + \mathbb{E}[I_{\mathbf{x}_1s}(t)]. \quad (3.34)$$

The first expected value in Eq. (3.34) is the expected interference received from other control units, and the second expected value is the expected interference received from sensors within the other subnetworks.

Starting with the expected interference received from the other control units, $\mathbb{E}[I_{\mathbf{x}_1cu}(t)]$, we have the following.

$$\mathbb{E}[I_{\mathbf{x}_1cu}(t)] = \mathbb{E}_{\Phi, h, \gamma} \left[\sum_{k=2}^M h_{k0}^2(t) \ell(\mathbf{x}_k - \mathbf{x}_1) \gamma_{1k0}(t) \zeta(\mathbf{x}_1, \mathbf{x}_k) \right] \quad (3.35)$$

$$= \mathbb{E}_{\Phi} \left[\sum_{k=2}^M \mathbb{E}_h[h_{k0}^2(t)] \ell(\mathbf{x}_k - \mathbf{x}_1) \mathbb{E}_{\gamma}[\gamma_{1k0}(t)] \zeta(\mathbf{x}_1, \mathbf{x}_k) \right] \quad (3.36)$$

$$= \frac{N_{sg} - 1}{2(M - 1)} \mathbb{E}_{\Phi} \left[\sum_{k=2}^M \ell(\mathbf{x}_k - \mathbf{x}_1) \zeta(\mathbf{x}_1, \mathbf{x}_k) \right] \quad (3.37)$$

where we used the fact, from Eq. (3.9) and Eq. (3.16), that $\mathbb{E}_h[h_{k0}^2(t)] = 1$ and $\mathbb{E}_{\gamma}[\gamma_{1k0}(t)] = \frac{N_{sg}-1}{2(M-1)}$. Let $\tilde{A}^M = \tilde{A} \times \tilde{A} \times \cdots \times \tilde{A}$ be \tilde{A} M -fold times. Then using the joint pdf in Eq. (3.27) to evaluate the expected value in Eq. (3.37) yields.

$$\mathbb{E}[I_{\mathbf{x}_1cu}(t)] = \frac{N_{sg} - 1}{2(M - 1)} \int_{\tilde{A}^M} \left(\sum_{k=2}^M \ell(\mathbf{u}_k - \mathbf{u}_1) \zeta(\mathbf{u}_1, \mathbf{u}_k) \right) f(\mathbf{u}_{[M]}) d\mathbf{u}_{[M]}. \quad (3.38)$$

We do not know of any methods to calculate the integral in Eq. (3.38) on closed form, so we need to use numerical methods to do so. Therefore, when evaluating the integral in Eq. (3.38) Monte Carlo (MC) integration will be used. MC integration is described in Appendix B.

Now turning to the expected interference received from the sensors from the other subnetworks, that is, $\mathbb{E}[I_{\mathbf{x}_1s}(t)]$.

$$\mathbb{E}[I_{\mathbf{x}_1s}(t)] = \mathbb{E}_{\Phi_k, h, \gamma} \left[\sum_{k=2}^M h_{k1}^2(t) \ell(\mathbf{x}_{k1} - \mathbf{x}_1) \gamma_{1k1}(t) \zeta(\mathbf{x}_1, \mathbf{x}_{k1}) \right] \quad (3.39)$$

$$= \mathbb{E}_{\Phi} \left[\sum_{k=2}^M \mathbb{E}_{\xi_k} \left[\mathbb{E}_h[h_{k1}^2(t)] \ell(\mathbf{x}_k + \xi_k - \mathbf{x}_1) \mathbb{E}_{\gamma}[\gamma_{1k1}(t)] \zeta(\mathbf{x}_1, \mathbf{x}_k + \xi_k) \right] \right]. \quad (3.40)$$

Notice as Φ_k constitutes of Φ and ξ_k , as seen from Eq. (3.31), we may change the expectation with respect to Φ_k to two expectations over Φ and ξ_k as in Eq. (3.40). Once again we use the fact that $\mathbb{E}_h[h_{k1}^2(t)] = 1$ and $\mathbb{E}_{\gamma}[\gamma_{1k1}(t)] = \frac{N_{sg}-1}{2(M-1)}$ in Eq. (3.40) this results in

$$\mathbb{E}[I_{\mathbf{x}_1s}(t)] = \frac{N_{sg} - 1}{2(M - 1)} \mathbb{E}_{\Phi} \left[\sum_{k=2}^M \mathbb{E}_{\xi_k} \left[\ell(\mathbf{x}_k + \xi_k - \mathbf{x}_1) \zeta(\mathbf{x}_1, \mathbf{x}_k + \xi_k) \right] \right] \quad (3.41)$$

$$= \frac{N_{sg} - 1}{2(M - 1)} \mathbb{E}_{\Phi} \left[\sum_{k=2}^M \frac{1}{r^{2\pi}} \int_{b(\mathbf{0}, r)} \ell(\mathbf{x}_k + \mathbf{v} - \mathbf{x}_1) \zeta(\mathbf{x}_1, \mathbf{x}_k + \mathbf{v}) d\mathbf{v} \right] \quad (3.42)$$

where Eq. (3.42) is due to the definition of expected value of $\boldsymbol{\xi}_k$ with the pdf $1/(r^2\pi)$ on $b(\mathbf{0}, r)$. If we define

$$\kappa_{\mathbf{x}_1}(\mathbf{x}_k) = \frac{1}{r^2\pi} \int_{b(\mathbf{0}, r)} \ell(\mathbf{x}_k + \mathbf{v} - \mathbf{x}_1) \zeta(\mathbf{x}_1, \mathbf{x}_k + \mathbf{v}) d\mathbf{v}, \quad (3.43)$$

then Eq. (3.42) is written as

$$\mathbb{E}[I_{\mathbf{x}_1 s}(t)] = \frac{N_{sg} - 1}{2(M - 1)} \mathbb{E}_{\Phi} \left[\sum_{k=2}^M \kappa_{\mathbf{x}_1}(\mathbf{x}_k) \right]. \quad (3.44)$$

Taking the expectation with respect to Φ yields

$$\mathbb{E}[I_{\mathbf{x}_1 s}(t)] = \frac{N_{sg} - 1}{2(M - 1)} \mathbb{E}_{\Phi} \left[\sum_{k=2}^M \kappa_{\mathbf{x}_1}(\mathbf{x}_k) \right] \quad (3.45)$$

$$= \frac{N_{sg} - 1}{2(M - 1)} \int_{\tilde{A}^M} \left(\sum_{k=2}^M \kappa_{\mathbf{u}_1}(\mathbf{u}_k) \right) f(\mathbf{u}_{[M]}) d\mathbf{u}_{[M]}. \quad (3.46)$$

A similar argument follows for the integral in Eq. (3.46) as for Eq. (3.38), so it will also be evaluated using MC integration. The mean interference at the first control unit is then given as the sum of Eq. (3.38) and Eq. (3.46). We will gather these two equations under the same integral, since it will be more computational efficient.

3.4.2 Derivation of Temporal Covariance of the Interference

The temporal covariance of the interference observed at the first control unit is given by

$$\text{cov}(I_{\mathbf{x}_1}(t_1) I_{\mathbf{x}_1}(t_2)) = \mathbb{E}[I_{\mathbf{x}_1}(t_1) I_{\mathbf{x}_1}(t_2)] - \mathbb{E}[I_{\mathbf{x}_1}(t_1)] \mathbb{E}[I_{\mathbf{x}_1}(t_2)]. \quad (3.47)$$

The term $\mathbb{E}[I_{\mathbf{x}_1}(t_1)] \mathbb{E}[I_{\mathbf{x}_1}(t_2)]$ is known from Section 3.4.1, hence we will focus on the term $\mathbb{E}[I_{\mathbf{x}_1}(t_1) I_{\mathbf{x}_1}(t_2)]$. We assume that the interference power is a wide-sense stationary (WSS) process, that is, the expected mean is constant over time and the ACF only depends on time lag (for a formal definition of WSS see [34, pp. 20-21]). Let $\tau = t_2 - t_1$ and $\Omega_{k\tau}$ be the displacement of the k -th subnetwork over the time τ . Note the displacement $\Omega_{k\tau}$ depends on the location of all the subnetworks, since the direction is changed if the subnetworks gets closer than a minimum distance d to each other. Furthermore, when a subnetwork is rotated the sensor actuator pairs are also rotated. Let $R_{k\tau}$ be a rotation matrix that denotes the rotation of the k -th subnetwork at time τ . The term $\mathbb{E}[I_{\mathbf{x}_1}(t_1) I_{\mathbf{x}_1}(t_1 + \tau)]$ can then be calculated as follows.

$$\begin{aligned}
& \mathbb{E}[I_{\mathbf{x}_1}(t_1)I_{\mathbf{x}_1}(t_1 + \tau)] \\
&= \mathbb{E}\left[\left(\sum_{k_1=2}^M h_{k_1 0}^2(t_1)\ell(\mathbf{x}_{k_1} - \mathbf{x}_1)\gamma_{1k_1 0}(t_1)\zeta(\mathbf{x}_1, \mathbf{x}_{k_1})\right.\right. \\
&\quad \left.+\sum_{k_1=2}^M h_{k_1 1}^2(t_1)\ell(\mathbf{x}_{k_1} + \boldsymbol{\xi}_{k_1} - \mathbf{x}_1)\gamma_{1k_1 1}(t_1)\zeta(\mathbf{x}_1, \mathbf{x}_{k_1} + \boldsymbol{\xi}_{k_1})\right)\left(\sum_{k_2=2}^M h_{k_2 0}^2(t_1 + \tau)\right. \\
&\quad \times \ell(\mathbf{x}_{k_2} + \Omega_{k_2 \tau} - \mathbf{x}_1 - \Omega_{1\tau})\gamma_{1k_2 0}(t_1 + \tau)\zeta(\mathbf{x}_1 + \Omega_{1\tau}, \mathbf{x}_{k_2} + \Omega_{k_2 \tau}) \\
&\quad \left.+\sum_{k_2=2}^M h_{k_2 1}^2(t_1 + \tau)\ell(\mathbf{x}_{k_2} + \Omega_{k_2 \tau} + R_{k_2 \tau}\boldsymbol{\xi}_{k_2} - \mathbf{x}_1 - \Omega_{1\tau})\gamma_{1k_2 1}(t_1 + \tau)\right. \\
&\quad \left.\times \zeta(\mathbf{x}_1 + \Omega_{1\tau}, \mathbf{x}_{k_2} + \Omega_{k_2 \tau} + R_{k_2 \tau}\boldsymbol{\xi}_{k_2})\right)\Big] \tag{3.48}
\end{aligned}$$

$$\begin{aligned}
&= \mathbb{E}[I_{\mathbf{x}_1 cu}(t_1)I_{\mathbf{x}_1 cu}(t_1 + \tau)] + \mathbb{E}[I_{\mathbf{x}_1 cu}(t_1)I_{\mathbf{x}_1 s}(t_1 + \tau)] \\
&\quad + \mathbb{E}[I_{\mathbf{x}_1 s}(t_1)I_{\mathbf{x}_1 cu}(t_1 + \tau)] + \mathbb{E}[I_{\mathbf{x}_1 s}(t_1)I_{\mathbf{x}_1 s}(t_1 + \tau)] \tag{3.49}
\end{aligned}$$

$$= \Sigma_{cucu}(\tau) + \Sigma_{cus}(\tau) + \Sigma_{scu}(\tau) + \Sigma_{ss}(\tau). \tag{3.50}$$

The four expected values in Eq. (3.50) will be treated separately in the following sections. As was done for the mean interference, the expressions for the four expected values will result in integrals for which we use MC integration to evaluate their values.

Calculation of $\Sigma_{cucu}(\tau)$

$$\begin{aligned}
\Sigma_{cucu}(\tau) &= \mathbb{E}\left[\sum_{k_1=2}^M \sum_{k_2=2}^M h_{k_1 0}^2(t_1)h_{k_2 0}^2(t_1 + \tau)\ell(\mathbf{x}_{k_1} - \mathbf{x}_1)\ell(\mathbf{x}_{k_2} + \Omega_{k_2 \tau} - \mathbf{x}_1 - \Omega_{1\tau})\right. \\
&\quad \left.\times \gamma_{1k_1 0}(t_1)\gamma_{1k_2 0}(t_1 + \tau)\zeta(\mathbf{x}_1, \mathbf{x}_{k_1})\zeta(\mathbf{x}_1 + \Omega_{1\tau}, \mathbf{x}_{k_2} + \Omega_{k_2 \tau})\right] \tag{3.51}
\end{aligned}$$

$$\begin{aligned}
&= \mathbb{E}_{\Phi}\left[\sum_{k_1=2}^M \sum_{k_2=2}^M \mathbb{E}_h[h_{k_1 0}^2(t_1)h_{k_2 0}^2(t_1 + \tau)]\ell(\mathbf{x}_{k_1} - \mathbf{x}_1)\ell(\mathbf{x}_{k_2} + \Omega_{k_2 \tau} - \mathbf{x}_1 - \Omega_{1\tau})\right. \\
&\quad \left.\times \mathbb{E}_{\gamma}[\gamma_{1k_1 0}(t_1)\gamma_{1k_2 0}(t_1 + \tau)]\zeta(\mathbf{x}_1, \mathbf{x}_{k_1})\zeta(\mathbf{x}_1 + \Omega_{1\tau}, \mathbf{x}_{k_2} + \Omega_{k_2 \tau})\right] \tag{3.52}
\end{aligned}$$

$$\begin{aligned}
&= \frac{N_{sg} - 1}{2(M - 1)} \mathbb{E}_{\Phi}\left[\sum_{k=2}^M \mathbb{E}_h[h_{k 0}^2(t_1)h_{k 0}^2(t_1 + \tau)]\ell(\mathbf{x}_k - \mathbf{x}_1)\right. \\
&\quad \left.\times \ell(\mathbf{x}_k + \Omega_{k\tau} - \mathbf{x}_1 - \Omega_{1\tau})\zeta(\mathbf{x}_1, \mathbf{x}_k)\zeta(\mathbf{x}_1 + \Omega_{1\tau}, \mathbf{x}_k + \Omega_{k\tau})\right] \\
&\quad + \frac{(N_{sg} - 1)(N_{sg} - 2)}{4(M - 1)(M - 2)} \mathbb{E}_{\Phi}\left[\sum_{k_1=2}^M \sum_{\substack{k_2=2 \\ k_2 \neq k_1}}^M \ell(\mathbf{x}_{k_1} - \mathbf{x}_1)\right. \\
&\quad \left.\times \ell(\mathbf{x}_{k_2} + \Omega_{k_2 \tau} - \mathbf{x}_1 - \Omega_{1\tau})\zeta(\mathbf{x}_1, \mathbf{x}_{k_1})\zeta(\mathbf{x}_1 + \Omega_{1\tau}, \mathbf{x}_{k_2} + \Omega_{k_2 \tau})\right]. \tag{3.53}
\end{aligned}$$

In equation (3.53) the sums have been split up into terms for which $k_1 = k_2 = k$ and $k_1 \neq k_2$. In the latter sum, we have that

$$\mathbb{E}_\gamma[\gamma_{1k_10}(t_1)\gamma_{1k_20}(t_1 + \tau)] = \frac{(N_{sg} - 1)(N_{sg} - 2)}{2(M - 1)2(M - 2)} = \frac{(N_{sg} - 1)(N_{sg} - 2)}{4(M - 1)(M - 2)} \quad (3.54)$$

$$\mathbb{E}_h[h_{k_10}^2(t_1)h_{k_20}^2(t_1 + \tau)] = \mathbb{E}_h[h_{k_10}^2(t_1)]\mathbb{E}_h[h_{k_20}^2(t_1 + \tau)] = 1 \quad (3.55)$$

where Eq. (3.55) is due to independence and Eq. (3.54) can be seen as the probability of two control units transmitting at the same time and in the same group as the first subnetwork. In the former sum, we have

$$\mathbb{E}_\gamma[\gamma_{1k0}(t_1)\gamma_{1k0}(t_1 + \tau)] = \frac{N_{sg} - 1}{2(M - 1)} \quad (3.56)$$

which is the probability of receiving interference from the control unit of subnetwork k . This requires that subnetwork k and the first subnetwork are in the same channel group and that it is doing DL. This is due to no random activity as well as we sample once in each frame, so if we receive interference from an interfere at t_1 we also receive interference from the same interfere at $t_1 + \tau$. In order to determine $\mathbb{E}_h[h_{k0}^2(t_1)h_{k0}^2(t_1 + \tau)]$, we use the fact that Jake Doppler's model was used to model our small scale fading, from Eq. (3.10) and [17], we have

$$\frac{\mathbb{E}[h_i^2(t)h_i^2(t + \tau)] - \mathbb{E}[h_i^2(t)]\mathbb{E}[h_i^2(t + \tau)]}{\sigma_{h_i^2}(t)\sigma_{h_i^2}(t + \tau)} \approx J_0^2(2\pi\nu\tau f_c/c) \quad (3.57)$$

where J_0 is first order Bessel function of zeroth kind, ν is the velocity of the subnetwork, f_c is the carrier frequency and c is the speed of light. Using that $\mathbb{E}[h_i^2(t)] = 1$ and assuming that the standard deviation is time-invariant, that is, $\sigma_{h_i^2}(t)\sigma_{h_i^2}(t + \tau) = \sigma_{h_i^2}^2$. We have that

$$\mathbb{E}_h[h_{kj}^2(t_1)h_{kj}^2(t_1 + \tau)] \approx J_0^2(2\pi\nu\tau f_c/c)\sigma_{h_i^2}^2 + 1 \quad (3.58)$$

for $j = 0, 1$. Using this and Eq. (3.27) to calculate the expected value in Eq. (3.53) yields

$$\begin{aligned} \Sigma_{cucu}(\tau) &\approx \frac{(J_0^2(2\pi\nu\tau f_c/c)\sigma_{h_i^2}^2 + 1)(N_{sg} - 1)}{2(M - 1)} \int_{\tilde{A}^M} \sum_{k=2}^M \ell(\mathbf{u}_k - \mathbf{u}_1)\ell(\mathbf{u}_k + \Omega_{k\tau} - \mathbf{u}_1 - \Omega_{1\tau}) \\ &\times \zeta(\mathbf{u}_1, \mathbf{u}_k)\zeta(\mathbf{u}_1 + \Omega_{1\tau}, \mathbf{u}_k + \Omega_{k\tau})f(\mathbf{u}_{[M]})d\mathbf{u}_{[M]} \\ &+ \frac{(N_{sg} - 1)(N_{sg} - 2)}{4(M - 1)(M - 2)} \int_{\tilde{A}^M} \sum_{k_1=2}^M \sum_{\substack{k_2=2 \\ k_2 \neq k_1}}^M \ell(\mathbf{u}_{k_1} - \mathbf{u}_1)\ell(\mathbf{u}_{k_2} + \Omega_{k_2\tau} - \mathbf{u}_1 - \Omega_{1\tau}) \\ &\times \zeta(\mathbf{u}_1, \mathbf{u}_{k_1})\zeta(\mathbf{u}_1 + \Omega_{1\tau}, \mathbf{u}_{k_2} + \Omega_{k_2\tau})f(\mathbf{u}_{[M]})d\mathbf{u}_{[M]}. \end{aligned} \quad (3.59)$$

Calculation of $\Sigma_{cus}(\tau)$ and $\Sigma_{scu}(\tau)$

$$\begin{aligned} \Sigma_{cus}(\tau) &= \mathbb{E} \left[\sum_{k_1=2}^M \sum_{k_2=2}^M h_{k_1 0}^2(t_1) h_{k_2 1}^2(t_1 + \tau) \ell(\mathbf{x}_{k_1} - \mathbf{x}_1) \right. \\ &\quad \times \ell(\mathbf{x}_{k_2} + \Omega_{k_2 \tau} + R_{k_2 \tau} \boldsymbol{\xi}_{k_2} - \mathbf{x}_1 - \Omega_{1\tau}) \gamma_{1k_1 0}(t_1) \gamma_{1k_2 1}(t_1 + \tau) \\ &\quad \left. \times \zeta(\mathbf{x}_1, \mathbf{x}_{k_1}) \zeta(\mathbf{x}_1 + \Omega_{1\tau}, \mathbf{x}_{k_2} + \Omega_{k_2 \tau} + R_{k_2 \tau} \boldsymbol{\xi}_{k_2}) \right] \end{aligned} \quad (3.60)$$

$$\begin{aligned} &= \mathbb{E}_{\Phi} \left[\sum_{k_1=2}^M \sum_{k_2=2}^M \mathbb{E}_{\boldsymbol{\xi}_{k_2}} \left[\mathbb{E}_h [h_{k_1 0}^2(t_1) h_{k_2 1}^2(t_1 + \tau)] \ell(\mathbf{x}_{k_1} - \mathbf{x}_1) \right. \right. \\ &\quad \times \ell(\mathbf{x}_{k_2} + \Omega_{k_2 \tau} + R_{k_2 \tau} \boldsymbol{\xi}_{k_2} - \mathbf{x}_1 - \Omega_{1\tau}) \mathbb{E}_{\gamma} [\gamma_{1k_1 0}(t_1) \gamma_{1k_2 1}(t_1 + \tau)] \\ &\quad \left. \left. \times \zeta(\mathbf{x}_1, \mathbf{x}_{k_1}) \zeta(\mathbf{x}_1 + \Omega_{1\tau}, \mathbf{x}_{k_2} + \Omega_{k_2 \tau} + R_{k_2 \tau} \boldsymbol{\xi}_{k_2}) \right] \right] \end{aligned} \quad (3.61)$$

$$\begin{aligned} &= \frac{(N_{sg} - 1)(N_{sg} - 2)}{4(M - 1)(M - 2)} \mathbb{E}_{\Phi} \left[\sum_{k_1=2}^M \sum_{\substack{k_2=2 \\ k_2 \neq k_1}}^M \ell(\mathbf{x}_{k_1} - \mathbf{x}_1) \zeta(\mathbf{x}_1, \mathbf{x}_{k_1}) \right. \\ &\quad \times \mathbb{E}_{\boldsymbol{\xi}_{k_2}} \left[\ell(\mathbf{x}_{k_2} + \Omega_{k_2 \tau} + R_{k_2 \tau} \boldsymbol{\xi}_{k_2} - \mathbf{x}_1 - \Omega_{1\tau}) \right. \\ &\quad \left. \left. \times \zeta(\mathbf{x}_1 + \Omega_{1\tau}, \mathbf{x}_{k_2} + \Omega_{k_2 \tau} + R_{k_2 \tau} \boldsymbol{\xi}_{k_2}) \right] \right]. \end{aligned} \quad (3.62)$$

The two sums in Eq. (3.62) have been changed to sum over the different pairs of control units and sensor from different subnetworks, since we cannot receive interference from both a control unit and a sensor from the same subnetwork. Additionally, $\mathbb{E}_h [h_{k_1 0}^2(t_1) h_{k_2 1}^2(t_1 + \tau)] = 1$ due the independence between the links and $\mathbb{E}_{\gamma} [\gamma_{1k_1 0}(t_1) \gamma_{1k_2 1}(t_1 + \tau)]$ is given by

$$\mathbb{E}_{\gamma} [\gamma_{1k_1 0}(t_1) \gamma_{1k_2 1}(t_1 + \tau)] = \frac{N_{sg} - 1}{2(M - 1)} \frac{N_{sg} - 2}{2(M - 2)} = \frac{(N_{sg} - 1)(N_{sg} - 2)}{4(M - 1)(M - 2)}. \quad (3.63)$$

Using the definition of expected value of $\boldsymbol{\xi}_{k_2}$ in Eq. (3.62) with the pdf $1/(r^2\pi)$ on $b(\mathbf{0}, r)$ yields

$$\begin{aligned} \Sigma_{cus}(\tau) &= \frac{(N_{sg}-1)(N_{sg}-2)}{4(M-1)(M-2)} \mathbb{E}_{\Phi} \left[\sum_{k_1=2}^M \sum_{\substack{k_2=2 \\ k_2 \neq k_1}}^M \ell(\mathbf{x}_{k_1} - \mathbf{x}_1) \zeta(\mathbf{x}_1, \mathbf{x}_{k_1}) \right. \\ &\quad \times \mathbb{E}_{\boldsymbol{\xi}_{k_2}} \left[\ell(\mathbf{x}_{k_2} + \Omega_{k_2\tau} + R_{k_2\tau} \boldsymbol{\xi}_{k_2} - \mathbf{x}_1 - \Omega_{1\tau}) \right. \\ &\quad \left. \left. \times \zeta(\mathbf{x}_1 + \Omega_{1\tau}, \mathbf{x}_{k_2} + \Omega_{k_2\tau} + R_{k_2\tau} \boldsymbol{\xi}_{k_2}) \right] \right] \end{aligned} \quad (3.64)$$

$$\begin{aligned} &= \frac{(N_{sg}-1)(N_{sg}-2)}{4(M-1)(M-2)} \mathbb{E}_{\Phi} \left[\sum_{k_1=2}^M \sum_{\substack{k_2=2 \\ k_2 \neq k_1}}^M \ell(\mathbf{x}_{k_1} - \mathbf{x}_1) \zeta(\mathbf{x}_1, \mathbf{x}_{k_1}) \right. \\ &\quad \times \frac{1}{r^2\pi} \int_{b(\mathbf{0}, r)} \ell(\mathbf{x}_{k_2} + \Omega_{k_2\tau} + R_{k_2\tau} \mathbf{v} - \mathbf{x}_1 - \Omega_{1\tau}) \\ &\quad \left. \times \zeta(\mathbf{x}_1 + \Omega_{1\tau}, \mathbf{x}_{k_2} + \Omega_{k_2\tau} + R_{k_2\tau} \mathbf{v}) d\mathbf{v} \right]. \end{aligned} \quad (3.65)$$

If we define

$$\begin{aligned} \alpha_{\mathbf{x}_1}(\mathbf{x}_{k_2}) &= \frac{1}{r^2\pi} \int_{b(\mathbf{0}, r)} \ell(\mathbf{x}_{k_2} + \Omega_{k_2\tau} + R_{k_2\tau} \mathbf{v} - \mathbf{x}_1 - \Omega_{1\tau}) \\ &\quad \times \zeta(\mathbf{x}_1 + \Omega_{1\tau}, \mathbf{x}_{k_2} + \Omega_{k_2\tau} + R_{k_2\tau} \mathbf{v}) d\mathbf{v}, \end{aligned} \quad (3.66)$$

then taking the expected value with respect to Φ yields

$$\begin{aligned} \Sigma_{cus}(\tau) &= \frac{(N_{sg}-1)(N_{sg}-2)}{4(M-1)(M-2)} \mathbb{E}_{\Phi} \left[\sum_{k_1=2}^M \sum_{\substack{k_2=2 \\ k_2 \neq k_1}}^M \ell(\mathbf{x}_{k_1} - \mathbf{x}_1) \zeta(\mathbf{x}_1, \mathbf{x}_{k_1}) \alpha_{\mathbf{x}_1}(\mathbf{x}_{k_2}) \right] \quad (3.67) \\ &= \frac{(N_{sg}-1)(N_{sg}-2)}{4(M-1)(M-2)} \int_{\tilde{A}^M} \sum_{k_1=2}^M \sum_{\substack{k_2=2 \\ k_2 \neq k_1}}^M \ell(\mathbf{u}_{k_1} - \mathbf{u}_1) \zeta(\mathbf{u}_1, \mathbf{u}_{k_1}) \alpha_{\mathbf{u}_1}(\mathbf{u}_{k_2}) f(\mathbf{u}_{[M]}) d\mathbf{u}_{[M]}. \end{aligned} \quad (3.68)$$

Turning to the similar case $\Sigma_{scu}(\tau)$ then by the same approach we obtain

$$\begin{aligned} \Sigma_{scu}(\tau) &= \frac{(N_{sg}-1)(N_{sg}-2)}{4(M-1)(M-2)} \int_{\tilde{A}^M} \sum_{k_2=2}^M \sum_{\substack{k_1=2 \\ k_1 \neq k_2}}^M \ell(\mathbf{u}_{k_2} + \Omega_{k_2\tau} - \mathbf{u}_1 - \Omega_{1\tau}) \\ &\quad \times \zeta(\mathbf{u}_1 + \Omega_{1\tau}, \mathbf{u}_{k_2} + \Omega_{k_2\tau}) \kappa_{\mathbf{u}_1}(\mathbf{u}_{k_1}) f(\mathbf{u}_{[M]}) d\mathbf{u}_{[M]} \end{aligned} \quad (3.69)$$

where

$$\kappa_{\mathbf{x}_1}(\mathbf{x}_k) = \frac{1}{r^2\pi} \int_{b(\mathbf{0}, r)} \ell(\mathbf{x}_k + \mathbf{v} - \mathbf{x}_1) \zeta(\mathbf{x}_1, \mathbf{x}_k + \mathbf{v}) d\mathbf{v} \quad (3.70)$$

is identical to Eq. (3.43).

Calculation of $\Sigma_{ss}(\tau)$

$$\begin{aligned} \Sigma_{ss}(\tau) &= \mathbb{E} \left[\sum_{k_1=2}^M \sum_{k_2=2}^M h_{k_1 1}^2(t_1) h_{k_2 1}^2(t_1 + \tau) \ell(\mathbf{x}_{k_1} + \boldsymbol{\xi}_{k_1} - \mathbf{x}_1) \right. \\ &\quad \times \ell(\mathbf{x}_{k_2} + \Omega_{k_2\tau} + R_{k_2\tau} \boldsymbol{\xi}_{k_2} - \mathbf{x}_1 - \Omega_{1\tau}) \zeta(\mathbf{x}_1, \mathbf{x}_{k_1} + \boldsymbol{\xi}_{k_1}) \\ &\quad \left. \times \zeta(\mathbf{x}_1 + \Omega_{1\tau}, \mathbf{x}_{k_2} + \Omega_{k_2\tau} + R_{k_2\tau} \boldsymbol{\xi}_{k_2}) \gamma_{1k_1 1}(t_1) \gamma_{1k_2 1}(t_1 + \tau) \right] \end{aligned} \quad (3.71)$$

$$\begin{aligned} &= \mathbb{E}_{\Phi} \left[\sum_{k_1=2}^M \sum_{k_2=2}^M \mathbb{E}_{\boldsymbol{\xi}_{k_1}, \boldsymbol{\xi}_{k_2}} \left[\mathbb{E}_h [h_{k_1 1}^2(t_1) h_{k_2 1}^2(t_1 + \tau)] \ell(\mathbf{x}_{k_1} + \boldsymbol{\xi}_{k_1} - \mathbf{x}_1) \right. \right. \\ &\quad \times \ell(\mathbf{x}_{k_2} + \Omega_{k_2\tau} + R_{k_2\tau} \boldsymbol{\xi}_{k_2} - \mathbf{x}_1 - \Omega_{1\tau}) \zeta(\mathbf{x}_1, \mathbf{x}_{k_1} + \boldsymbol{\xi}_{k_1}) \\ &\quad \left. \left. \times \zeta(\mathbf{x}_1 + \Omega_{1\tau}, \mathbf{x}_{k_2} + \Omega_{k_2\tau} + R_{k_2\tau} \boldsymbol{\xi}_{k_2}) \mathbb{E}_{\gamma} [\gamma_{1k_1 1}(t_1) \gamma_{1k_2 1}(t_1 + \tau)] \right] \right] \end{aligned} \quad (3.72)$$

$$\begin{aligned} &= \frac{N_{sg} - 1}{2(M - 1)} \mathbb{E}_{\Phi} \left[\sum_{k=2}^M \mathbb{E}_{\boldsymbol{\xi}_k} \left[\mathbb{E}_h [h_{k 1}^2(t_1) h_{k 1}^2(t_1 + \tau)] \ell(\mathbf{x}_{k 1} + \boldsymbol{\xi}_k - \mathbf{x}_1) \right. \right. \\ &\quad \times \ell(\mathbf{x}_k + \Omega_{k\tau} + R_{k\tau} \boldsymbol{\xi}_k - \mathbf{x}_1 - \Omega_{1\tau}) \zeta(\mathbf{x}_1, \mathbf{x}_k + \boldsymbol{\xi}_k) \zeta(\mathbf{x}_1 + \Omega_{1\tau}, \mathbf{x}_k + \Omega_{k\tau} + R_{k\tau} \boldsymbol{\xi}_k) \left. \left. \right] \right] \\ &\quad + \frac{(N_{sg} - 1)(N_{sg} - 2)}{4(M - 1)(M - 2)} \mathbb{E}_{\Phi} \left[\sum_{k_1=2}^M \sum_{\substack{k_2=2 \\ k_2 \neq k_1}}^M \mathbb{E}_{\boldsymbol{\xi}_{k_1}, \boldsymbol{\xi}_{k_2}} \left[\ell(\mathbf{x}_{k_1} + \boldsymbol{\xi}_{k_1} - \mathbf{x}_1) \right. \right. \\ &\quad \times \ell(\mathbf{x}_{k_2} + \Omega_{k_2\tau} + R_{k_2\tau} \boldsymbol{\xi}_{k_2} - \mathbf{x}_1 - \Omega_{1\tau}) \zeta(\mathbf{x}_1, \mathbf{x}_{k_1} + \boldsymbol{\xi}_{k_1}) \\ &\quad \left. \left. \times \zeta(\mathbf{x}_1 + \Omega_{1\tau}, \mathbf{x}_{k_2} + \Omega_{k_2\tau} + R_{k_2\tau} \boldsymbol{\xi}_{k_2}) \right] \right]. \end{aligned} \quad (3.73)$$

In Eq. (3.73) the sums have been arranged such that terms for which $k_1 = k_2 = k$ are grouped and terms for which $k_1 \neq k_2$ are grouped. In the first sums we are looking at the same sensors at t_1 and $t_1 + \tau$, hence $\mathbb{E}_{\gamma} [\gamma_{1k_1 1}(t_1) \gamma_{1k_1 1}(t_1 + \tau)] = \frac{N_{sg} - 1}{2(M - 1)}$. For the case $k_1 \neq k_2$ we are looking at sensors from different subnetworks, hence we have

$$\mathbb{E}_{\gamma} [\gamma_{1k_1 1}(t_1) \gamma_{1k_2 1}(t_1 + \tau)] = \frac{(N_{sg} - 1)(N_{sg} - 2)}{4(M - 1)(M - 2)}, \quad (3.74)$$

$$\mathbb{E}_h [h_{k_1 1}^2(t_1) h_{k_2 1}^2(t_1 + \tau)] = \mathbb{E}_h [h_{k_1 1}^2(t_1)] \mathbb{E}_h [h_{k_2 1}^2(t_1 + \tau)] = 1 \quad (3.75)$$

where Eq. (3.75) is due to independence and Eq. (3.74) can analogous to Eq. (3.54) be seen as the probability of two sensors from different subnetworks transmitting at the same time in the same channel group as the first control unit. Rewriting Eq. (3.73)

into an expression for which it is easier to use the definition of expected value yields.

$$\begin{aligned}
\Sigma_{ss}(\tau) &= \frac{N_{sg} - 1}{2(M - 1)} \mathbb{E}_{\Phi} \left[\sum_{k=2}^M \mathbb{E}_{\xi_k} \left[\mathbb{E}_h [h_{\mathbf{x}_1 k_1}^2(t_1) h_{\mathbf{x}_1 k_1}^2(t_1 + \tau)] \ell(\mathbf{x}_k + \xi_k - \mathbf{x}_1) \right. \right. \\
&\quad \left. \left. \times \ell(\mathbf{x}_k + \Omega_{k\tau} + R_{k\tau} \xi_k - \mathbf{x}_1 - \Omega_{1\tau}) \zeta(\mathbf{x}_1, \mathbf{x}_k + \xi_k) \zeta(\mathbf{x}_1 + \Omega_{1\tau}, \mathbf{x}_k + \Omega_{k\tau} + R_{k\tau} \xi_k) \right] \right] \\
&\quad + \frac{(N_{sg} - 1)(N_{sg} - 2)}{4(M - 1)(M - 2)} \mathbb{E}_{\Phi} \left[\sum_{k_1=2}^M \sum_{\substack{k_2=2 \\ k_2 \neq k_1}}^M \mathbb{E}_{\xi_{k_1}} \left[\ell(\mathbf{x}_{k_1} + \xi_{k_1} - \mathbf{x}_1) \right. \right. \\
&\quad \times \zeta(\mathbf{x}_1, \mathbf{x}_{k_1} + \xi_{k_1}) \left. \right] \mathbb{E}_{\xi_{k_2}} \left[\ell(\mathbf{x}_{k_2} + \Omega_{k_2\tau} + R_{k_2\tau} \xi_{k_2} - \mathbf{x}_1 - \Omega_{1\tau}) \right. \\
&\quad \left. \left. \times \zeta(\mathbf{x}_{k_2} + \Omega_{k_2\tau} + R_{k_2\tau} \xi_{k_2}, \mathbf{x}_{k_1} + \xi_{k_1}) \right] \right]. \tag{3.76}
\end{aligned}$$

Again, we use the result in Eq. (3.58), that is,

$$\mathbb{E}_h [h_{k_1}^2(t_1) h_{k_1}^2(t_1 + \tau)] \approx J_0^2(2\pi\tau\nu f_c/c) \sigma_{h_i}^2 + 1, \tag{3.77}$$

and using the definition of expected value gives the following.

$$\begin{aligned}
\Sigma_{ss}(\tau) &\approx \frac{(J_0^2(2\pi\tau\nu f_c/c) \sigma_{h_i}^2 + 1)(N_{sg} - 1)}{2(M - 1)} \mathbb{E}_{\Phi} \left[\sum_{k=2}^M \frac{1}{r^2\pi} \int_{b(\mathbf{0}, r)} \ell(\mathbf{x}_k + \mathbf{v} - \mathbf{x}_1) \zeta(\mathbf{x}_1, \mathbf{x}_k + \mathbf{v}) \right. \\
&\quad \left. \times \ell(\mathbf{x}_k + \Omega_{k\tau} + R_{k\tau} \mathbf{v} - \mathbf{x}_1 - \Omega_{1\tau}) \zeta(\mathbf{x}_1 + \Omega_{1\tau}, \mathbf{x}_k + \Omega_{k\tau} + R_{k\tau} \mathbf{v}) d\mathbf{v} \right] \\
&\quad + \frac{(N_{sg} - 1)(N_{sg} - 2)}{4(M - 1)(M - 2)} \mathbb{E}_{\Phi} \left[\sum_{k_1=2}^M \sum_{\substack{k_2=2 \\ k_2 \neq k_1}}^M \frac{1}{r^2\pi} \int_{b(\mathbf{0}, r)} \ell(\mathbf{x}_{k_1} + \mathbf{v} - \mathbf{x}_1) \zeta(\mathbf{x}_1, \mathbf{x}_{k_1} + \mathbf{v}) d\mathbf{v} \right. \\
&\quad \left. \times \frac{1}{r^2\pi} \int_{b(\mathbf{0}, r)} \ell(\mathbf{x}_{k_2} + \Omega_{k_2\tau} + R_{k_2\tau} \mathbf{v} - \mathbf{x}_1 - \Omega_{1\tau}) \zeta(\mathbf{x}_1 + \Omega_{1\tau}, \mathbf{x}_{k_2} + \Omega_{k_2\tau} + R_{k_2\tau} \mathbf{v}) d\mathbf{v} \right]. \tag{3.78}
\end{aligned}$$

If we define

$$\begin{aligned}
\eta_{\mathbf{x}_1}(\mathbf{x}_k) &= \frac{1}{r^2\pi} \int_{b(\mathbf{0}, r)} \ell(\mathbf{x}_k + \mathbf{v} - \mathbf{x}_1) \zeta(\mathbf{x}_1, \mathbf{x}_k + \mathbf{v}) \ell(\mathbf{x}_k + \Omega_{k\tau} + R_{k\tau} \mathbf{v} - \mathbf{x}_1 - \Omega_{1\tau}) \\
&\quad \times \zeta(\mathbf{x}_1 + \Omega_{1\tau}, \mathbf{x}_k + \Omega_{k\tau} + R_{k\tau} \mathbf{v}) d\mathbf{v}, \tag{3.79}
\end{aligned}$$

and use it together with Eq. (3.43) and Eq. (3.66) in Eq. (3.78) we get the following.

$$\begin{aligned}
\Sigma_{ss}(\tau) &\approx \frac{(J_0^2(2\pi\tau\nu f_c/c) \sigma_{h_i}^2 + 1)(N_{sg} - 1)}{2(M - 1)} \mathbb{E}_{\Phi} \left[\sum_{k=2}^M \eta_{\mathbf{x}_1}(\mathbf{x}_k) \right] \\
&\quad + \frac{(N_{sg} - 1)(N_{sg} - 2)}{4(M - 1)(M - 2)} \mathbb{E}_{\Phi} \left[\sum_{k_1=2}^M \sum_{\substack{k_2=2 \\ k_2 \neq k_1}}^M \kappa_{\mathbf{x}_1}(\mathbf{x}_{k_1}) \alpha_{\mathbf{x}_1}(\mathbf{x}_{k_2}) \right]. \tag{3.80}
\end{aligned}$$

Taking the expectation over Φ yields

$$\begin{aligned} \Sigma_{ss}(\tau) \approx & \frac{(J_0^2(2\pi\tau\nu f_c/c)\sigma_{h_l}^2 + 1)(N_{sg} - 1)}{2(M - 1)} \int_{\tilde{A}^M} \sum_{k=2}^M \eta_{\mathbf{u}_1}(\mathbf{u}_k) f(\mathbf{u}_{[M]}) d\mathbf{u}_{[M]} \\ & + \frac{(N_{sg} - 1)(N_{sg} - 2)}{4(M - 1)(M - 2)} \int_{\tilde{A}^M} \sum_{k_1=2}^M \sum_{\substack{k_2=2 \\ k_2 \neq k_1}}^M \kappa_{\mathbf{u}_1}(\mathbf{u}_{k_1}) \alpha_{\mathbf{u}_1}(\mathbf{u}_{k_2}) f(\mathbf{u}_{[M]}) d\mathbf{u}_{[M]}. \end{aligned} \quad (3.81)$$

We have now derived all the components needed to approximate the temporal covariance,

$$\text{cov}(I_{\mathbf{x}_1}(t_1)I_{\mathbf{x}_1}(t_1 + \tau)) = \mathbb{E}[I_{\mathbf{x}_1}(t_1)I_{\mathbf{x}_1}(t_1 + \tau)] - \mathbb{E}[I_{\mathbf{x}_1}(t_1)]\mathbb{E}[I_{\mathbf{x}_1}(t_1 + \tau)] \quad (3.82)$$

where $\mathbb{E}[I_{\mathbf{x}_1}(t_1)I_{\mathbf{x}_1}(t_1 + \tau)]$ is approximate using the four terms derived in this section, that is,

$$\mathbb{E}[I_{\mathbf{x}_1}(t_1)I_{\mathbf{x}_1}(t_1 + \tau)] \approx \Sigma_{cucu}(\tau) + \Sigma_{cus}(\tau) + \Sigma_{scu}(\tau) + \Sigma_{ss}(\tau). \quad (3.83)$$

3.4.3 Autocorrelation Function of the Interference

The temporal ACF (or Pearson's correlation coefficient) is defined as

$$\rho(I_{\mathbf{x}_1}(t_1), I_{\mathbf{x}_1}(t_2)) = \frac{\text{cov}(I_{\mathbf{x}_1}(t_1), I_{\mathbf{x}_1}(t_2))}{\sqrt{\text{var}[I_{\mathbf{x}_1}(t_1)]\text{var}[I_{\mathbf{x}_1}(t_2)]}}. \quad (3.84)$$

The covariance was found in Section 3.4.2. The variance of the interference is found by evaluating the covariance at $t_1 = t_2 = t$, that is

$$\text{cov}(I_{\mathbf{x}_1}(t), I_{\mathbf{x}_1}(t)) = \mathbb{E}[I_{\mathbf{x}_1}^2(t)] - \mathbb{E}[I_{\mathbf{x}_1}(t)]^2 = \text{var}[I_{\mathbf{x}_1}(t)]. \quad (3.85)$$

Assuming that the interference power is stationary and has a finite variance and that the temporal covariance only depends on the time lag $\tau = t_2 - t_1$, we can rewrite Eq. (3.84) to

$$\rho(I_{\mathbf{x}_1}(t_1), I_{\mathbf{x}_1}(t_1 + \tau)) = \frac{\text{cov}(I_{\mathbf{x}_1}(t_1), I_{\mathbf{x}_1}(t_1 + \tau))}{\text{var}[I_{\mathbf{x}_1}]} = \rho_{I_{\mathbf{x}_1}}(\tau) \quad (3.86)$$

which can be estimated using MC integration for various time lags τ .

4. Proposed Predictors

In this chapter, the proposed interference predictors are presented. Two predictors are considered, namely a last value predictor and an autoregressive (AR) predictor. The last value predictor is chosen since, as mentioned in Section 2.3.5, the different resource allocation method used for interference mitigation only use the current measurements to make their decisions. These decisions only impact the future measurements, thus it is like predicting the future measurements to be like the current, which is the main idea behind the last value prediction. The AR predictor is chosen because of its simplicity.

For the sake of prediction, the interference samples are divided into two parts, a measurement part and a prediction part. The measurement part will be used to estimate the parameters used in the predictor, that is the AR coefficients for the AR predictor. Afterwards, the predictor can be used to predict samples beyond the measurement part. The predicted samples can then be compared with the real interference samples in the prediction part to measure how accurate the prediction is. The length of the measurement part and the prediction part in samples will be referred to as the measurement horizon and prediction horizon, respectively.

4.1 Last Value Predictor

The last value predictor works as the name suggests, it takes the interference power at the measurement horizon and predicts that the interference power will stay at this value. The equation used to perform last value prediction is seen below

$$\widehat{\mathbf{I}}(n) = \mathbf{i}(MH) \quad \text{for } n = 1, \dots, \tau \quad (4.1)$$

where $\widehat{\mathbf{I}}(1 : \tau)$ is the predicted interference samples, τ is the prediction horizon, $\mathbf{i}(MH)$ is the interference sample at time MH and MH is the measurement horizon.

4.2 Autoregressive Processes and Predictors

In this section, AR processes will be presented as well as how the parameters for such processes can be estimated. The AR process will be used to predict the interference power simulated from the interference model. Thus, this section will be concluded with an algorithm of the prediction scheme.

4.2.1 Autoregressive Processes and Yule Walker Equations

Assuming that the interference power can be modelled using an AR model of order p , that is, the interference sample at time t is given by a linear combination of the previous p interference samples. The definition of an AR model is stated below.

Definition 4.1 (Autoregressive Model)

An AR model of order p is of the form

$$\mathbf{x}(t) = \beta_0 + \beta_1 \mathbf{x}(t-1) + \beta_2 \mathbf{x}(t-2) + \cdots + \beta_p \mathbf{x}(t-p) + \mathbf{w}(t) \quad (4.2)$$

where \mathbf{x} is WSS, $\mathbf{w}(t) \sim \mathcal{N}(0, \sigma_w^2)$ is white Gaussian noise and $\beta_0, \beta_1, \beta_2, \dots, \beta_p$ are constants where

$$\beta_0 = \mu_{\mathbf{x}}(1 - \beta_1 - \beta_2 - \cdots - \beta_p) \quad (4.3)$$

and $\mu_{\mathbf{x}}$ is the mean of \mathbf{x} .

In the case where \mathbf{x} is a zero mean time series, the AR coefficient β_0 is equal to zero. For this reason the mean interference is subtracted from the interference samples before using the AR model, for ease of notation the interference samples will still be written as \mathbf{i} throughout this section, even though the mean has been subtracted. Modelling the interference as an AR model of order p is then done by

$$\mathbf{i}(t) = \sum_{j=1}^p \beta_j \mathbf{i}(t-j) + \mathbf{w}(t). \quad (4.4)$$

The coefficients $\beta_1, \beta_2, \dots, \beta_p$ can be estimated using the Yule Walker equations, which will be derived in the following. Multiplying both sides of Eq. (4.4) with $\mathbf{i}(t-h)$, for $h \geq 1$ and taking the expected value yields

$$\mathbb{E}[\mathbf{i}(t)\mathbf{i}(t-h)] = \sum_{j=1}^p \beta_j \mathbb{E}[\mathbf{i}(t-j)\mathbf{i}(t-h)], \quad (4.5)$$

since $\mathbb{E}[\mathbf{i}(t-h)\mathbf{w}(t)] = 0$ for $h \geq 1$. It follows that $\mathbb{E}[\mathbf{i}(k)\mathbf{i}(l)] = \text{cov}(k-l)$ because \mathbf{i} is a WSS zero mean time series. Hence

$$\text{cov}(h) = \sum_{j=1}^p \beta_j \text{cov}(h-j) \quad h = 1, 2, \dots \quad (4.6)$$

and evaluation for $h = 0$ we have that

$$\text{cov}(0) = \sum_{j=1}^p \beta_j \text{cov}(j) + \sigma_w^2, \quad (4.7)$$

since $\mathbb{E}[\mathbf{i}(t)\mathbf{w}(t)] = \sigma_w^2$. Isolating for σ_w^2 we have

$$\sigma_w^2 = \text{cov}(0) - \sum_{j=1}^p \beta_j \text{cov}(j) \quad (4.8)$$

This yields the Yule Walker equations given in the following definition [34, p. 113].

Definition 4.2 (Yule Walker Equations)

The Yule Walker equations are given by

$$\text{cov}(t) = \sum_{j=1}^p \beta_j \text{cov}(t-j) \quad t = 1, 2, \dots, p \quad (4.9)$$

$$\sigma_w^2 = \text{cov}(0) - \sum_{j=1}^p \beta_j \text{cov}(j). \quad (4.10)$$

Normalizing Eq. (4.9) with $\text{cov}(0)$ gives

$$\boldsymbol{\rho}(t) = \sum_{j=1}^p \beta_j \boldsymbol{\rho}(t-j) \quad t = 1, 2, \dots, p. \quad (4.11)$$

Vectorizing Eq. (4.11) gives

$$\boldsymbol{\rho} = R\boldsymbol{\beta} \quad (4.12)$$

where $\boldsymbol{\rho} = [\boldsymbol{\rho}(1), \boldsymbol{\rho}(2), \dots, \boldsymbol{\rho}(p)]^T$, $R = \{\boldsymbol{\rho}(i-j)\}_{i,j=1}^p$ and $\boldsymbol{\beta} = [\beta_1, \beta_2, \dots, \beta_p]^T$. The AR parameters can then be solved for

$$\boldsymbol{\beta} = R^{-1}\boldsymbol{\rho}. \quad (4.13)$$

Since the ACF is not known on closed form, it will be estimated. Hence, the Yule Walker estimates are given by

$$\hat{\boldsymbol{\beta}} = \hat{R}^{-1}\hat{\boldsymbol{\rho}} \quad (4.14)$$

where $\hat{\boldsymbol{\rho}} = [\hat{\boldsymbol{\rho}}(1), \hat{\boldsymbol{\rho}}(2), \dots, \hat{\boldsymbol{\rho}}(p)]$ and $\hat{R}^{-1} = \{\hat{\boldsymbol{\rho}}(i-j)\}_{i,j=1}^p$. In our prediction, the sample ACF is used as the estimate of $\boldsymbol{\rho}$.

AR prediction is done by first estimating the AR parameters of the time series, and then calculating the next step(s) of the time series where the noise is set to zero. An algorithm describing how the interference is predicted, using AR prediction, is seen in Algorithm 1.

Algorithm 1 Predicting Interference Power Using AR(p)

Input) Prediction horizon: τ , measurement horizon: MH , interference samples: $\mathbf{i}(1 : MH)$ and order: p .

Output) The predicted interference samples: $\widehat{\mathbf{I}}(1 : \tau)$.

1) Estimate $\widehat{\boldsymbol{\beta}} \in \mathbb{R}^p$ with Yule Walker equations Eq. (4.14) using $\mathbf{i}(1 : MH) - \text{mean}(\mathbf{i}(1 : MH))$.

2) Define $\mathbf{i}_p = \mathbf{i}(MH - p + 1 : MH)$.

3) for $n \in (1, 2, \dots, \tau)$:

4) $\widehat{\mathbf{I}}(n) = \widehat{\boldsymbol{\beta}}^T \mathbf{i}_p$.

5) $\mathbf{i}_p = [\mathbf{i}_p^T(2 : p) \widehat{\mathbf{I}}(n)]^T$.

5. Numerical Evaluation

In this chapter, numerical evaluation of the analytical expressions of the mean and ACF from Section 3.4 and the predictors from Chapter 4 will be performed. We start by evaluating the analytical expressions of the mean and ACF, and then the predictors, this is done in Section 5.1 and Section 5.2, respectively.

5.1 Evaluating the Mean and ACF From the Stochastic Interference Model

In this section, we start by deriving expressions for the MC integrals of the mean and then the ACF of the interference received at a control unit in an in-robot sub-network. The derivation of the MC integrals is based on the analytical expressions from Section 3.4.1 and Section 3.4.3. After the MC integrals have been constructed, we perform some numerical experiments, where we simulate interference from the interference model in Chapter 3 and compare the mean and ACF of that to the mean and ACF obtained with MC integration. We use MC integration to evaluate the integrals instead of classical numerical integration methods, such as, the trapezoidal and Simpson's rule since it is more feasible for higher dimensions [35, pp. 1-5], [36, pp 30-33]. The dimensionality of our integrals corresponds to two times the number of control units we deploy in the in-X subnetworks, as each control unit has an x and y coordinate. For a short introduction to MC integration see Appendix B.

5.1.1 Using MC Integration To Estimate the Mean Interference Power

In order to obtain the mean interference, derived in Section 3.4.1, we have to evaluate the integrals of the form

$$\mathbb{E}[I_{\mathbf{x}_1 cu}(t)] = \frac{N_{sg} - 1}{2(M - 1)} \int_{\tilde{A}^M} \left(\sum_{k=2}^M \ell(\mathbf{u}_k - \mathbf{u}_1) \zeta(\mathbf{u}_1, \mathbf{u}_k) \right) f(\mathbf{u}_{[M]}) d(\mathbf{u}_{[M]}) \quad (5.1)$$

where ℓ is a path-loss function, ζ is the shadowing component and

$$f(\mathbf{x}_{[M]}) = \prod_{k=1}^M f(\mathbf{x}_k | \mathbf{x}_{[k-1]}) \quad (5.2)$$

is the joint probability density function (pdf) of the locations of the control units. Recall from Eq. (3.21) that for $0 < k \leq M$

$$f(\mathbf{x}_k | \mathbf{x}_{[k-1]}) = \begin{cases} \frac{1}{|\tilde{A} \setminus \bigcup_{j=1}^{k-1} b(\mathbf{x}_j, d)|}, & \text{for } \mathbf{x}_k \in \tilde{A} \setminus \bigcup_{j=1}^{k-1} b(\mathbf{x}_j, d), \\ 0, & \text{else} \end{cases} \quad (5.3)$$

is the conditional pdf of the k -th control unit.

In terms of MC integration, we draw N_{sim} samples from the joint density f . Specifically, let $\mathbf{x}_{[M]}^{(i)}$ be the i -th realization of the locations of the control units, then

$$\mathbf{x}_{[M]}^{(1)}, \mathbf{x}_{[M]}^{(2)}, \dots, \mathbf{x}_{[M]}^{(N_{sim})} \stackrel{iid}{\sim} f(\mathbf{x}_{[M]}). \quad (5.4)$$

The integral in Eq. (5.1) can then be estimated by

$$Q_{\mathbf{x}_{1cu}}[N_{sim}] = \frac{1}{N_{sim}} \frac{N_{sg} - 1}{2(M-1)} \sum_{i=1}^{N_{sim}} \frac{\left(\sum_{k=2}^M \ell(\mathbf{x}_k^{(i)} - \mathbf{x}_1^{(i)}) \zeta(\mathbf{x}_1^{(i)}, \mathbf{x}_k^{(i)}) \right) f(\mathbf{x}_{[M]}^{(i)})}{f(\mathbf{x}_{[M]}^{(i)})} \quad (5.5)$$

$$= \frac{N_{sg} - 1}{2N_{sim}(M-1)} \sum_{i=1}^{N_{sim}} \left(\sum_{k=2}^M \ell(\mathbf{x}_k^{(i)} - \mathbf{x}_1^{(i)}) \zeta(\mathbf{x}_1^{(i)}, \mathbf{x}_k^{(i)}) \right). \quad (5.6)$$

The interference contribution from the control units is estimated using Eq. (5.6). In the case for the sensors, $I_{\mathbf{x}_{1s}}$, we get almost the same expression with exception of having $\kappa_{\mathbf{x}_1^{(i)}}$ instead of ℓ and ζ in the inner sum as seen in Eq. (3.46).

$$Q_{\mathbf{x}_{1s}}[N_{sim}] = \frac{N_{sg} - 1}{2N_{sim}(M-1)} \sum_{i=1}^{N_{sim}} \left(\sum_{k=2}^M \kappa_{\mathbf{x}_1^{(i)}}(\mathbf{x}_k^{(i)}) \right) \quad (5.7)$$

$$= \frac{N_{sg} - 1}{2N_{sim}(M-1)} \sum_{i=1}^{N_{sim}} \left(\sum_{k=2}^M \frac{1}{r^2\pi} \int_{b(\mathbf{0}, r)} \ell(\mathbf{x}_k^{(i)} + \mathbf{v} - \mathbf{x}_1^{(i)}) \zeta(\mathbf{x}_1^{(i)}, \mathbf{x}_k^{(i)} + \mathbf{v}) d\mathbf{v} \right). \quad (5.8)$$

As seen in Eq. (5.8) there is another integral that needs to be solved. We also solve this integral using MC integration. That is,

$$\kappa_{\mathbf{x}_1^{(i)}}(\mathbf{x}_k^{(i)}) = \frac{1}{r^2\pi} \int_{b(\mathbf{0}, r)} \ell(\mathbf{x}_k^{(i)} + \mathbf{v} - \mathbf{x}_1^{(i)}) \zeta(\mathbf{x}_1^{(i)}, \mathbf{x}_k^{(i)} + \mathbf{v}) d\mathbf{v} \quad (5.9)$$

$$\approx \frac{1}{L_{sim}} \frac{1}{r^2\pi} \sum_{n=1}^{L_{sim}} \frac{\ell(\mathbf{x}_k^{(i)} + \mathbf{v}^{(n)} - \mathbf{x}_1^{(i)}) \zeta(\mathbf{x}_1^{(i)}, \mathbf{x}_k^{(i)} + \mathbf{v}^{(n)})}{p(\mathbf{v}^{(n)})} \quad (5.10)$$

$$= \widehat{\kappa}_{\mathbf{x}_1^{(i)}}(\mathbf{x}_k^{(i)}, L_{sim}) \quad (5.11)$$

where the samples $\mathbf{v}^{(1)}, \mathbf{v}^{(2)}, \dots, \mathbf{v}^{(L_{sim})} \stackrel{iid}{\sim} \mathcal{U}(b(\mathbf{0}, r))$, in this case $p = 1/(r^2\pi)$. Using Eq. (5.11) to estimate Eq. (5.8) yields

$$Q_{\mathbf{x}_1s}[N_{sim}] \approx \frac{N_{sg} - 1}{2N_{sim}(M - 1)} \sum_{i=1}^{N_{sim}} \left(\sum_{k=2}^M \frac{1}{L_{sim}} \sum_{n=1}^{L_{sim}} \ell(\mathbf{x}_k^{(i)} + \mathbf{v}^{(n)} - \mathbf{x}_1^{(i)}) \zeta(\mathbf{x}_1^{(i)}, \mathbf{x}_k^{(i)} + \mathbf{v}^{(n)}) \right) \quad (5.12)$$

$$= Q_{\mathbf{x}_1s}[N_{sim}, L_{sim}]. \quad (5.13)$$

It should be noted, that in the case of scenario 1 from Table 3.4 there is no misalignment, that is, all the received interference is from sensors from other subnetworks. Consequently, if the mean interference is estimated for this scenario using MC integration, Eq. (5.13) should be used after multiplying it with 2. For scenario 2 which is not only without misalignment but also with only one channel, which gives that $N_{sg} = M$ and thus resulting in the following

$$Q_{\mathbf{x}_1s}[N_{sim}, L_{sim}] = \frac{1}{N_{sim}} \sum_{i=1}^{N_{sim}} \left(\sum_{k=2}^M \frac{1}{L_{sim}} \sum_{n=1}^{L_{sim}} \ell(\mathbf{x}_k^{(i)} + \mathbf{v}^{(n)} - \mathbf{x}_1^{(i)}) \zeta(\mathbf{x}_1^{(i)}, \mathbf{x}_k^{(i)} + \mathbf{v}^{(n)}) \right). \quad (5.14)$$

From Section 3.4.1, we have that the expected interference can be estimated as the sum of Eq. (5.6) and Eq. (5.13).

$$Q_{\mathbf{x}_1}[N_{sim}, L_{sim}] = Q_{\mathbf{x}_1cu}[N_{sim}] + Q_{\mathbf{x}_1s}[N_{sim}, L_{sim}] \quad (5.15)$$

$$\begin{aligned} &= \frac{N_{sg} - 1}{2N_{sim}(M - 1)} \sum_{i=1}^{N_{sim}} \left(\sum_{k=2}^M \ell(\mathbf{x}_k^{(i)} - \mathbf{x}_1^{(i)}) \zeta(\mathbf{x}_1^{(i)}, \mathbf{x}_k^{(i)}) \right) \\ &+ \frac{N_{sg} - 1}{2N_{sim}(M - 1)} \sum_{i=1}^{N_{sim}} \left(\sum_{k=2}^M \frac{1}{L_{sim}} \sum_{n=1}^{L_{sim}} \ell(\mathbf{x}_k^{(i)} + \mathbf{v}^{(n)} - \mathbf{x}_1^{(i)}) \zeta(\mathbf{x}_1^{(i)}, \mathbf{x}_k^{(i)} + \mathbf{v}^{(n)}) \right) \end{aligned} \quad (5.16)$$

$$\begin{aligned} &= \frac{N_{sg} - 1}{2N_{sim}(M - 1)} \sum_{i=1}^{N_{sim}} \left(\sum_{k=2}^M \left(\ell(\mathbf{x}_k^{(i)} - \mathbf{x}_1^{(i)}) \zeta(\mathbf{x}_1^{(i)}, \mathbf{x}_k^{(i)}) \right. \right. \\ &\left. \left. + \frac{1}{L_{sim}} \sum_{n=1}^{L_{sim}} \ell(\mathbf{x}_k^{(i)} + \mathbf{v}^{(n)} - \mathbf{x}_1^{(i)}) \zeta(\mathbf{x}_1^{(i)}, \mathbf{x}_k^{(i)} + \mathbf{v}^{(n)}) \right) \right). \end{aligned} \quad (5.17)$$

The mean obtained from using Eq. (5.17) corresponds to the mean interference from scenario 3 with multiple channels and misalignment. The case for scenario 4 and 5 where there is only one channel, which again gives that $N_{sg} = M$ and thus resulting

in the following

$$Q_{\mathbf{x}_1}[N_{sim}, L_{sim}] = \frac{1}{N_{sim}} \sum_{i=1}^{N_{sim}} \left(\sum_{k=2}^M \ell(\mathbf{x}_k^{(i)} - \mathbf{x}_1^{(i)}) \zeta(\mathbf{x}_1^{(i)}, \mathbf{x}_k^{(i)}) \right) + \frac{1}{L_{sim}} \sum_{n=1}^{L_{sim}} \ell(\mathbf{x}_k^{(i)} + \mathbf{v}^{(n)} - \mathbf{x}_1^{(i)}) \zeta(\mathbf{x}_1^{(i)}, \mathbf{x}_k^{(i)} + \mathbf{v}^{(n)}). \quad (5.18)$$

As seen in Appendix B the accuracy of the MC integration depends on the number samples used, that is, N_{sim} and L_{sim} . Thus, we have to investigate appropriate values for N_{sim} and L_{sim} such that the results we obtain are accurate. Afterwards, the mean interference power estimated using MC integration can be compared to the mean interference power estimated by simulating from the interference model. This is done in the next section.

5.1.2 Comparing the Mean Estimated Using MC Integration to the Mean of Simulated Interference Power

In this section, the mean interference power estimated using MC integration and mean interference power from simulations using the interference model are compared. However, in order to do this, the MC integration parameters, N_{sim} and L_{sim} , have to be determined first.

Determining N_{sim} and L_{sim}

Now we will determine the MC integration parameters, N_{sim} and L_{sim} , and make sure they are large enough for the integral to have converged. In Appendix B, it is shown that the variance decreases linearly with a factor $1/N$ where N is the number of samples, which in turn means the standard deviation decreases with a factor $1/\sqrt{N}$.

In order to see the convergence of the estimators when N_{sim} and L_{sim} are increased, a variance analysis is conducted. First we look at the case in Eq. (5.13), where the mean interference comes from sensors only. In order to perform the analysis, we perform the MC integration $N_{int} = 1024$ times for each choice of N_{sim} and L_{sim} and then calculate the empirical standard deviation. Let $Q_{\mathbf{x}_1s}[N_{sim}, L_{sim}, i]$ be the i -th realization of the MC integration in Eq. (5.13). Then the estimated standard deviation is given as

$$\sigma_s[N_{sim}, L_{sim}] = \left(\frac{1}{N_{int}} \sum_{i=1}^{N_{int}} \left(Q_{\mathbf{x}_1s}[N_{sim}, L_{sim}, i] - \frac{1}{N_{int}} \sum_{j=1}^{N_{int}} Q_{\mathbf{x}_1s}[N_{sim}, L_{sim}, j] \right)^2 \right)^{1/2}. \quad (5.19)$$

In order to evaluate Eq. (5.13), we have used the parameters as specified in Table 3.3. The results of Eq. (5.19) for various N_{sim} and L_{sim} are seen in Table 5.1. We see that increasing L_{sim} does not significantly decrease the standard deviation compared to when N_{sim} is increased.

$L_{sim} \backslash N_{sim}$	10	25	50	100
10	0.00219	0.00138	0.000918	0.000683
25	0.00197	0.00126	0.000903	0.000620
50	0.00197	0.00122	0.000865	0.000615

Table 5.1: The estimated standard deviation of the mean interference from Eq. (5.13) using the settings in Table 3.3 for $N_{sim} = 10, 25, 50, 100$ and $L_{sim} = 10, 25, 50$.

$L_{sim} \backslash N_{sim}$	10	25	50	100
10	0.00155	0.000982	0.000692	0.000484
25	0.00150	0.000940	0.000666	0.000479
50	0.00149	0.000904	0.000666	0.000458

Table 5.2: The estimated standard deviation of the mean interference from Eq. (5.17) using the settings in Table 3.3 for $N_{sim} = 10, 25, 50, 100$ and $L_{sim} = 10, 25, 50$.

Secondly, we want to examine the estimated mean interference from Eq. (5.17). Specifically, let $Q_{\mathbf{x}_1}[N_{sim}, L_{sim}, i]$ be the i -th realization of the estimated mean. The estimated standard deviation $\sigma[N_{sim}, L_{sim}]$ is then defined similar to Eq. (5.19) where $Q_{\mathbf{x}_1}[N_{sim}, L_{sim}, i]$ is used instead of $Q_{\mathbf{x}_s}[N_{sim}, L_{sim}, i]$. The estimated standard deviation of the mean interference is seen in Table 5.2 for various N_{sim} and L_{sim} . Again, we observe that increasing L_{sim} does not provide any significant improvements compared to when N_{sim} is increased.

Based on these results we choose set $N_{sim} = 50$ and $L_{sim} = 10$ as the size of the 95% confidence interval will then be smaller than 2 [dB]. The confidence interval is calculated using the following expression

$$\left[\tilde{I}_{\mathbf{x}} - 1.96\sigma[50, 10], \tilde{I}_{\mathbf{x}} + 1.96\sigma[50, 10] \right] \quad (5.20)$$

where the values -1.96 and 1.96 are the 2.5% and 97.5% quantiles of the standard normal distribution, that is, $\Phi_{0.025} = -1.96$ and $\Phi_{0.975} = 1.96$, and

$$\tilde{I}_{\mathbf{x}} = \frac{1}{N_{int}} \sum_{j=1}^{N_{int}} Q_{\mathbf{x}_1}[N_{sim}, L_{sim}, j]. \quad (5.21)$$

The intervals for scenario 1, 2 and 3 are $[-21.619, -19.767]$ [dB], $[-14.629, -12.778]$ [dB] and $[-22.337, -20.680]$ [dB], respectively. For scenario 4 and 5 the interval is $[-15.347, -13.691]$ [dB].

Comparing the Mean Interference Power From the Interference Model and the Stochastic Interference Model

The mean interference estimated using MC integration is now compared to the empirical mean obtained through simulating from the model in Chapter 3. We simulated 1024 snapshots and calculated the mean interference for all of the snapshots, this is done for all the scenarios in Table 3.4. Histograms of the means for the different scenarios can be seen in Figure 5.1. In the plots we have marked the 2.5%, 25%, 50%, 75%, 97.5% quantiles. Furthermore, the edges of the confidence intervals for the means obtained using MC integration are also plotted. Here we see that, the median of the simulated means from interference model is in the middle of the confidence interval for all scenarios. Since the median is in the middle of the confidence interval for all the scenarios, we deem that the mean interference for scenario 1, 2 and 3 can be estimated well using Eq. (5.13), Eq. (5.14), and Eq. (5.17), respectively. Additionally, the mean interference for scenario 4 and 5 can be estimated well using Eq. (5.18).

5.1.3 Using MC Integration to Estimate the ACF of the Interference Power

In this section, we will derive the MC integrals for the ACF of the interference in in-robot subnetworks at different time lags using the theory from Appendix B and the analytical expressions from Section 3.4.2. Afterwards, the ACF obtained using MC integration is compared with empirically estimates of the ACF using simulated data from the interference model in Chapter 3.

In the estimation of the covariance of the interference, we need to calculate some integrals. Specifically, we need to estimate $\kappa_{\mathbf{x}_1}$, $\alpha_{\mathbf{x}_1}$ and $\eta_{\mathbf{x}_1}$, which will also be done using MC integration. The function $\kappa_{\mathbf{x}_1}$ has already been estimated in Eq. (5.11). Recall from Section 3.4.2 that $\alpha_{\mathbf{x}_1}$ and $\eta_{\mathbf{x}_1}$ are defined as

$$\begin{aligned} \alpha_{\mathbf{x}_1}(\mathbf{x}_k) &= \frac{1}{r^2\pi} \int_{b(\mathbf{0},r)} \ell(\mathbf{x}_k + \Omega_{k\tau} + R_{k\tau}\mathbf{v} - \mathbf{x}_1 - \Omega_{1\tau}) \\ &\quad \times \zeta(\mathbf{x}_1 + \Omega_{1\tau}, \mathbf{x}_k + \Omega_{k\tau} + R_{k\tau}\mathbf{v}) d\mathbf{v} \end{aligned} \quad (5.22)$$

and

$$\begin{aligned} \eta_{\mathbf{x}_1}(\mathbf{x}_k) &= \frac{1}{r^2\pi} \int_{b(\mathbf{0},r)} \ell(\mathbf{x}_k + \mathbf{v} - \mathbf{x}_1) \zeta(\mathbf{x}_1, \mathbf{x}_k + \mathbf{v}) \ell(\mathbf{x}_k + \Omega_{k\tau} + R_{k\tau}\mathbf{v} - \mathbf{x}_1 - \Omega_{1\tau}) \\ &\quad \times \zeta(\mathbf{x}_1 + \Omega_{1\tau}, \mathbf{x}_k + \Omega_{k\tau} + R_{k\tau}\mathbf{v}) d\mathbf{v} \end{aligned} \quad (5.23)$$

where $\tau = t_2 - t_1$ is the time lag, $\Omega_{k\tau}$ is the displacement of the k -th subnetwork after the lag τ , $R_{k\tau}$ is the change in direction of the k -th subnetwork after the lag τ and r is the cell radius of the subnetwork.

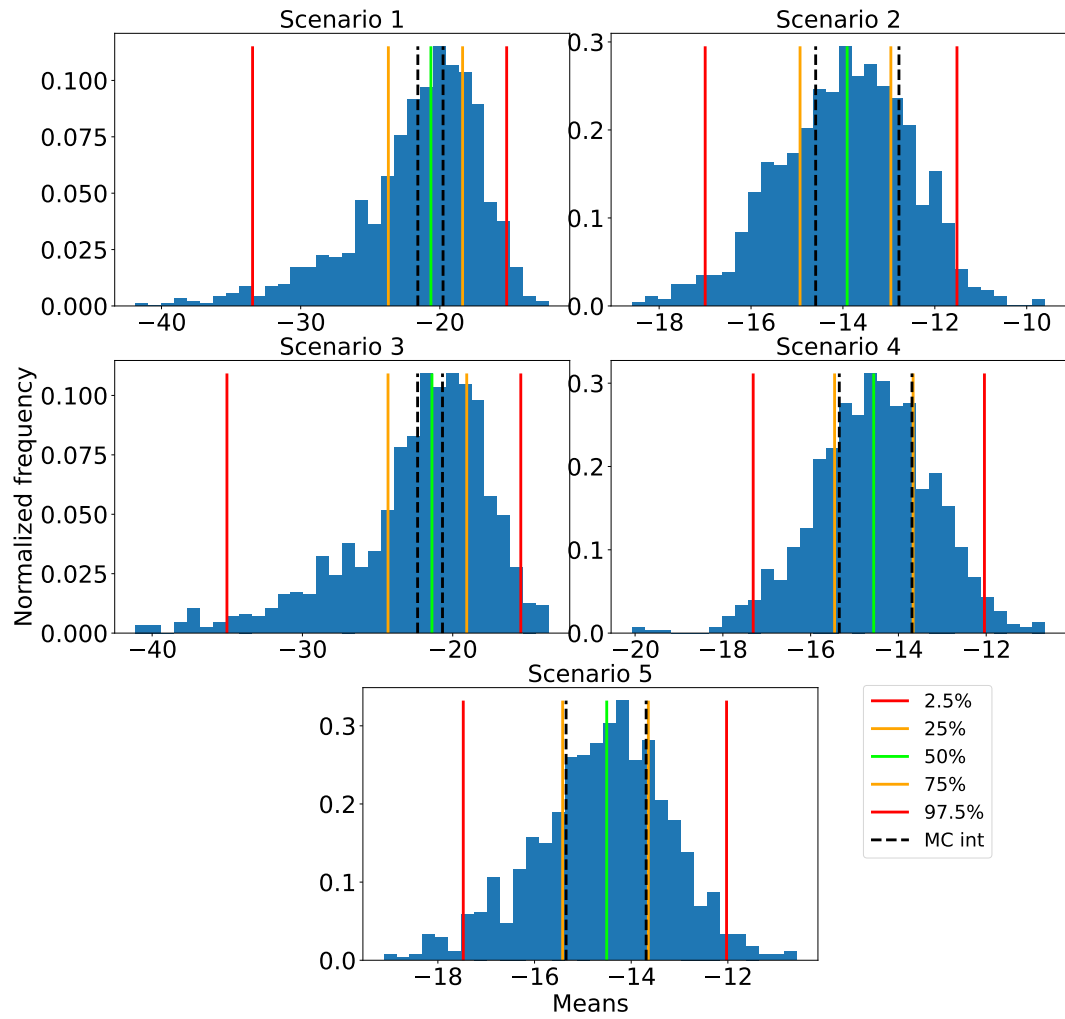


Figure 5.1: Histograms of the empirical means of the interference power simulated using the model in Chapter 3 with the settings described in Table 3.3 for the scenarios described in Table 3.4.

When performing the MC integration we deploy the subnetwork according to the joint pdf in Eq. (3.27). Afterwards, we let the subnetworks move according to the mobility model described in Chapter 3 for lag τ . Thus, after the lag τ the displacements, $\Omega_{k\tau}$, and change in direction, $R_{k\tau}$, for all the subnetworks are known.

Regarding the MC integration, we do analogously as we did with the mean interference, and use

$$\mathbf{x}_{[M]}^{(1)}, \mathbf{x}_{[M]}^{(2)}, \dots, \mathbf{x}_{[M]}^{(N_{sim})} \stackrel{iid}{\sim} f(\mathbf{x}_{[M]}) \quad \text{and} \quad \mathbf{v}^{(1)}, \mathbf{v}^{(2)}, \dots, \mathbf{v}^{(L_{sim})} \stackrel{iid}{\sim} \mathcal{U}(b(\mathbf{0}, r)) \quad (5.24)$$

as the samples for the locations of the control units and sensors to estimate the integrals. The functions $\alpha_{\mathbf{x}_1}$ and $\eta_{\mathbf{x}_1}$ can then be estimated as

$$\alpha_{\mathbf{x}_1^{(i)}}(\mathbf{x}_k^{(i)}) \approx \frac{1}{L_{sim}} \sum_{n=1}^{L_{sim}} \ell(\mathbf{x}_k^{(i)} + \Omega_{k\tau}^{(i)} + R_{k\tau}^{(i)} \mathbf{v}^{(n)} - \mathbf{x}_1^{(i)} - \Omega_{1\tau}^{(i)}) \quad (5.25)$$

$$\times \zeta(\mathbf{x}_1^{(i)} + \Omega_{1\tau}^{(i)}, \mathbf{x}_k^{(i)} + \Omega_{k\tau}^{(i)} + R_{k\tau}^{(i)} \mathbf{v}^{(n)}) \quad (5.26)$$

$$= \widehat{\alpha}_{\mathbf{x}_1^{(i)}}(\mathbf{x}_k^{(i)}, L_{sim}) \quad (5.27)$$

and

$$\eta_{\mathbf{x}_1^{(i)}}(\mathbf{x}_k^{(i)}) \approx \frac{1}{L_{sim}} \sum_{n=1}^{L_{sim}} \ell(\mathbf{x}_k^{(i)} + \mathbf{v}^{(n)} - \mathbf{x}_1^{(i)}) \zeta(\mathbf{x}_1^{(i)}, \mathbf{x}_k^{(i)} + \mathbf{v}^{(n)}) \quad (5.28)$$

$$\times \ell(\mathbf{x}_k^{(i)} + \Omega_{k\tau}^{(i)} + R_{k\tau}^{(i)} \mathbf{v}^{(n)} - \mathbf{x}_1^{(i)} - \Omega_{1\tau}^{(i)}) \quad (5.29)$$

respectively. We have chosen the same MC integration parameter, L_{sim} , for α and η as for κ , since the area of integration is the same.

We start by considering covariance of the interference power for the scenarios with misalignment, that is, scenario 3, 4 and 5. Since, the covariance of these scenarios get contributions from all four terms from Eq. (3.83), whereas the covariances of scenario 1 and 2 only get a contribution from Σ_{ss} . It should be noted that the constants in Σ_{ss} are slightly different for scenario 1 and 2, which will be shown later in this section. The four terms contributing to the covariance of scenario 3, 4 and 5 can be estimated

as

$$\begin{aligned} \Sigma_{cucu}(\tau) &\approx \frac{(J_0^2(2\pi\tau\nu f_c/c)\sigma_{h_l}^2 + 1)(N_{sg} - 1)}{2(M - 1)} \frac{1}{N_{sim}} \sum_{i=1}^{N_{sim}} \sum_{k=2}^M \ell(\mathbf{x}_k^{(i)} - \mathbf{x}_1^{(i)}) \\ &\quad \times \ell(\mathbf{x}_k^{(i)} + \Omega_{k\tau}^{(i)} - \mathbf{x}_1^{(i)} - \Omega_{1\tau}^{(i)}) \zeta(\mathbf{x}_1^{(i)}, \mathbf{x}_k^{(i)}) \zeta(\mathbf{x}_1^{(i)} + \Omega_{1\tau}^{(i)}, \mathbf{x}_k^{(i)} + \Omega_{k\tau}^{(i)}) \\ &\quad + \frac{(N_{sg} - 1)(N_{sg} - 2)}{4(M - 1)(M - 2)} \frac{1}{N_{sim}} \sum_{i=1}^{N_{sim}} \sum_{k_1=2}^M \sum_{\substack{k_2=2 \\ k_2 \neq k_1}}^M \ell(\mathbf{x}_{k_1}^{(i)} - \mathbf{x}_1^{(i)}) \\ &\quad \times \ell(\mathbf{x}_{k_2}^{(i)} + \Omega_{k_2\tau}^{(i)} - \mathbf{x}_1^{(i)} - \Omega_{1\tau}^{(i)}) \zeta(\mathbf{x}_1^{(i)}, \mathbf{x}_{k_1}^{(i)}) \zeta(\mathbf{x}_1^{(i)} + \Omega_{1\tau}^{(i)}, \mathbf{x}_{k_2}^{(i)} + \Omega_{k_2\tau}^{(i)}) \end{aligned} \quad (5.30)$$

$$= \widehat{\Sigma}_{cucu}(\tau; N_{sim}), \quad (5.31)$$

$$\begin{aligned} \Sigma_{cus}(\tau) &\approx \frac{(N_{sg} - 1)(N_{sg} - 2)}{4(M - 1)(M - 2)} \frac{1}{N_{sim}} \sum_{i=1}^{N_{sim}} \sum_{k_1=2}^M \sum_{\substack{k_2=2 \\ k_2 \neq k_1}}^M \ell(\mathbf{x}_{k_1}^{(i)} - \mathbf{x}_1^{(i)}) \\ &\quad \times \zeta(\mathbf{x}_1^{(i)}, \mathbf{x}_{k_1}^{(i)}) \widehat{\alpha}_{\mathbf{x}_1^{(i)}}(\mathbf{x}_{k_2}^{(i)}; L_{sim}) \end{aligned} \quad (5.32)$$

$$= \widehat{\Sigma}_{cus}(\tau; N_{sim}, L_{sim}), \quad (5.33)$$

$$\begin{aligned} \Sigma_{scu}(\tau) &\approx \frac{(N_{sg} - 1)(N_{sg} - 2)}{4(M - 1)(M - 2)} \frac{1}{N_{sim}} \sum_{i=1}^{N_{sim}} \sum_{k_2=2}^M \sum_{\substack{k_1=2 \\ k_1 \neq k_2}}^M \ell(\mathbf{x}_{k_2}^{(i)} + \Omega_{k_2\tau}^{(i)} - \mathbf{x}_1^{(i)} - \Omega_{1\tau}^{(i)}) \\ &\quad \times \zeta(\mathbf{x}_1^{(i)} + \Omega_{1\tau}^{(i)}, \mathbf{x}_{k_2}^{(i)} + \Omega_{k_2\tau}^{(i)}) \widehat{\kappa}_{\mathbf{x}_1^{(i)}}(\mathbf{x}_{k_1}^{(i)}; L_{sim}) \end{aligned} \quad (5.34)$$

$$= \widehat{\Sigma}_{scu}(\tau; N_{sim}, L_{sim}) \quad (5.35)$$

and

$$\begin{aligned} \Sigma_{ss}(\tau) &\approx \frac{(J_0^2(2\pi\tau\nu f_c/c)\sigma_{h_l}^2 + 1)(N_{sg} - 1)}{2(M - 1)} \frac{1}{N_{sim}} \sum_{i=1}^{N_{sim}} \sum_{k=2}^M \widehat{\eta}_{\mathbf{x}_1^{(i)}}(\mathbf{x}_k^{(i)}; L_{sim}) \\ &\quad + \frac{(N_{sg} - 1)(N_{sg} - 2)}{4(M - 1)(M - 2)} \frac{1}{N_{sim}} \sum_{i=1}^{N_{sim}} \sum_{k_1=2}^M \sum_{\substack{k_2=2 \\ k_2 \neq k_1}}^M \widehat{\kappa}_{\mathbf{x}_1^{(i)}}(\mathbf{x}_{k_1}^{(i)}; L_{sim}) \\ &\quad \times \widehat{\alpha}_{\mathbf{x}_1^{(i)}}(\mathbf{x}_{k_2}^{(i)}; L_{sim}) \end{aligned} \quad (5.36)$$

$$= \widehat{\Sigma}_{ss}(\tau; N_{sim}, L_{sim}) \quad (5.37)$$

where $\sigma_{h_i}^2$ is found through simulation of small scale fading to be ≈ 0.7 . The ACF of the interference is given as

$$\rho_{I_{\mathbf{x}_1}}(\tau) = \frac{\text{cov}(\tau)}{\text{cov}(0)} = \frac{\mathbb{E}[I_{\mathbf{x}_1}(t_1)I_{\mathbf{x}_1}(t_1 + \tau)] - \mathbb{E}[I_{\mathbf{x}_1}(t_1)]\mathbb{E}[I_{\mathbf{x}_1}(t_1 + \tau)]}{\mathbb{E}[I_{\mathbf{x}_1}^2(t_1)] - \mathbb{E}[I_{\mathbf{x}_1}(t_1)]^2}. \quad (5.38)$$

From Eq. (3.83) we have that

$$\begin{aligned} \mathbb{E}[I_{\mathbf{x}_1}(t_1)I_{\mathbf{x}_1}(t_1 + \tau)] &\approx \widehat{\Sigma}_{cucu}(\tau; N_{sim}) + \widehat{\Sigma}_{cus}(\tau; N_{sim}, L_{sim}) \\ &\quad + \widehat{\Sigma}_{scu}(\tau; N_{sim}, L_{sim}) + \widehat{\Sigma}_{ss}(\tau; N_{sim}, L_{sim}) \end{aligned} \quad (5.39)$$

$$= \widehat{\Sigma}(\tau; N_{sim}, L_{sim}). \quad (5.40)$$

Using this and Eq. (5.17), for a given time lag τ , the ACF of the interference is estimated as

$$\rho_{I_{\mathbf{x}_1}}(\tau) \approx \frac{\widehat{\Sigma}(\tau; N_{sim}, L_{sim}) - Q_{\mathbf{x}_1}[N_{sim}, L_{sim}]^2}{\widehat{\Sigma}(0; N_{sim}, L_{sim}) - Q_{\mathbf{x}_1}[N_{sim}, L_{sim}]^2}. \quad (5.41)$$

Note that when using MC integration to estimate $\widehat{\Sigma}(\tau; N_{sim}, L_{sim})$ the sum that goes up to N_{sim} can be taken out of $\widehat{\Sigma}_{cucu}(\tau; N_{sim})$, $\widehat{\Sigma}_{cus}(\tau; N_{sim}, L_{sim})$, $\widehat{\Sigma}_{scu}(\tau; N_{sim}, L_{sim})$ and $\widehat{\Sigma}_{ss}(\tau; N_{sim}, L_{sim})$ and then we have one sum which goes up to N_{sim} . This is done when calculating the correlation since it is more efficient.

When estimating the ACF of the interference power for scenario 1 and 2 Eq. (5.41) is still used, the only difference being that, as mentioned, we only get contribution from Σ_{ss} . Thus $\widehat{\Sigma} = \widehat{\Sigma}_{ss}$, however $\widehat{\Sigma}_{ss}$ is slightly changed compared to scenario 3, 4 and 5. Specifically, the first and second terms are multiplied by 2 and 4, respectively. This is because for scenario 1 and 2 only receive interference from UL, hence the probability of receiving UL interference is 1, and thus when considering the traffic function in Eq. (3.17) and Eq. (3.74) only the probability of being in the same channel group is needed. This results in

$$\begin{aligned} \widehat{\Sigma}_{ss}(\tau; N_{sim}, L_{sim}) &= \frac{(J_0^2(2\pi\tau\nu f_c/c)\sigma_{h_i}^2 + 1)(N_{sg} - 1)}{(M - 1)} \frac{1}{N_{sim}} \sum_{i=1}^{N_{sim}} \sum_{k=2}^M \widehat{\eta}_{\mathbf{x}_1^{(i)}}(\mathbf{x}_k^{(i)}; L_{sim}) \\ &\quad + \frac{(N_{sg} - 1)(N_{sg} - 2)}{(M - 1)(M - 2)} \frac{1}{N_{sim}} \sum_{i=1}^{N_{sim}} \sum_{k_1=2}^M \sum_{\substack{k_2=2 \\ k_2 \neq k_1}}^M \widehat{\kappa}_{\mathbf{x}_1^{(i)}}(\mathbf{x}_{k_1}^{(i)}; L_{sim}) \\ &\quad \times \widehat{\alpha}_{\mathbf{x}_1^{(i)}}(\mathbf{x}_{k_2}^{(i)}; L_{sim}) \end{aligned} \quad (5.42)$$

$$= \widehat{\Sigma}(\tau; N_{sim}, L_{sim}). \quad (5.43)$$

5.1.4 Comparing the ACF Estimated Using MC Integration to the ACF of Simulated Interference Power

In this section, the ACF estimated using MC integration is compared to the ACFs simulated using the interference model. In order to estimate the ACF using MC integration, we need to determine values for N_{sim} and L_{sim} . Since it is more computational heavy to estimate the ACF compared to the mean, we will pick large values instead of making a variance analysis like we did for the mean interference. We choose $N_{sim} = 1600$ and $L_{sim} = 100$.

For the empirical ACFs, we use the same ACFs as in Section 3.2, where 1024 snapshots were used for each scenario. In this section, we will consider the distribution of the ACFs by looking at the quantiles over the different snapshots. In Figure 5.2 the quantiles of the ACFs from scenario 1 through 5 are seen together with the ACFs estimated using MC integration. From Figure 5.2, we see that the ACF estimated using MC integration is greater than more than 95% of the empirical ACFs for scenario 2, 4 and 5, and for scenario 1 and 3, we see that the ACF estimated using MC integration is greater than approximately 95% of the empirical ACFs. Even though the ACFs obtained using MC integration overestimate the empirical ACFs, the shape still seem to match the empirical ones, that is, their shape is similar to the Bessel function of the first kind squared (the Bessel function of the first kind squared can be seen in Figure 3.4). Since, they have similar shape it seems like there is an offset, which could be a scaling factor we failed to account for in the derivation or a mistake in the implementation. Looking at Eq. (5.41), we suspect that it is in $\widehat{\Sigma}$ where the scaling mistake lies, as the MC means, seen in Figure 5.1, seem to be correctly estimated for all the scenarios. If we try to correct the offset with a scaling factor k , that is using

$$\rho_{I_{\mathbf{x}_1}}(\tau) \approx \frac{\widehat{\Sigma}(\tau; N_{sim}, L_{sim})k - Q_{\mathbf{x}_1}[N_{sim}, L_{sim}]^2}{\widehat{\Sigma}(0; N_{sim}, L_{sim})k - Q_{\mathbf{x}_1}[N_{sim}, L_{sim}]^2}, \quad (5.44)$$

then we obtain ACFs seen in Figure 5.3. The scaling factor is different for each scenario. We found that an appropriate scaling factor for scenario 1 ($k = 1/5$) was half as big as the factor for scenario 2 ($k = 2/5$). This was also the case for scenario 3 and 4, where $k = 1/11$ and $k = 2/11$ are used for scenario 3 and 4, respectively. Recall that the only difference between scenario 1 and 3 and scenario 2 and 4, respectively, is the number of channel groups. For scenario 5, a scaling factor $k = 1/5$ was chosen.

It should be noted that the 0.05 quantile has a drop at its first time step. This may be due to an issue with the mobility model, when two or more subnetworks collide and new directions are drawn uniformly. When the new directions are drawn, there is no guarantee that the subnetworks will not collide again in the next time step. When a subnetwork changes direction the placement of the sensors in that subnetwork are also rotated. Thus, there is an instantaneous change in position of the sensors which

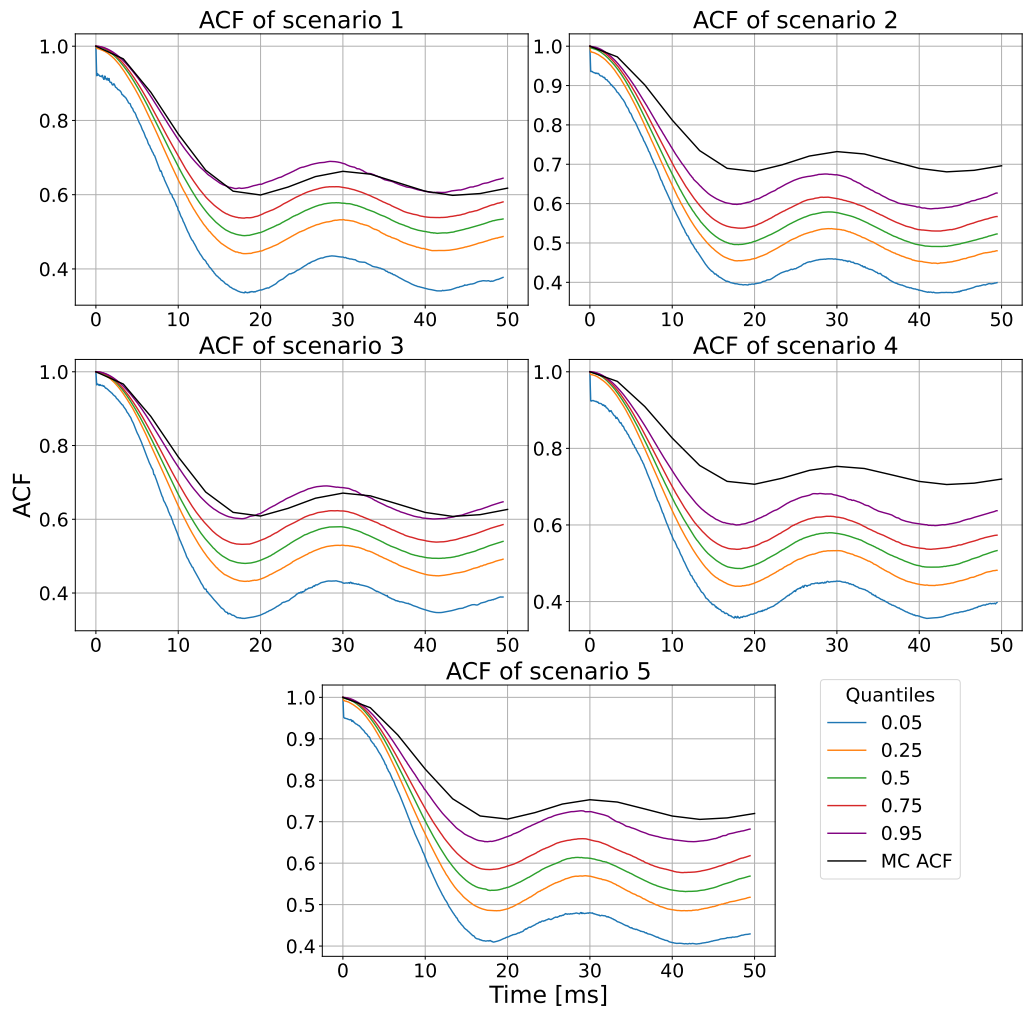


Figure 5.2: Quantiles of the ACFs for scenario 1 through 5 together with the ACF estimated using MC integration.

affects both the path-loss and the shadowing. However, despite of this flaw in the mobility model, we still maintain the same assessment, as the interference signal were simulated using a sample frequency of 10000 [Hz] and a velocity of the subnetworks 2 [m/s], so this issue only affects a small portion of the simulated interference samples.

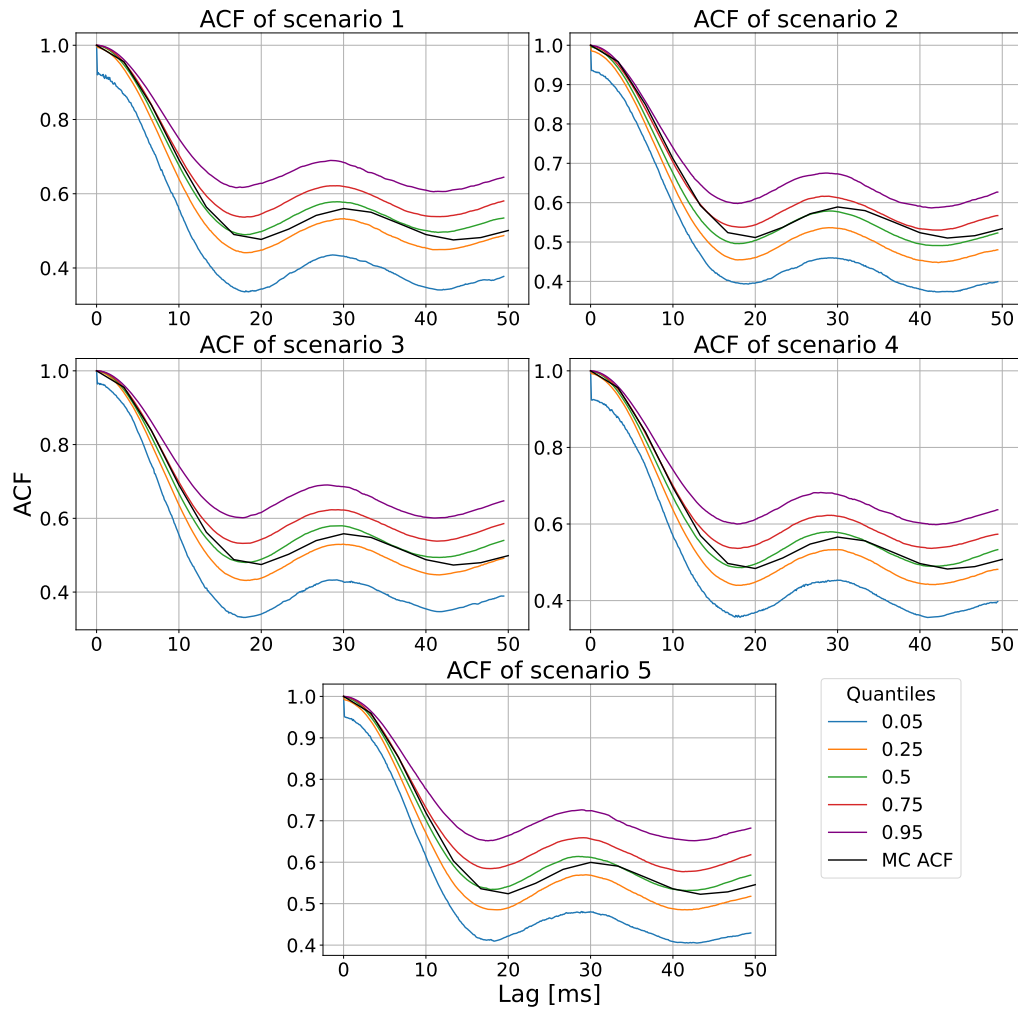


Figure 5.3: Quantiles of the ACFs for scenario 1 through 5 together with the ACF estimated using MC integration multiplied with adjusting factors.

5.2 Performance Evaluation of the Predictors

In this section, the performance of the proposed predictors is evaluated. The performance evaluation will be based on scenario 3 from Table 3.4, as this scenario includes interference received from both UL and DL as well as multiple channels. We will change some of the settings from Table 3.3, specifically, room size, number of subnetworks, and velocity, in order to see if and how changing these parameters will change the performance of the predictors. The changes made to these settings for the different test scenarios can be seen in Table 5.3. The rest of the settings are the same as the settings in Table 3.3. Before the evaluation of the predictors is conducted, a preliminary experiment is carried out. In this preliminary experiment we will determine an appropriate sample frequency for the interference predictor as well as to determine the order and training time for the AR predictor.

Settings \ Test scenario	1	2	3	4	5	6
Room size	30x30	30x30	60x60	60x60	60x60	60x60
Velocity	2	20	2	20	2	20
Number of subnetworks	16	16	16	16	32	32

Table 5.3: Settings for the different test scenarios.

5.2.1 Preliminary Experiment

First, we start out with a preliminary experiment where we test for which sample frequency it makes sense to predict the interference as well as select an appropriate model order and a measurement horizon for the AR predictor. It is important to choose an appropriate sample frequency since, if the sample frequency is too high, the change in power between each sample could be almost negligible. In order to see the change between each sample, we have made a histogram of the absolute difference between neighboring samples. This is done for test scenario 1 for different sample frequencies, 5000, 1000, 500, 250 [Hz], these histograms can be seen in Figure 5.4. We have chosen a sample frequency of 250 [Hz], since we deem that when the median of the differences between samples is 1 [dB] there is enough change between samples. For the remainder of this chapter a sample frequency of 250 [Hz] is used.

As presented in Chapter 4, we want to use an AR predictor to predict the interference power. In order to select an appropriate order as well as a measurement horizon, an initial prediction experiment is conducted. In order to evaluate the accuracy of a prediction, we use the normalized mean squared error (NMSE), since the NMSE is a commonly used metric to evaluate the accuracy of interference predictions [1], [37].

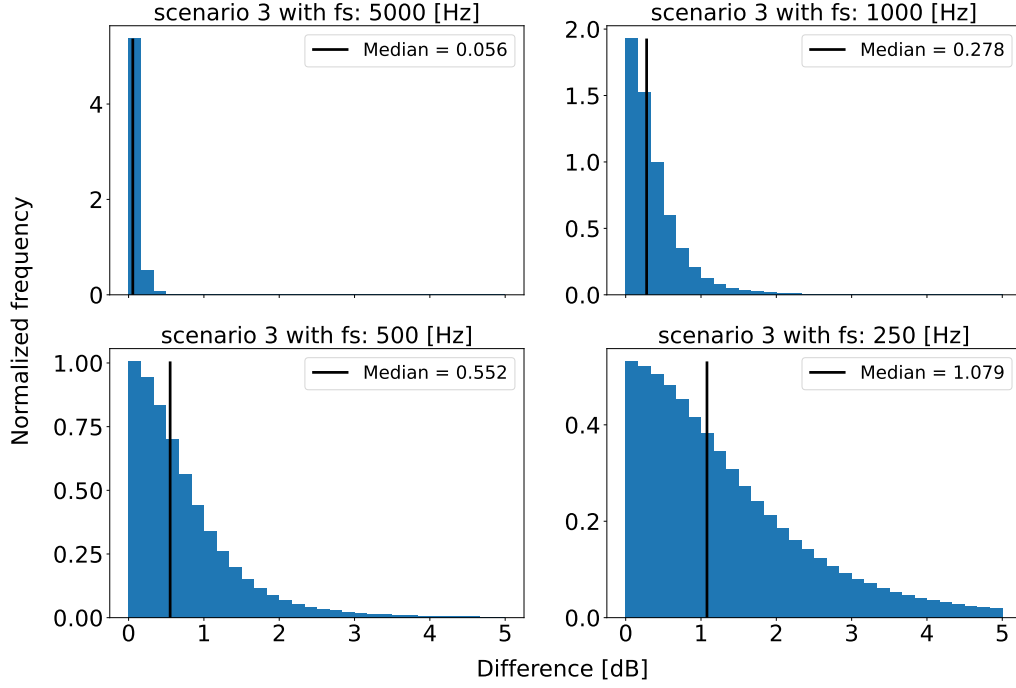


Figure 5.4: Histograms of the difference between neighboring samples for test scenario 1 with sample frequencies of 5000, 1000, 500, 250 [Hz].

The NMSE is defined as

$$\text{NMSE}(\tau) = \frac{1}{N_{obs}} \sum_{j=1}^{N_{obs}} \text{NMSE}_j(\tau) = \frac{1}{N_{obs}} \sum_{j=1}^{N_{obs}} \frac{\sum_{t=1}^{PT} (i_j(MH + t + \tau) - \hat{I}_j(t + \tau))^2}{\sum_{t=1}^{PT} (i_j(MH + t + \tau))^2} \quad (5.45)$$

where N_{obs} is the number of snapshots, $\text{NMSE}_j(\tau)$ is the NMSE of the j -th snapshot for a prediction horizon τ , PT is the prediction time within each snapshot, MH is the measurement horizon, i_j is the true interference power of the j -th snapshot and \hat{I}_j is the predicted interference values for the j -th snapshot. Throughout all of the experiments the NMSE will be calculated using $N_{obs} = 1024$ and $PT = 250$.

In the experiments, noise has been added to the snapshots to represent the measurement noise when the interference power is sampled by the predictors. Let \bar{i}_j be the mean interference of the j -th snapshot, then the noise is added in the following way

$$\tilde{i}_j(t) = i_j(t) + w_j^2(t) \quad (5.46)$$

where $\{w_j(t)\}_t \stackrel{iid}{\sim} \mathcal{N}(0, \sigma_{w,j}^2)$ and

$$\sigma_{w,j}^2 = 10^{SNR/10} \bar{i}_j. \quad (5.47)$$

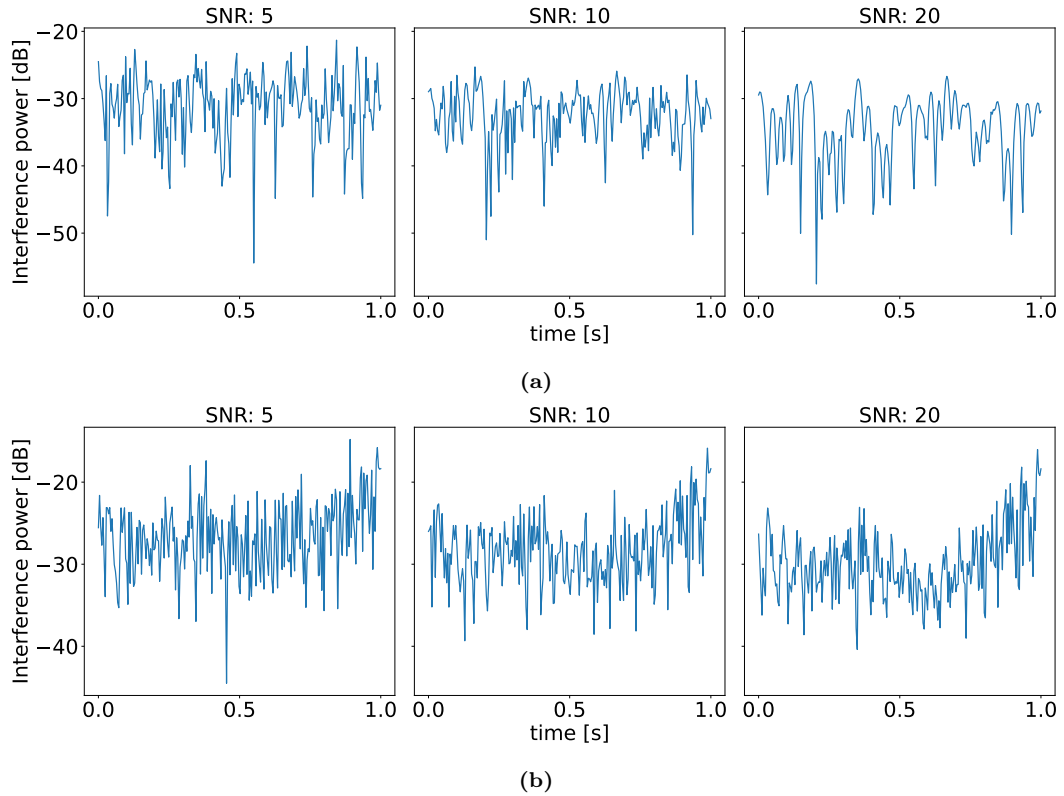


Figure 5.5: Plots of interference traces for scenario 1 in (a) and scenario 2 in (b).

The AR predictors then train on data with noise added to it, this is done for different signal to noise ratios (SNRs) specifically 5, 10 and 20 [dB]. For the initial experiment, test scenario 1 and 2 from Table 5.3 will be used. The only difference between the two scenarios is the velocity of the subnetworks, which is 2 and 20 [m/s] for scenario 1 and 2, respectively. We found that increasing the velocity of the subnetworks changed the interference power significantly compared to changing the other simulation settings. Hence, for the initial test we use the two scenarios. Time traces of the simulated interference power for the three different SNR values are seen in Figure 5.5a and Figure 5.5b for the first and fourth test scenario, respectively.

Based on the time traces of the interference, we expect a good prediction performance for the cases with SNR of 20 [dB] and slightly worse performance for SNR of 10 [dB] while we expect a bad performance for SNR of 5 [dB]. Additionally, the difference between scenario 1 and 2 is apparent, we see an increased volatility of the interference power of scenario 2, hence we expect a worse prediction accuracy for scenarios with velocity of 20 [m/s] compared to scenarios with velocity of 2 [m/s].

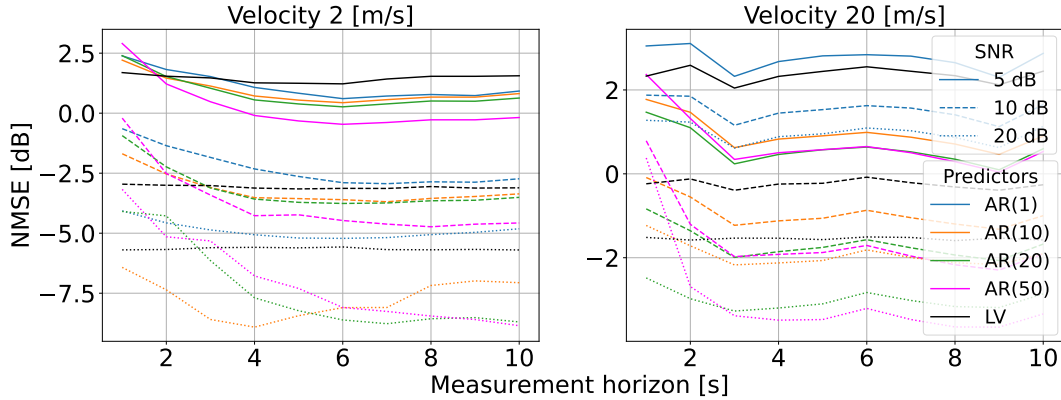


Figure 5.6: Plots of the NMSE, for a one-step prediction, against the measurement horizon for scenario 1 and 2.

In order to evaluate which AR order and measurement horizon to use, the AR predictors are tested by comparing them for one-step ahead predictions ($\tau = 1$ corresponding to 4 [ms]) for different choices of measurement horizons. The AR orders we test for are 1, 10, 20 and 50. The prediction is carried out according to Algorithm 1 seen at the end of Chapter 4. The NMSE, for a one-step prediction, is plotted against the measurement horizon in Figure 5.6 for test scenario 1 and 2.

For both velocities it is observed that a measurement horizon of 5 [s] is enough for the AR predictors to be trained, and that AR(10), AR(20) and AR(50) performs better than the last value predictor. For a velocity of 2 [m/s], it is observed that AR(50) performs best for SNRs of 5 and 10 [dB], while for an SNR of 20 [dB] it is AR(10) and AR(20) that have the best performances. For a velocity of 20 [m/s], it is seen that AR(20) and AR(50) performs similarly across all SNR values. Based on these observations, we assess that the AR(20) predictor performs the best when considering both scenarios, and that a measurement horizon of 5 [s] is sufficient, that is, $MH = 1250$. Thus, we will use the AR(20) predictor in the remainder of the performance evaluation with a measurement horizon of 5 [s].

5.2.2 Performance Evaluation of the Predictors

As mentioned we will test the AR(20) predictor for different settings, namely, room size, velocity and number of subnetworks, the different settings for these parameters can be seen in Table 5.3 for the 6 test scenarios. For the performance evaluation of the AR(20) predictor, we will consider three different aspects. First, the mean NMSE from Eq. (5.45) is plotted against the prediction horizon. Second, the CDF of the NMSE is plotted, this is done in order to see the distribution of $NMSE_j(\tau)$ instead of the mean values $NMSE(\tau)$. Lastly, the NMSE is plotted against the SNR values ranging from 0 to 25 [dB], this is to see, how robust the AR(20) predictor is to differ-

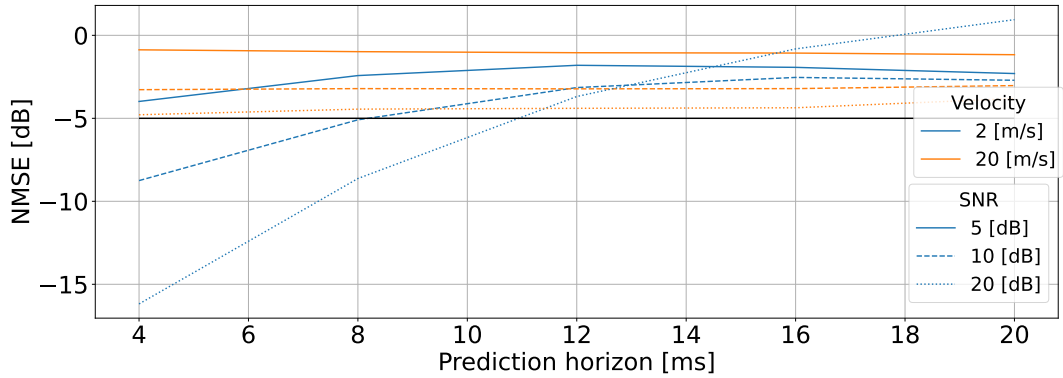


Figure 5.7: NMSE versus prediction horizon for the AR(20) predictor with measurement horizon set to 5 [s] for test scenario 1 and 2.

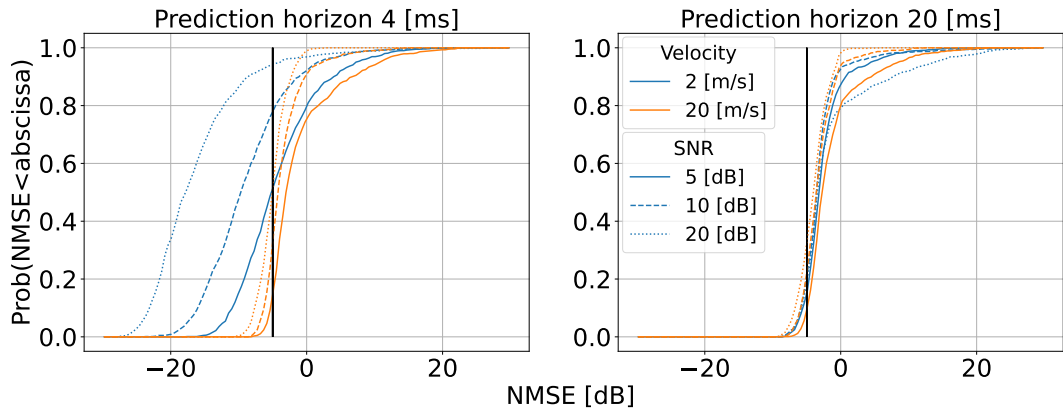


Figure 5.8: CDF of NMSE for the AR(20) predictor with prediction horizons on 4 and 20 [ms] and a measurement horizon on 5 [s] for test scenario 1 and 2.

ent levels of noise. The evaluation is made for SNR values of 5, 10 and 20 [dB] and for a one-step (4 [ms]) and a five-step (20 [ms]) prediction. An example of a time trace plot of a prediction for each scenario can be seen in Figure C.1-C.3 in Appendix C. To evaluate when a prediction is successful a threshold has to be chosen, that is, we deem predictions with an NMSE lower than that threshold successful. To the best of our knowledge, there is no generally accepted value for such a threshold. The choice of threshold depends on the application, since when a prediction is useful depends a lot on the application. In this evaluation of the predictor we set the threshold to -5 [dB]. The threshold is plotted as a black line throughout the remainder of the performance evaluation. The results for test scenario 1 and 2 are seen in Figure 5.7-5.9.

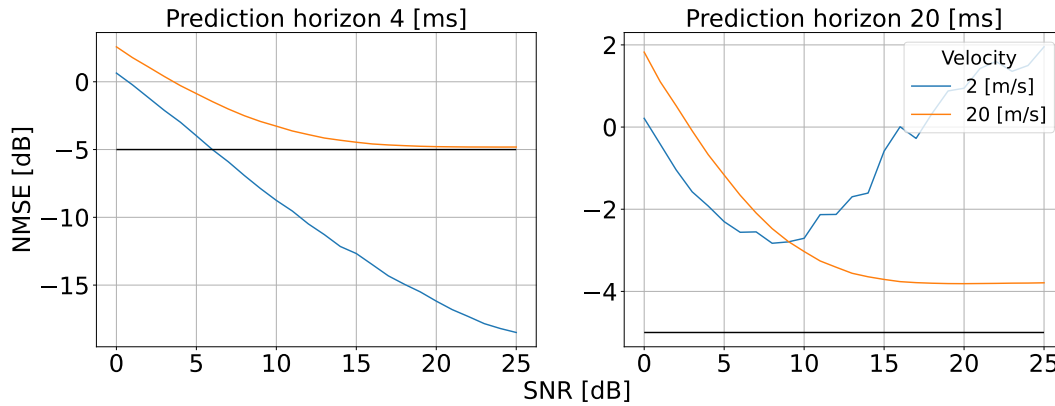


Figure 5.9: NMSE versus SNR for the AR(20) predictor with prediction horizons on 4 and 20 [ms] and a measurement horizon on 5 [s] for test scenario 1 and 2.

From Figure 5.7, it is seen that in the case of a velocity of 2 [m/s], the AR(20) predictor makes successful predictions for one step and two step predictions (4 and 8 [ms]) for an SNR of 10 and 20 [dB]. Otherwise, the prediction errors are above the -5 [dB] threshold for all prediction horizons for a velocity of 20 [m/s], and the prediction with SNR of 5 [dB] and velocity 2 [m/s]. From the CDFs in Figure 5.8 for one-step prediction, it is observed that when the velocity is 2 [m/s] the NMSEs are below the threshold for 50, 75 and 90 % of the predictions for SNRs of 5, 10 and 20 [dB], respectively. Note that for one-step predictions the distributions of the NMSEs are generally wider for a velocity of 2 [m/s], since more smaller errors occur, there are no NMSE values below -10 [dB] for velocity of 20 [m/s]. However, when looking at higher NMSE values, for instance 0 [dB], then the probability of observing errors lower than that value becomes almost the same for both of the scenarios. For the five-step prediction the probability of observing a prediction error less than the threshold is below 30 % for both scenarios for all SNR values. It is also observed that the distributions of the NMSEs, for a velocity of 20 [m/s], are almost identical for one-step prediction as for five-step prediction. This is also apparent from Figure 5.7, where the NMSEs for scenario 2 do not seem to increase much with the prediction horizon. From the NMSE plotted against different SNR values in Figure 5.9, for one step prediction it is seen that the prediction error for a velocity of 20 [m/s] stays slightly above the threshold, while for a velocity of 2 [m/s] the NMSEs are below the threshold for SNR levels greater than 7 [dB]. For the five-step prediction, it is observed that the NMSEs are above the threshold for both velocities across all SNRs. Additionally, it is seen that, for a velocity of 2 [m/s], the AR(20) predictor gets unstable for high values of SNR. This is also visible for an SNR of 20 [dB] in Figure 5.8 from the heavy tail of the NMSE distribution and in Figure 5.7 as it has the largest error at a prediction horizon of 20 [ms].

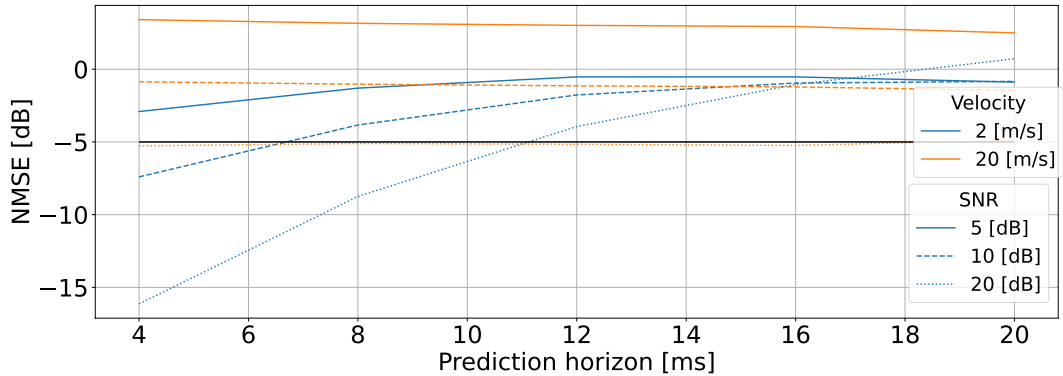


Figure 5.10: NMSE versus prediction horizon for the AR(20) predictor with measurement horizon set to 5 [s] for test scenario 3 and 4.

The results for scenario 3 and 4 are seen in Figure 5.10-5.12. From Figure 5.10, similar results as for scenario 1 and 2 are seen, that is, the prediction errors for velocity of 2 [m/s] and SNR of 10 and 20 [dB] for one and two step prediction, respectively, are below the threshold. Additionally, the NMSE for a velocity of 20 [m/s] and SNR of 20 [dB] is approximately equal to the threshold for all prediction horizons. In Figure 5.11, it is seen that for a velocity of 2 [m/s] and SNRs of 5, 10 and 20 [dB] that the one step prediction errors are below the threshold for 45, 70 and 90 % of the predictions, respectively. For a velocity of 20 [m/s] and SNR of 20 [dB], it is observed that the NMSE is below the threshold for approximately 60 % of both the one-step and five-step predictions, while rest of the five-step predictions are below the threshold less than 30 % of the time. Again, it is seen that the NMSE distributions for a velocity of 20 [m/s] are similar for one-step and five-step predictions. From Figure 5.12, similar behavior as for scenario 1 and 2 are seen for scenario 3 and 4. It should be noted that, the prediction errors are higher for scenario 3 and especially 4 for low SNR values compared to that of scenario 1 and 2, respectively.

The results for scenario 5 and 6 can be seen in Appendix C in Figure C.4-C.6. The results for these two scenarios are similar to the previous results.

5.2.3 Comparing AR(20) Predictor with Last Value Predictor

In this section, we compare the AR(20) predictor to the last value predictor. The reason for this comparison is, as mentioned in Chapter 4, the different resource allocation methods used for interference mitigation rely on current interference power measurements, and when a decision is made, it only influences future measurement, hence it is like they use last value prediction. Therefore, if the AR(20) predictor performs better than the last value predictor, it is still an improvement, even though it might not be a good prediction compared to the threshold. In this comparison, we will only look at one step prediction, which corresponds to 4 [ms], since in [7] their dynamic channel allocation algorithms measure the SINR every 5 [ms], thus one step

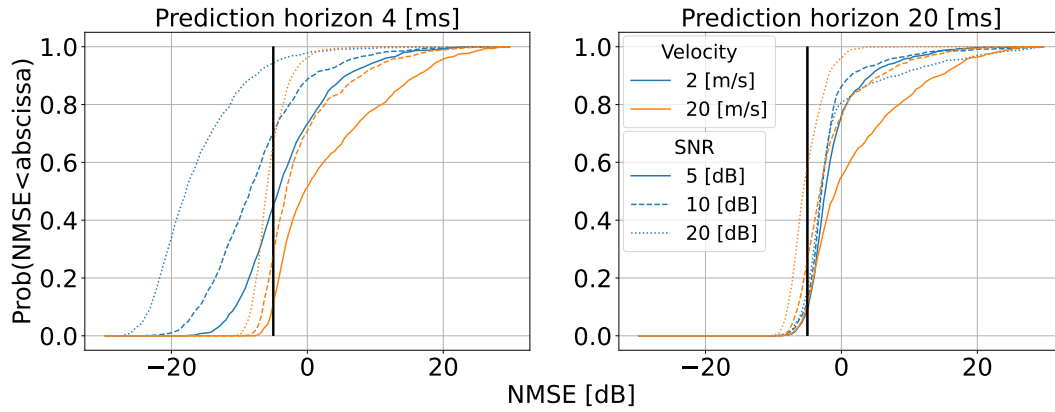


Figure 5.11: CDF of NMSE for the AR(20) predictor with prediction horizons on 4 and 20 [ms] and a measurement horizon on 5 [s] for test scenario 3 and 4.

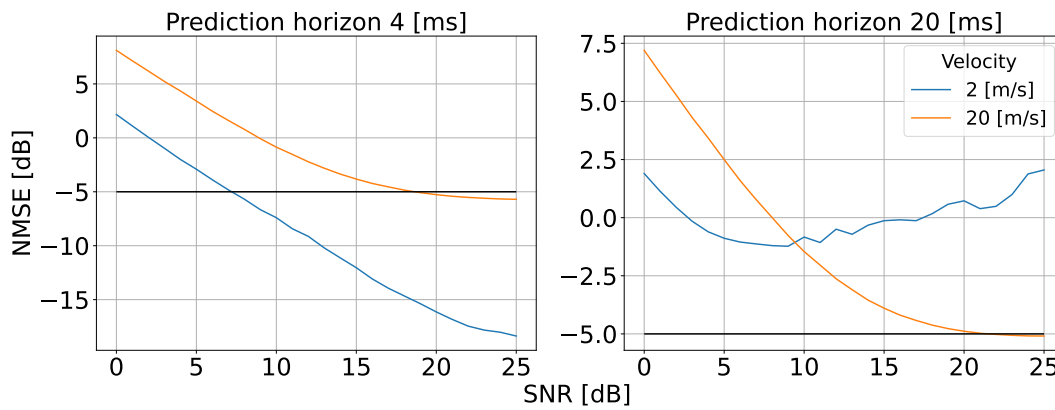


Figure 5.12: NMSE versus SNR for the AR(20) predictor with prediction horizons on 4 and 20 [ms] and a measurement horizon on 5 [s] for test scenario 3 and 4.

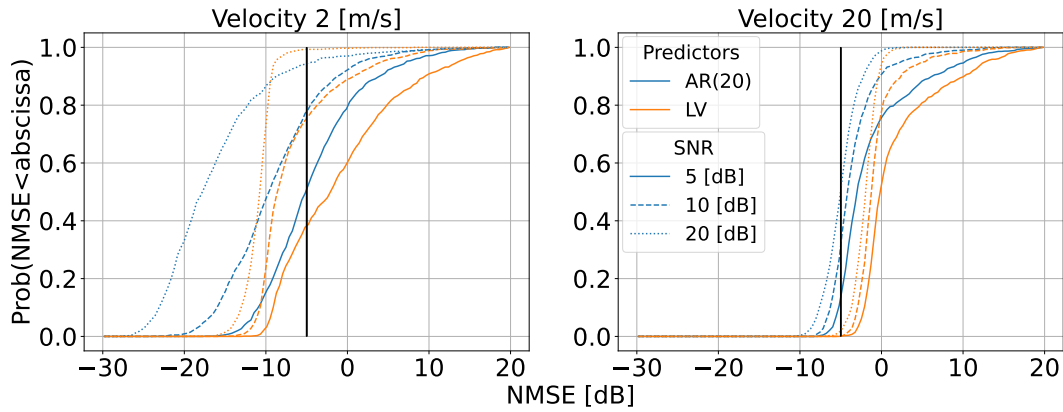


Figure 5.13: CDF of NMSE for the AR(20) and last value predictor with prediction horizons on 4 [ms] and a measurement horizon on 5 [s] for test scenario 1 and 2

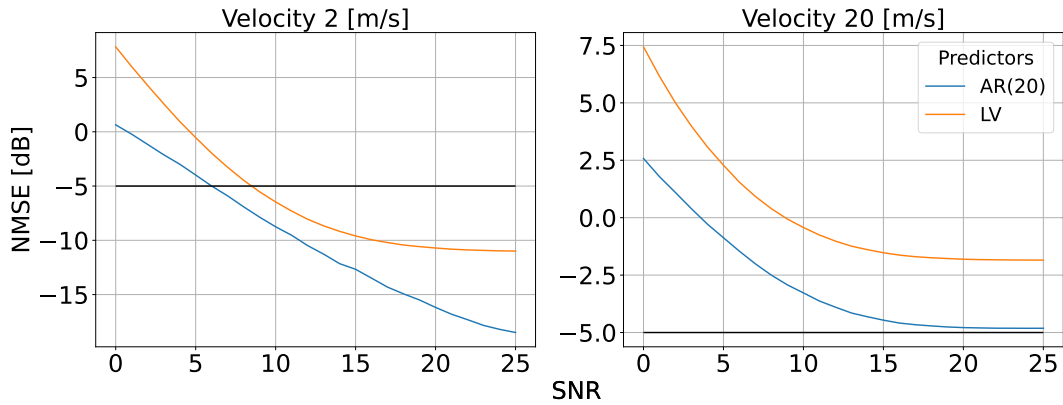


Figure 5.14: NMSE versus SNR for the AR(20) and last value predictor with prediction horizons on 4 [ms] and a measurement horizon on 5 [s] for test scenario 1 and 2.

prediction gives sufficient insight about SINR for this application. Furthermore, we also only use scenario 1 and 2, since, as we saw in the previous section, there was only a small difference in the prediction performance between scenario 1, 3 and 5 and between scenario 2, 4 and 6.

From the plots seen in Figure 5.13 and Figure 5.14, we see that the AR(20) predictor outperforms the last value predictor for all SNRs and both velocities, with the only exception being that the AR(20) predictor, for the case with a velocity of 2 [m/s] and an SNR of 20 [dB], has a higher probability of observing an NMSE greater than ≈ -9 [dB] than the last value predictor.

6. Discussion

In this chapter we elaborate on the results obtained in Chapter 5. Specifically, the estimation of the mean and ACF of the interference in Section 5.1 and the performance evaluation of the AR(20) interference predictor in Section 5.2.

For the estimation of the mean interference using MC integration, we deem that we estimated the mean interference well for all the scenarios. In the estimation of the ACFs using MC integration, we found that the estimations overestimates the empirical ACFs significantly. The reason for this overestimation is unknown, however, from Figure 5.3, the overestimation seems to be caused by a wrong scaling factor. Despite the overestimation, the shape of the estimated ACF still resembles the empirical ACF quite closely. In fact, when trying to correct for the potential scaling factor the ACFs almost coincide with the empirical ones. Both the estimated and empirical ACFs have a shape that is very close to that of the zeroth order Bessel function of the first kind squared. This Bessel function is used to approximate the ACF of the Rayleigh small scale fading, see Figure 3.4. The considered in-robot subnetworks have a velocity of 2 [m/s] which in turn means that they move 0.1 [m] over 50 [ms]. Thus, the changes in interference power is mainly due to small scale fading, as the position of the subnetworks changes slowly so path-loss and shadowing remain almost constant when considering small lags in time. In fact, when looking at the adjusted estimated ACFs, see Figure 5.3, we see a similar estimation error as the approximation error caused by using the zeroth order Bessel function of first kind instead of the ACF of the Rayleigh fading, see Figure 3.4.

From Section 5.2, a notable difference in prediction accuracy was seen for cases where the subnetworks moved with a velocity of 2 [m/s] and 20 [m/s]. Generally, the prediction error did not decrease significantly when predicting multiple steps for 20 [m/s], this is apparent in all of the plots of the CDFs and the NMSE plotted against prediction horizon (see Figure 5.7-5.8 and Figure 5.10-5.11). The subnetwork moving with a velocity of 20 [m/s], may be too fast for the AR(20) predictor to model it properly. In Figure 6.1, a histogram of the absolute difference between consecutive interference power samples is seen. Comparing this to Figure 5.4, a sample frequency of 250 [hz] may be too low to fully capture the fast variation in power we see with 20

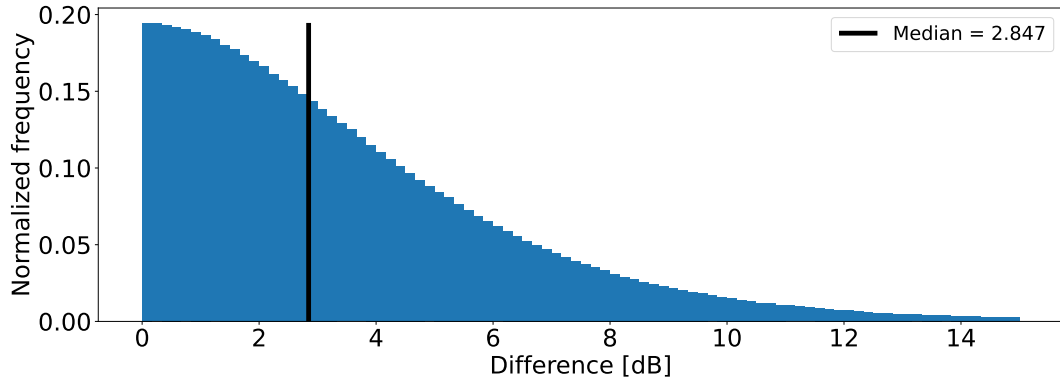


Figure 6.1: Histogram of the absolute difference between consecutive samples from test scenario 2 in Table 5.3.

[m/s]. Despite this, the AR(20) predictor still captures some of the information in the interference samples when the velocity is 20 [m/s], as can also be seen from the time trace plots in Appendix C. Further, it also outperforms the last value predictor, hence it might still be useful from an application point of view.

In the case where the subnetworks moved with a velocity of 2 [m/s], the AR(20) predictor had a prediction error below the threshold for SNR values greater than 7 [dB] for one-step predictions. However, when making five-step predictions the AR(20) predictor seem to become unstable as the SNR is increased. The reason for this, may be a model mismatch, and that the AR predictor is not well suited for predicting more than one step ahead for interference in the in-robot subnetworks model we consider. If we look at the plot in Figure 5.5 where the SNR and velocity are 20 [dB] and 2[m/s], respectively, the interference trace looks very smooth, whereas for 20 [m/s] the traces fluctuate significantly more. The increased velocity seem to aid the stability of the AR(20) predictor, as the predictor does not get unstable for high SNR values when the velocity is 20 [m/s]. This suggests that in the case of longer prediction, the AR predictor is more suited for interference with more fluctuations such as when there is low SNR or high velocity.

When comparing the results from test scenario 1 and 2 (16/900 subnetworks per [m²]) to test scenario 3 and 4 (16/3600 subnetworks per [m²]) the effects of increasing the room size becomes apparent. The prediction error for low SNR values seem to increase when the room size is increased, whereas the prediction error for high SNR values are slightly reduced (see the case with 20 [m/s]) or are close to similar. When the room size is increased, it makes the effect of path-loss more severe and the correlation due to shadowing smaller, as the distances between the subnetworks are on average larger than for test scenario 1 and 2. When comparing test scenario 3 and 4 (16/3600 subnetworks per [m²]) with test scenario 5 and 6 (32/3600 subnetworks per [m²]), the effect of increasing the number of subnetworks is seen. Increasing the number of subnetworks increases the density of the subnetworks, hence it is expected that it partly reverses the effect from increasing the room size. This is exactly what

we observe for low SNR values, here the results are between what is observed from test scenario 1 & 2 and test scenario 3 & 4. In the case of high SNR values, all the NMSEs are comparable.

In this report, we used an AR(20) model as our best interference predictor, since it is very simple to implement and use. However, ideally a more sophisticated interference predictor could be designed, which could use prior information from the in-robot subnetworks model. In Section 3.2 it was shown that the interference power from the in-robot subnetworks interference model is log-normally distributed. Additionally, in Section 5.1, the mean and ACF of the interference power have been estimated using MC integration. Thus, it could be of interest to design an interference predictor which could utilize the distribution and/or some of the first and second order statistics of the interference power samples. This could for example be achieved using a Bayesian predictor which utilizes prior information. However, even though the AR(20) predictor is over-simplistic it still provides reasonable results which could potential decrease the overhead associated with resource allocation in wireless networks. For instance, the subnetworks could use predicted interference samples to channel sensing instead of using the current measurements, and thereby avoid the interference before it occurs. It was argued that using current samples to perform the distributed dynamic resource allocation corresponds to using the interference power predicted using the last value predictor. Thus, since the AR(20) predictor outperforms the last value predictor across all scenarios, there is a potential gain which could be harvested using this simple predictor.

7. Conclusion

In this Master's Thesis, we have analyzed and predicted the interference power of in-robot subnetworks in a factory setting. In order to do so we set the goal of answering the following problem statement.

"How can a mathematical model be made to realistically capture the interference power in in-robot subnetworks in a factory setting, and how can the interference power from this model be predicted? Additionally, is it possible to find statistics for the interference power from such a model?"

In order to derive the statistics of the interference power for in-robot subnetworks in a factory setting, we first made a model describing all the different parts of the interference power. From this model first and second order statistics were derived, specifically, the mean and the ACF of the interference power. The expressions for the mean and ACF contained some high dimensional integrals which we could not solve analytically, thus we used the numerical method MC integration. We found that when we solved the expression for the mean interference, using MC integration, it coincided with the empirical mean when the interference power was simulated for all scenarios. When we solved the expression for the ACF of the interference power, we found that it overestimated the empirical ACF of the simulated interference power by a big margin, however, they did have the same form. Furthermore, we saw that if we scaled $\hat{\Sigma}$ appropriately in the calculations of the ACF, then it matched the ACF of the simulated interference power.

It was shown that a simple AR(20) predictor was able to predict the interference samples up to a time-lag of 8 [ms], when the interference power was simulated from the in-robot subnetworks model, and the velocity of the subnetworks was 2 [m/s]. The predictor was tested under different scenarios, specifically, the predictor was tested for scenarios with different room sizes, velocities and number of subnetworks. Further, the AR(20) predictor outperformed a last value predictor for all the different scenarios.

8. Future Research

Considering that a main use of interference prediction is to increase the SINR by allocating the resources according to some algorithm. It could be interesting to combine the predictor with such an algorithm, for instance, if channel switching was included in the interference model. Since it would most likely change the statistics of the different channels. Furthermore, it could be interesting to implement the DDCA algorithms from [7] and use the information from the AR predictor to see how and if it improves the results.

In future research, it could be interesting to use/design a Bayesian predictor that could use some of the prior information, that is, the interference power is log-normal distributed, how the mean and the ACF of the interference power is given. A Bayesian predictor which uses this information well.

A. Point Process Theory

In this chapter, we give a brief introduction to the point process theory, which will be used in Chapter 3. Before we can define a point process, point patterns are needed. A point pattern is defined as the deterministic sequence $\varphi = (x_k)_{k \leq \mathcal{K}} \in \mathcal{N}$ where $x_k \in \mathcal{X}$, \mathcal{N} is the space containing all point patterns φ and $\mathcal{K}, k \in \mathbb{N}^+$ [11, p. 18]. Here it is assumed that \mathcal{X} is a space equipped with a metric d , such that, (\mathcal{X}, d) is a complete, separable metric space [38, pp. 4-5]. Usually the ordering of the points in φ does not matter. The point pattern φ is called simple if $\mathbf{x}_i \neq \mathbf{x}_k$ for $i \neq k$, and then φ is a countable subset of \mathcal{X} . Associated with every point pattern φ is a counting process N_φ . The counting measure does as the name suggests count the number of points from a point pattern which fall in the space B . More mathematical definition of the counting measure is given below [11, p. 18].

Definition A.1 (Counting Measure)

The counting measure $N_\varphi : \mathcal{B} \rightarrow \mathbb{N}$ of φ is defined as

$$N_\varphi(B) = \sum_{k=1}^{\mathcal{K}} \mathbf{1}(\mathbf{x}_k \in B), \quad (\text{A.1})$$

for any bounded Borel set $B \in \mathcal{B}$, where \mathcal{B} is the Borel σ -algebra and $\mathbf{1}(\mathbf{x}_k \in B)$ is the indicator function equalling 1 if $\mathbf{x}_k \in B$ and zero otherwise. [11, p. 18]

We can now define a point process. A point process is the random process that has \mathcal{N} as the outcome space.

Definition A.2 (Point process)

A point process Φ is a measurable map from $\Sigma \rightarrow \mathcal{N}$, where $(\Sigma, \mathcal{F}, \mathbb{P})$ is a probability space [11, p. 18].

Point processes can be equivalently defined as a random counting measure N_Φ and as a random point pattern if the point process is simple. When using the random counting measure, measurability is needed, therefore $N_\Phi(B)$ needs to be defined

for a sufficiently rich class of subsets of \mathcal{X} , where the Borel σ -algebra, $\mathcal{B}(\mathcal{X})$, is the natural choice. When using the random point pattern we need the realizations of Φ to be simple with probability 1 [11, p. 19].

Next we will define the distribution of a point process, but in order to do so the subsets of \mathcal{N} which needs to be measurable has to be specified. The σ -algebra induced by $E_{B,k}$, $B \in \mathcal{B}$, $k \in \mathbb{N}_0$ where

$$E_{B,k} = \{N_\Phi(B) = k\} = \{\varphi \in \mathcal{N} : N_\varphi(B) = k\} \quad (\text{A.2})$$

is sufficiently rich for all the events of interest to be measurable. We denote this σ -algebra \mathcal{R} [11, p. 20].

An important quantity when describing point processes is the intensity measure Λ . The intensity measure is defined below [11, p. 19].

Definition A.3 (Intensity measure)

The intensity measure is defined as

$$\Lambda(B) = \mathbb{E}[N_\Phi(B)] \quad \forall B \in \mathcal{B}. \quad (\text{A.3})$$

A point process with locally finite intensity measure is a point process that satisfies $\Lambda(B) < \infty$ for $|B| < \infty$, where $|\cdot|$ is the Lebesgue measure.

Now we define the measurable space $(\mathcal{N}, \mathcal{R})$. This measurable space can be extended to a probability space by adding the point process distribution P to it. This results in the probability space $(\mathcal{N}, \mathcal{R}, P)$ which is called the canonical probability space for point processes [11, p. 20].

Definition A.4 (Point Process Distribution)

The point process distribution is the probability measure, P , pertaining to the probability space $(\mathcal{N}, \mathcal{R}, P)$

$$P(E) = \mathbb{P}(\Phi^{-1}(E)) = \mathbb{P}(\Phi \in E) \quad (\text{A.4})$$

where $\Phi^{-1}(E)$ is the pre-image of E , given by

$$\Phi^{-1}(E) = \{\omega \in \Sigma : \Phi^\omega \in E\}. \quad (\text{A.5})$$

Next we will present the class of point processes called stationary point processes. Stationary point processes have the property of being translation invariant [11, p. 21].

Definition A.5 (Stationary Point Processes)

A point process is stationary if its distribution is translation invariant i.e.

$$P(E) = P(E + \mathbf{x}) \quad \forall E \in \mathcal{R} \text{ and } \forall \mathbf{x} \in \mathcal{X} \quad (\text{A.6})$$

where $E + \mathbf{x}$ is the translation of the event E by \mathbf{x} .

Stationary point processes have almost surely an infinite number of points all throughout \mathcal{X} . Furthermore, the intensity measure of stationary point processes is proportional to the Lebesgue measure $\Lambda(B) = |B|\rho$, the constant ρ is called the intensity of the stationary point process [11, p. 21].

A.1 Binomial Point Process

In this section we will define the BPP. A BPP is a point process which is conditioned on the number of points, and each of these points are placed iid according to some known distribution f . A formal definition of a BPP is given below.

Definition A.6 (Binomial Point Process)

Let f be a density on a set $B \subset \mathcal{X}$ and let $n \in \mathbb{N}^+$. Then a point process, Φ , with n iid points with density f is called a Binomial process. We then write $\Phi \sim \text{Binomial}(B, n, f)$. [39, p. 14]

The simplest BPP is where the distribution, f , of the points is uniform over area B . An example of such an BPP is given in Figure A.1, where 100 points are distributed uniformly over the area $B = [0, 5] \times [0, 10]$.

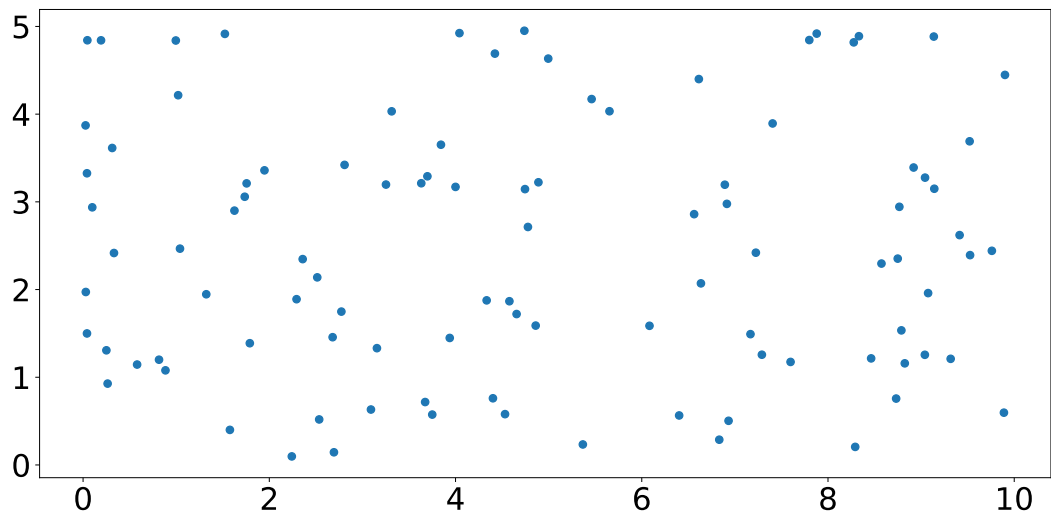


Figure A.1: An BPP $\Phi \sim \text{Binomial}([0, 5] \times [0, 10], 100, \frac{1}{50})$.

B. Monte Carlo Integration

In order to compute the mean interference as well as the ACF of the interference power in Chapter 5, we need to evaluate some integrals which we could not find any closed form solutions to. Hence, we will use MC integration instead to estimate the mean and ACF of the interference power.

If we want to evaluate an integral of the form

$$I = \int_{\Omega} f(\mathbf{x}) d\mathbf{x} \quad (\text{B.1})$$

where Ω is the domain of integration and $f : \Omega \rightarrow \mathbb{R}$. Using MC integration, the integral in Eq. (B.1) may be estimated by [36, p. 37]

$$Q[N] = \frac{1}{N} \sum_{i=1}^N \frac{f(\mathbf{x}_i)}{p(\mathbf{x}_i)} \quad (\text{B.2})$$

where \mathbf{x}_i for $i = [N]$ are drawn iid from a chosen density $p : \Omega \rightarrow \mathbb{R}_+$. This estimator is unbiased as can be seen by [36, p. 38]

$$\mathbb{E}[Q[N]] = \frac{1}{N} \sum_{i=1}^N \mathbb{E} \left[\frac{f(\mathbf{x}_i)}{p(\mathbf{x}_i)} \right] \quad (\text{B.3})$$

$$= \frac{1}{N} \sum_{i=1}^N \int_{\Omega} \frac{f(\mathbf{x})}{p(\mathbf{x})} p(\mathbf{x}) d\mathbf{x} \quad (\text{B.4})$$

$$= \int_{\Omega} f(\mathbf{x}) d\mathbf{x} \quad (\text{B.5})$$

$$= I \quad (\text{B.6})$$

given that $f(\mathbf{x})/p(\mathbf{x})$ is finite when $f(\mathbf{x}) \neq 0$. The variance of $Q[N]$ is often useful in order to assess how much the estimator has converged. The variance of $Q[N]$ is

found by [36, p. 39]

$$\text{Var}[Q[N]] = \text{Var} \left[\frac{1}{N} \sum_{i=1}^N \frac{f(\mathbf{x}_i)}{p(\mathbf{x}_i)} \right] \quad (\text{B.7})$$

$$= \frac{1}{N^2} \sum_{i=1}^N \text{Var} \left[\frac{f(\mathbf{x}_i)}{p(\mathbf{x}_i)} \right] \quad (\text{B.8})$$

$$= \frac{1}{N} \text{Var} \left[\frac{f(\mathbf{x})}{p(\mathbf{x})} \right] \quad (\text{B.9})$$

where Eq. (B.8) holds due to the independence between \mathbf{x}_i and \mathbf{x}_j for $i \neq j$. Thus, the variance of $Q[N]$ decreases linearly with a factor $1/N$. Since the estimator is unbiased and the variance decreases with the number of samples, we are guaranteed that the result is close to the true value, if we choose a sufficiently large N .

C. Additional Results

In this chapter additional results from Section 5.2 are presented. Specifically a time trace plot of a prediction for each of the test scenarios and the plots for the performance evaluation of the AR(20) for test scenario 5 and 6. The plots for the time traces and the performance evaluation can be seen in Figure C.1-C.3 and Figure C.4-C.6, respectively. In the time trace plots we have predicted for 5 time steps, which corresponds to 20 [ms], the true interference power is also shown together with the predicted interference powers.

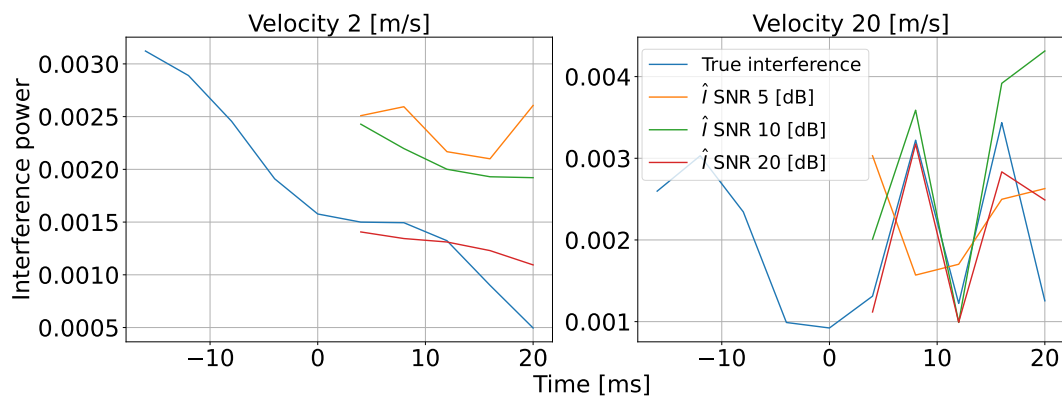


Figure C.1: Time trace plot a prediction for scenario 1 and 2.

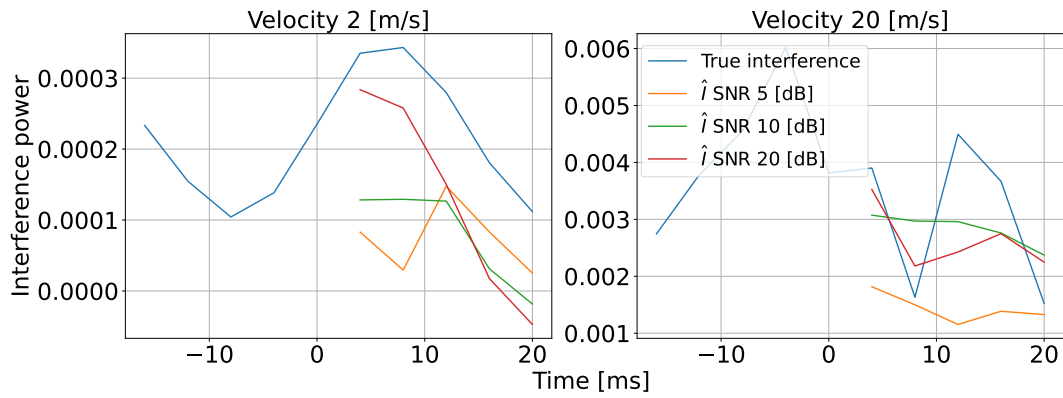


Figure C.2: Time trace plot a prediction for scenario 3 and 4.

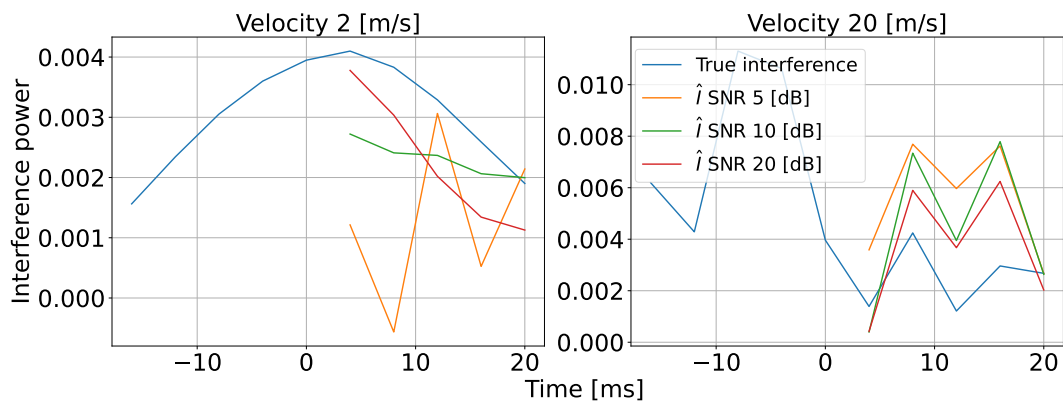


Figure C.3: Time trace plot a prediction for scenario 5 and 6.

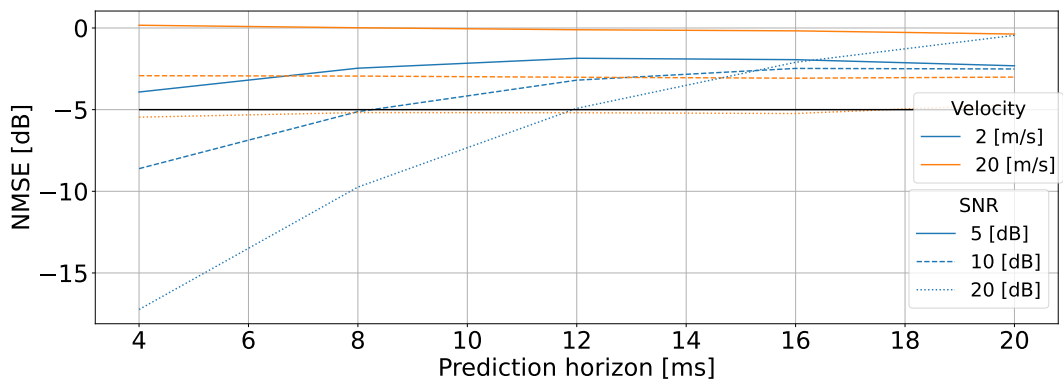


Figure C.4: NMSE versus prediction horizon for the AR(20) predictor with measurement horizon set to 5 [s] for test scenario 5 and 6.

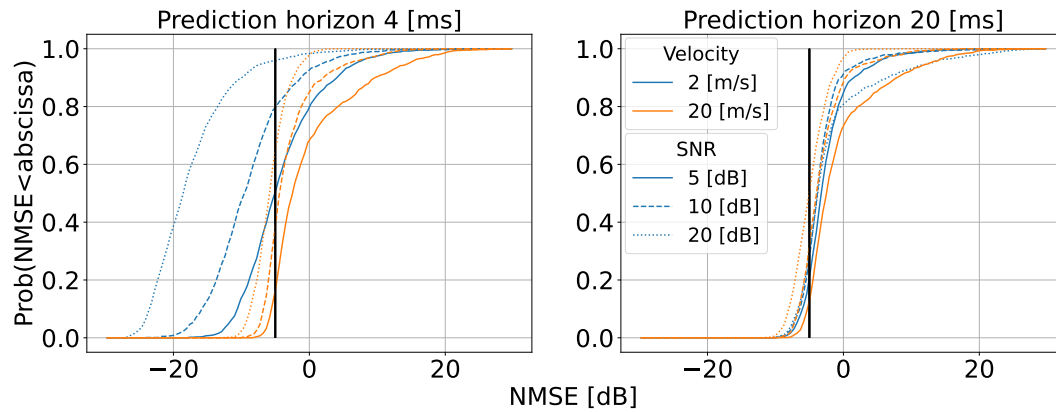


Figure C.5: CDF of NMSE for the AR(20) predictor with prediction horizons on 4 and 20 [ms] and a measurement horizon on 5 [s] for test scenario 5 and 6.

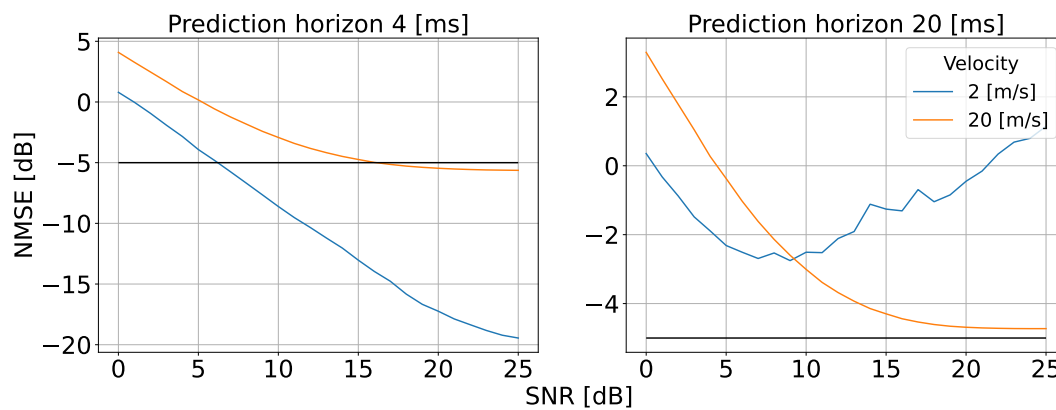


Figure C.6: NMSE versus SNR for the AR(20) predictor with prediction horizons on 4 and 20 [ms] and a measurement horizon on 5 [s] for test scenario 5 and 6.

Bibliography

- [1] J. F. Schmidt, U. Schilcher, M. K. Atiq, and C. Bettstetter, “Interference prediction in wireless networks: Stochastic geometry meets recursive filtering,” *IEEE Transactions on Vehicular Technology*, vol. 70, no. 3, pp. 2783–2793, 2021. DOI: 10.1109/TVT.2021.3059032.
- [2] N. Baccour, D. Puccinelli, T. Voigt, *et al.*, “External radio interference,” in *Radio Link Quality Estimation in Low-Power Wireless Networks*. Heidelberg: Springer International Publishing, 2013, pp. 21–63, ISBN: 978-3-319-00774-8. DOI: 10.1007/978-3-319-00774-8_2. [Online]. Available: https://doi.org/10.1007/978-3-319-00774-8_2.
- [3] S. Nayak and R. Patgiri, “6g communication: Envisioning the key issues and challenges,” *EAI Endorsed Transactions on Internet of Things*, vol. 6, no. 24, p. 166959, 2021. DOI: 10.4108/eai.11-11-2020.166959. [Online]. Available: <https://doi.org/10.4108/eai.11-11-2020.166959>.
- [4] G. Berardinelli, P. Baracca, R. O. Adeogun, *et al.*, “Extreme communication in 6g: Vision and challenges for ‘in-x’ subnetworks,” *IEEE Open Journal of the Communications Society*, vol. 2, pp. 2516–2535, 2021. DOI: 10.1109/OJCOMS.2021.3121530.
- [5] R. Adeogun, G. Berardinelli, and P. E. Mogensen, “Enhanced interference management for 6g in-x subnetworks,” English, *IEEE Access*, Apr. 2022, ISSN: 2169-3536. DOI: 10.1109/ACCESS.2022.3170694.
- [6] R. Adeogun and G. Berardinelli, “Intelligent multi-agent resource allocation in 6g in-x subnetworks with limited sensing information,” English, *IEEE Communications Letters*, 2022, ISSN: 1089-7798.
- [7] R. Adeogun, G. Berardinelli, I. Rodriguez, and P. Mogensen, “Distributed dynamic channel allocation in 6g in-x subnetworks for industrial automation,” in *2020 IEEE Globecom Workshops (GC Wkshps)*, 2020, pp. 1–6. DOI: 10.1109/GCWkshps50303.2020.9367532.
- [8] R. Adeogun, G. Berardinelli, P. E. Mogensen, I. Rodriguez, and M. Razzaghpour, “Towards 6g in-x subnetworks with sub-millisecond communication cycles and extreme reliability,” *IEEE Access*, vol. 8, pp. 110172–110188, 2020. DOI: 10.1109/ACCESS.2020.3001625.

- [9] X. Xing, T. Jing, W. Cheng, Y. Huo, and X. Cheng, "Spectrum prediction in cognitive radio networks," *IEEE Wireless Communications*, vol. 20, no. 2, pp. 90–96, 2013. DOI: 10.1109/MWC.2013.6507399.
- [10] M. Giordani, M. Polese, M. Mezzavilla, S. Rangan, and M. Zorzi, "Toward 6g networks: Use cases and technologies," *IEEE Communications Magazine*, vol. 58, no. 3, pp. 55–61, 2020. DOI: 10.1109/MCOM.001.1900411.
- [11] B. Błaszczyszyn, M. Haenggi, P. Keeler, and S. Mukherjee, *Stochastic Geometry Analysis of Cellular Networks*. Cambridge University Press, 2018. DOI: 10.1017/9781316677339.
- [12] T. M. Cover and J. A. Thomas, *Elements of Information Theory*, 2nd ed. John Wiley & Sons, Inc, 2006, ISBN: 978-0-471-24195-9.
- [13] R. K. Saha, "On application and evaluation of millimeter-wave spectrum sharing, trading and reusing for small cells toward spectral and energy efficiencies of 6g," in *2020 23rd International Symposium on Wireless Personal Multimedia Communications (WPMC)*, 2020, pp. 1–6. DOI: 10.1109/WPMC50192.2020.9309473.
- [14] R. K. Saha, "Approaches to improve millimeter-wave spectrum utilization using indoor small cells in multi-operator environments toward 6g," *IEEE Access*, vol. 8, pp. 207 643–207 658, 2020. DOI: 10.1109/ACCESS.2020.3037684.
- [15] H. Shokri-Ghadikolaei, C. Fischione, and E. Modiano, "On the accuracy of interference models in wireless communications," pp. 1–6, 2016. DOI: 10.1109/ICC.2016.7510904.
- [16] H. ElSawy, A. Sultan-Salem, M.-S. Alouini, and M. Z. Win, "Modeling and analysis of cellular networks using stochastic geometry: A tutorial," *IEEE Communication Surveys and Tutorials*, 2016. [Online]. Available: <http://hdl.handle.net/10754/605178.1>.
- [17] U. Schilcher, J. F. Schmidt, M. K. Atiq, and C. Bettstetter, "Autocorrelation and coherence time of interference in poisson networks," *IEEE Transactions on Mobile Computing*, vol. 19, no. 7, pp. 1506–1518, 2020. DOI: 10.1109/TMC.2019.2912373.
- [18] U. Schilcher, S. Toumpis, M. Haenggi, A. Crismani, G. Brandner, and C. Bettstetter, "Interference functionals in Poisson networks," *IEEE Trans. Information Theory*, vol. 62, no. 1, pp. 370–383, Jan. 2016. DOI: 10.1109/TIT.2015.2501799.
- [19] M. K. Atiq, U. Schilcher, M. Haenggi, and C. Bettstetter, "Burstiness of interference pikes in wireless networks," 2020, Manuscript under review.
- [20] M. K. Atiq, U. Schilcher, J. F. Schmidt, and C. Bettstetter, "Semi-blind interference prediction in wireless networks," in *Proc. ACM Intern. Conf. on Modeling, Analysis and Simulation of Wireless and Mobile Systems (MSWiM)*, Miami Beach, FL, USA, Nov. 2017, pp. 19–23. DOI: 10.1145/3127540.3127579.

- [21] U. Schilcher, J. F. Schmidt, and C. Bettstetter, "On interference dynamics in Matérn networks," *IEEE Trans. Mobile Computing*, vol. 19, no. 7, pp. 1677–1688, Jul. 2020. DOI: 10.1109/TMC.2019.2911498.
- [22] A. K. Ajami and H. Artail, "Analyzing the throughput of online home users during the covid-19 pandemic using the neyman-scott cluster process," in *2021 17th International Conference on Wireless and Mobile Computing, Networking and Communications (WiMob)*, 2021, pp. 54–59. DOI: 10.1109/WiMob52687.2021.9606408.
- [23] L.-B. Fredriksson, "Controller area networks and the protocol can for machine control systems," *Mechatronics*, vol. 4, pp. 159–172, 1994.
- [24] E. Marin, D. Singelée, B. Yang, I. Verbrauwede, and B. Preneel, "On the feasibility of cryptography for a wireless insulin pump system," *CODASPY '16*, 113–120, 2016. DOI: 10.1145/2857705.2857746. [Online]. Available: <https://doi.org/10.1145/2857705.2857746>.
- [25] M. Toussaint, D. Andreu, P. Fraisse, and D. Guiraudy, "Wireless distributed architecture for therapeutic functional electrical stimulation: A technology to design network-based muscle control," *Conference proceedings : Annual International Conference of the IEEE Engineering in Medicine and Biology Society. IEEE Engineering in Medicine and Biology Society. Conference*, vol. 2010, pp. 6218–21, Aug. 2010. DOI: 10.1109/IEMBS.2010.5627724.
- [26] R. Adeogun, G. Berardinelli, and P. E. Mogensen, "Learning to dynamically allocate radio resources in mobile 6g in-x subnetworks," English, in *2021 IEEE 32nd Annual International Symposium on Personal, Indoor and Mobile Radio Communications (PIMRC)*, ser. I E E E International Symposium Personal, Indoor and Mobile Radio Communications, United States: IEEE, Sep. 2021, pp. 959–965, ISBN: 978-1-7281-7587-4. DOI: 10.1109/PIMRC50174.2021.9569345.
- [27] X. Xing, T. Jing, Y. Huo, H. Li, and X. Cheng, "Channel quality prediction based on bayesian inference in cognitive radio networks," in *2013 Proceedings IEEE INFOCOM*, 2013, pp. 1465–1473. DOI: 10.1109/INFCOM.2013.6566941.
- [28] P. W. Dent, G. E. Bottomley, and T. M. Croft, "Jakes fading model revisited," *Electronics Letters*, vol. 29, pp. 1162–1163, 1993.
- [29] S. Lu, J. May, and R. Haines, "Efficient modeling of correlated shadow fading in dense wireless multi-hop networks," Apr. 2014. DOI: 10.1109/WCNC.2014.6951986.
- [30] S. Lu, J. May, and R. J. Haines, "Effects of correlated shadowing modeling on performance evaluation of wireless sensor networks," pp. 1–5, 2015. DOI: 10.1109/VTCFa11.2015.7390909.

- [31] V. Schmidt, *Stochastic Geometry, Spatial Statistics and Random Fields: Models and Algorithms*, ser. Lecture Notes in Mathematics. Springer International Publishing, 2014, ISBN: 9783319100647. [Online]. Available: <https://books.google.dk/books?id=brsUBQAAQBAJ>.
- [32] “Entropy, relative entropy, and mutual information,” in *Elements of Information Theory*. John Wiley & Sons, Ltd, 2005, ch. 2, pp. 13–55, ISBN: 9780471748823. DOI: <https://doi.org/10.1002/047174882X.ch2>. eprint: <https://onlinelibrary.wiley.com/doi/pdf/10.1002/047174882X.ch2>. [Online]. Available: <https://onlinelibrary.wiley.com/doi/abs/10.1002/047174882X.ch2>.
- [33] P. Olofsson and M. Andersson, *Probability, Statistics and Stochastic Processes*, 2nd. ed. John Wiley & Sons, Ltd, 2012, ISBN: 978-0-470-88974-9.
- [34] R. Shumway and D. Stoffer, *Time Series Analysis and Its Applications*, English, 4th, ser. Springer Texts in Statistics. Springer Cham, 2017, ISBN: 978-3-319-52452-8.
- [35] G. Leobacher and F. Pillichshammer, *Introduction to Quasi-Monte Carlo Integration and Applications*. 2014.
- [36] E. Veach, “Robust monte carlo methods for light transport simulation,” AAI9837162, Ph.D. dissertation, 1998, ISBN: 0591907801.
- [37] R. O. Adeogun, “Channel prediction for mobile mimo wireless communication systems,” Doctoral (Ph.D.) Theses (Supervisors: Ass. Prof. Pawel Dmochowski and Ass. Prof. Paul D. Teal), Ph.D. dissertation, Victoria University of Wellington, New Zealand, 2014.
- [38] M. N. M. van Lieshout, *Markov Point Processes and Their Applications*. Imperial College Press, 2000. DOI: <https://doi.org/10.1142/p060>.
- [39] R. Waagepetersen and J. Møller, *Statistical inference and simulation for spatial point processes*, English, ser. Monographs on Statistics and Applied Probability 100. Chapman & Hall, 2003, ISBN: 1584882654.